Strömungstechnik

Dominik Denker

Gradient Trajectory Analysis of Reacting Turbulent Flows



Gradient Trajectory Analysis of Reacting Turbulent Flows

Gradiententrajektorienanalyse von reagierenden turbulenten Strömungen

Von der Fakultät für Maschinenwesen der Rheinisch-Westfälischen Technischen Hochschule Aachen zur Erlangung des akademischen Grades eines Doktors der Ingenieurwissenschaften genehmigte Dissertation

vorgelegt von

Dominik Denker

Berichter: Univ.-Prof. Dr.-Ing. Heinz Günter Pitsch

Asst. Prof. Antonio Attili, Ph.D.

Tag der mündlichen Prüfung: 23. Oktober 2020

Diese Dissertation ist auf den Internetseiten der Universitätsbibliothek online verfügbar.

Berichte aus der Strömungstechnik

Dominik Denker

Gradient Trajectory Analysis of Reacting Turbulent Flows

Shaker Verlag Düren 2020

Bibliografische Information der Deutschen Nationalbibliothek

Die Deutsche Nationalbibliothek verzeichnet diese Publikation in der Deutschen Nationalbibliografie; detaillierte bibliografische Daten sind im Internet über http://dnb.d-nb.de abrufbar.

Zugl.: D 82 (Diss. RWTH Aachen University, 2020)

Copyright Shaker Verlag 2020 Alle Rechte, auch das des auszugsweisen Nachdruckes, der auszugsweisen oder vollständigen Wiedergabe, der Speicherung in Datenverarbeitungsanlagen und der Übersetzung, vorbehalten.

Printed in Germany.

ISBN 978-3-8440-7739-1 ISSN 0945-2230

Shaker Verlag GmbH • Am Langen Graben 15a • 52353 Düren Telefon: 02421/99 0 11 - 0 • Telefax: 02421/99 0 11 - 9

Internet: www.shaker.de • E-Mail: info@shaker.de

Acknowlegments

The present thesis was completed during my time as a research assistant at the Institute for Combustion Technology, RWTH Aachen University. The research was funded in part from the Deutsche Forschungsgemeinschaft (DFG) under the Project "Regimes in Turbulent Non-Premixed Combustion" as well as from the European Research Counsel (ERC) Advanced Grant "Milestone" (Multi-Scale Description of Non-Universal Behavior in Turbulent Combustion.) The majority of the simulations and the analysis of the results were by conducted on the supercomputers JUQEEN, JURECA and JUWELS of the Forschungszentrum Jülich. I appreciate the sizeable calculation resources provided by the Jülich Aachen Research Alliance (JARA) and the Gauss Centre for Supercomputing (GSC).

I would like to thank my advisor Prof. Heinz Pitsch for his support and guidance as well as for the trust placed in my scientific work which allowed and encouraged me to pursue and develop my own instincts and research interests. The underlying vision and ideas for this work originate from discussions with Prof. Norbert Peters at the very start of my career. Although my time under his guidance was unfortunately cut short, his genius, a seemingly endless enthusiasm and scientific curiosity in combination with his friendly and unassuming nature left a lasting impression on me. I am immensely grateful for the limited time I had the privilege to work with him. Further, I would like to thank my second supervisor Prof. Antonio Attili for the valuable advice and encouragement throughout my research. This thesis benefited greatly from his altruistic commitment and continued dedication in innumerable, highly enjoyable scientific discussions. I am also grateful to Prof. Manfred Wirsum for being the chair of the committee.

I would like to extend my gratitude to my colleagues at the Institute for Combustion Technology for their help, advice and friendship. The unique and amiable environment with a plethora of scientific and also non-scientific discussion topics was largely owed to my dear office mates Jonas Boschung and Fabian Hennig. Further, I would like to especially thank Abhishek Khetan, Stephan Kruse, Kai Niemietz, Metin Korkmaz, Raymond Langer, Bernhard Jochim, Konstantin Kleinheinz and Lukas Berger for the countless memorable moments during discussions, extracurricular activities and conferences.

I am also appreciative for the support I received from the previous gen-

erations of the turbulence group, foremost for the invaluable advice from Michael Gauding and Jens-Henrik Göbbert. Moreover, I would like to thank the student assistants and undergraduate students that worked with me.

Finally, I wish to thank my family on both sides of the Atlantic for their encouragement and interest. Most of all I am beholden to my wife, Amy, for her unlimited love, support and patience.

Zusammenfassung

In dieser Arbeit werden reagierende turbulente Strömungen mit der Dissipations Element (DE) Analyse untersucht. Dies ist eine Gradiententrajektorien basierte Methode zur Unterteilung turbulenter Felder in raumfüllende Unterregionen, in denen sich Skalare monoton verhalten. Im Kontext der Verbrennung ist diese Eigenschaft wichtig, da DEs somit lokal und eindeutig das maximale Ausmaß aufzeigen, welches eine von diffusivem Transport dominierte Struktur, wie z.B. eine Flamme, in einer turbulenten Strömung potentiell einnehmen kann.

Zuerst wird die DE-Analyse auf das Mischungsbruchfeld Z aus direkten numerischen Simulationen (DNS) von nicht vorgemischten Freistrahlflammen angewandt. Es wird gezeigt, dass sich die normierte DE-Parameterstatistik sowie die charakteristischen Skalierungen der jeweiligen Mittelwertgrößen nicht von innerten turbulenten Strömungen unterscheiden. Zusätzlich wird gezeigt, dass die skalare Dissipationsrate χ mit dem Gradienten der größeren lokalen Strömungstopologie, dem DE-Gradienten g, in Beziehung gesetzt werden kann. Ein DE-Parameter basiertes Regimediagramm für nicht vorgemischte Verbrennung wird eingeführt und verifiziert.

Des weiteren werden nicht-lokale Effekte in DNS von vorgemischten Freistrahlflammen untersucht. Die DE Analyse wird auf die Temperaturfelder T angewendet, welche jedoch im Gegensatz zu Z einen chemischen Quellterm besitzen. Die Selbstähnlichkeit der normierten DE-Längenverteilung bleibt bestehen, jedoch zeigt die Statistik der skalaren Differenz ΔT einen deutlichen Einfluss der Flammenstruktur. In der Flammenstrukturanalyse wird gezeigt, dass die Einführung von Extrempunkten nahe der Flammenfront zu einer signifikanten Verdickung der Vorwärm- und Reaktionszone führt. Dieser Effekt wird quantifiziert und mit der Brenngeschwindigkeit in Beziehung gesetzt.

Abschließend werden die gewonnenen Erkenntnisse bei der Modellierung der Verbrennung genutzt. Die Skalierung und Selbstähnlichkeit der DE-Parameterstatistik werden in einer Methodik für die Vorhersage von Verbrennungsregimen bei nicht vorgemischter Verbrennung verwendet. Diese Methodik wird in Reynolds-gemittelten Navier-Stokes-Simulationen eines PKW-Dieselmotors angewendet. Weiterhin wird ein Modell für die Wahrscheinlichkeitsdichtefunktion von Z eingeführt, welches Effekte von laminaren Bereichen und externer Intermittenz berücksichtigt.

Abstract

In this thesis, reacting turbulent flows are analyzed from a structural point of view using Dissipation Element (DE) analysis, which is a gradient trajectory (GT) based method for compartmentalizing turbulent fields into space filling sub-regions in which scalars behave monotonically. In the context of combustion, this property is important, as DEs locally and unambiguously indicate the maximum extent a diffusive transport dominated structure, such as a flame, can potentially occupy in a turbulent flow.

First, DE analysis is applied to the mixture fraction field Z of a series of direct numerical simulations (DNS) of non-premixed jet flames. In a statistical investigation, it is shown that the normalized DE parameter statistics as well as the characteristic scalings of the respective mean quantities do not differ from non-reacting turbulent flows and are therefore unaffected by the heat release. Additionally, it is demonstrated that the scalar dissipation rate χ can be related to the gradient of the larger local flow topology as represented by the DE gradient g. The DE parameters are then used in the construction of a regime diagram for non-premixed combustion which is verified by the DNS results.

Secondly, non-local effects in DNS of premixed combustion are investigated in a series of spatially evolving jet flames. DE analysis is applied to the temperature fields T which, contrary to Z, possess a chemical source term. The self-similarity of the normalized DE length distribution is retained, but the statistics of the scalar difference ΔT show a clear influence of the flame structure. In the consecutive GT based flame structure analysis, it is shown that the introduction of extremal points close to the flame front leads to a significant thickening of both the preheating and inner reaction zone. This effect is quantified and related to the turbulent burning velocity.

Finally, the insights gained are used in combustion modelling. The scaling and self-similarity of the DE parameter statistics are used in a framework for the prediction of combustion regimes in non-premixed combustion. This framework is applied in the Reynolds averaged Navier-Stokes simulation of a passenger car diesel engine. Further, a novel model for the probability density function of Z is presented, which considers effects of laminar regions and external intermittency.

Publications

This thesis is mainly based on the following publications in scientific journals and a book chapter.

- D. Denker et al. "Dissipation element analysis of premixed jet flames". In: Comb. Sci. Tech. 191.9 (2019), pp. 1677–1683.
- D. Denker, A. Attili, and H. Pitsch. "Dissipation Element Analysis of Inert and Reacting Turbulent Flows". In: *Data Analysis for Direct Numerical Simulations of Turbulent Combustion*. Ed. by H. Pitsch and A. Attili. Springer International Publishing, 2020. Chap. 2, pp. 19–41.
- D. Denker et al. "A New Modeling Approach for Mixture Fraction Statistics Based on Dissipation Elements". In: *Proc. Comb. Inst* (2020).
- D. Denker et al. "Gradient Trajectory Analysis of the Burning Rate in Turbulent Premixed Jet Flames". In: *Comb. Sc. and Tech.* 192.11 (2020), pp. 2189–2207.
- D. Denker et al. "Dissipation Element Analysis of Non-premixed Jet Flames". In: *J. Fluid Mech.* 905 (2020), A4.

Additionally, the following journal publications were contributed during my time at the Institute for Combustion Technology:

- J. Boschung et al. "Finite Reynolds number corrections to the 4/5-law for decaying turbulence". In: *Phys. Rev. Fluids* 1.064403 (2016).
- J. Boschung et al. "Analysis of structure function equations up to the seventh order". In: *J. Turbul.* (2017), pp. 1–32.
- A. Schnorr et al. "Feature Tracking by Two-Step Optimization". In: *IEEE Transactions on Visualization and Computer Graphics* (2018).
- M. Bode et al. "Using Physics-Informed Super-Resolution Generative Adversarial Networks for Subgrid Modeling in Turbulent Reactive Flows". In: Proc. Comb. Inst. (2020).

- M. Gauding et al. "On the combined effect of internal and external intermittency in turbulent non-premixed jet flames". In: *Proc. Comb. Inst.* (2020).
- A. Attili et al. "Turbulent flame speed and reaction layer thickening in premixed jet flames at constant Karlovitz and increasing Reynolds numbers". In: *Proc. Comb. Institute* (2020).

Contents

A	ckno	wlegments	iii
Zι	ısam	menfassung	\mathbf{v}
\mathbf{A}	ostra	<u>ct</u>	vii
Pι	ıblic	ations	ix
C	onter	nts.	хi
Li	st of	Figures	$\mathbf{x}\mathbf{v}$
Li	st of	Tables	xix
1	Intr	roduction and Motivation	1
2	Intr	roduction to Reacting Turbulent Flows	3
	2.1	Theoretical Concepts of Turbulence	3
		2.1.1 Governing Equations of Fluid Motion	3
		2.1.2 Characteristics of Turbulent Flows	5
		2.1.3 Scales in Turbulent Flows	6
		2.1.4 Geometries in Turbulent Flows	9
	2.2	Introduction to Turbulent Combustion	10
		2.2.1 Non-dimensional Numbers in Turbulent Combustion .	11
		2.2.2 Models for Turbulent Combustion	13
	2.3		15
-			
3		roduction to Dissipation Element Analysis	19
	3.1	Introduction to Dissipation Elements	19
		3.1.1 Definition of Dissipation Elements	19
		3.1.2 Physical and Numerical Considerations	24
	3.2	Statistics of Dissipation Element Parameters	27
		3.2.1 Marginal Statistics and Scaling of mean DE Parameters	27
		3.2.2 Joint Statistics	28

		3.2.3 DE analysis of Reacting Flows	32
4	Dire	ect Numerical Simulations of Turbulent Reacting Flows	37
-	4.1	Introduction to Direct Numerical Simulations	37
	4.2	Numerical Methods and Algorithms	40
	1.2	4.2.1 Numerical Methods of the Non-Reacting Cases	42
	4.3	Configurations and Case Descriptions	43
	4.4	Turbulent Flame Analysis	46
	1.1	Turbulent Finne Hindysis	10
5	Diss	sipation Element Based Flame Analysis of Non-Premixed	
	Flai	mes	51
	5.1	Dissipation Element Analysis	53
		5.1.1 Marginal Dissipation Element Parameter Statistics	55
		5.1.2 Joint Dissipation Element Parameter Statistics	58
	5.2	Regimes in Turbulent Non-Premixed Combustion	63
		5.2.1 Local Flame Analysis	73
		5.2.2 Temporal Evolution of the Combustion Regimes	76
6		sipation Element Analysis of Turbulent Premixed Com-	
	bus	tion	79
		6.0.1 Configurations	79
	6.1	DE Analysis of the Temperature Fields in Premixed Jet Flames	•
		6.1.1 Marginal Statistics	82
		6.1.2 Joint Statistics	88
	6.2	Gradient Trajectory Analysis of the Burning Rate	96
		6.2.1 Flame Structure Analysis	98
		6.2.2 Correlation between Reacting Scalars and DE Parameters	•
		6.2.3 Integral Statistics	108
=			4 4 6
7		dient Trajectory Statistics Based Modelling Applications	•
	7.1	<u> </u>	113
			114
			119
	- 0		121
	7.2	U 11	124
		3 0	128
			129
		<u> </u>	131
		7.2.4 Model Validation and Discussion	134

8 Summary and Conclusion

137

List of Figures

3.1	Schematic representation of a DE and its parameters in one-	
	dimensional space.	20
3.2	Schematic representation of gradient trajectories connecting	
	the same extremal points in three dimensional space	21
3.3	A DE in the mixture fraction field Z in a DNS of non-premixed	
	temporally evolving jet flame	22
3.4	Schematic representation of the potential methods of obtaining	
	spatial statistics in the DE decomposed space	23
3.5	PDF of the normalized DE length $\ell/\ell_{\rm m}$	28
3.6	Ratio of the Kolmogorov micro scale η to the mean DE length	
	$\ell_{\rm m}$ for various inert and reacting cases	29
3.7	JPDFS of the normalized DE length and DE scalar difference	
	for various fields in different flow configurations	30
3.8	Mean DE scalar difference conditioned on the DE length for	
	various flow configurations	32
3.9	a): Mixture fraction Z profile in physical space obtained from a	
	counterflow configuration and schematic DEs. b): Correspond-	
	ing stationary flamelet solution of the normalized heat release	
	$\dot{\omega}_T$ in mixture fraction space. c) and d): Mean stoichiometric	
	temperature $\langle T_{\rm st} \rangle$ in a DNS of planar non-premixed jet flame	
	conditioned on the stoichiometric scalar dissipation rate $\chi_{\rm st}$.	34
4.1	General setup of the non-premixed DNS investigated in this	
	thesis.	42
4.2	Starting profiles of the stream-wise mean velocity component	
	and scalars.	45
4.3	Mixture fraction Z in the x-y center plane at time steps $t^* = 10$	
	and $t^* = 20$	48
4.4	Normalized temperature T^* in the x-y center plane at time	
	steps $t^* = 10$ and $t^* = 20$	49
4.5	Temporal evolution of the normalized Favre averaged scalar	
	dissipation rate and temporal evolution of the normalized area	
	of the iso surface of the stoichiometric mixture fraction	50

F1 ADD: ' ' 'I	11 0 C + 1 1 D 1	_
	the flame front in the low Re low	
dilution case.		54
5.2 DE analysis of the mixture	e fraction field of the intermediate	
		55
5.3 Comparison of PDFs of the	e normalized DE length $\ell/\ell_{ m m}$	57
5.4 JPDF of the normalized D	E length $\ell^* = \ell/\ell_{\rm m}$ and normalized	_
scalar difference $\Delta Z^* = \Delta Z^*$	$Z/\Delta Z_{ m m}$	60
5.5 Normalized DE scalar differ	rence conditioned on the normalized	
DE length $\langle \Delta Z^* \ell^* \rangle$ and $\langle \Delta Z^* \ell^* \rangle$	$\Delta\phi^* \ell^* angle$	61
5.6 Average ratio $C_{\gamma} = \langle \chi / (2R) \rangle$	$O(g^2)$ in the final time step of the	_
respective simulations		62
5.7 DE parameter based regime	diagram for turbulent non-premixed	_
combustion		66
5.8 Comparison of the mixture	fraction conditioned PDFs $P(T Z)$	_
	e PDF of the temperature averaged	_
		67
	steady state flamelet solutions at	•
	n rates and the inner reaction zone	=
approximation by means of		68
	ditioned on normalized DE parame-	J O
		70
	0/04	10
	$_{ m OH} angle$ conditioned on normalized DE	1
		71
	minima $\langle T_{\rm DE,min} \rangle$ and in the max-	
	ssing the stoichiometric iso-surface	
	ized DE parameter g' and $\Delta Z'$ for	
the high Re case		72
	conditioned on the stoichiometric	
		72
5.14 Mass fraction of OH radic	als obtained along all gradient tra-	
jectories of a single DE		73
5.15 Mean DE coefficient of v	ariation of the OH mass fraction	
$\langle c_{\rm v,OH}(Z_{\rm st}) \rangle$ conditioned or	n the normalized DE parameters g'	
and $\Delta Z'$		75
5.16 Temporal evolution of the n	ormalized area of the stoichiometric	_
iso surface attributed to the		77
6.1 Atomic oxygen mass fracti	on in the $x-y$ center plane of the	_
		80

6.2	Upstream $x - y$ center plane of the temperature fields and	
_	mirrored corresponding DE analysis of the temperature field.	83
6.3	DE analysis of the passive scalar field in the Inert Isotropic case	. 84
6.4	Normalized mean DE length $\ell_{\rm m}/\eta$ and normalized mean DE	
	differences $\Delta \phi_{\rm m}/\Delta \phi_{\rm max}$ and $\Delta T_{\rm m}/\Delta T_{\rm max}$	84
6.5	PDFs of normalized separation length $\ell^* = \ell/\ell_m$	87
6.6	JPDFs of the normalized separation length and normalized	
	scalar difference $P(\Delta \phi^*, \ell^*)$	89
6.7	JPDFs of the normalized separation length $\ell/\delta_{\rm F}$ and the nor-	
	malized scalar difference $\Delta T/(T_{\rm b}-T_{\rm u})$	91
6.8	Kullback-Leibler divergence of the JPDFs of the normalized	
	DE parameters of the various cases with reference to the JPDF	
	obtained from the Inert Isotropic case	93
6.9	Normalized mean DE scalar difference conditioned on the nor-	
	malized DE length	95
6.10	The $T = 1800$ K iso-surface in the stream-wise regions investi-	
	gated.	98
6.11	Mean temperature conditioned on the arc-length distance to	
	the flame surface and the mean temperature additionally con-	
	ditioned on the normalized scalar difference	99
6.12	JPDF of the normalized temperature gradient $\nabla T/\nabla T_{\rm fl}(1800{\rm K})$	
	and the normalized arc-length distance $s/\delta_{\rm F}$ in the High Re	
	case conditioned on the normalized scalar difference ΔT^*	101
6.13	Schematic illustration of the impact of the scalar structure as	
	indicated by DEs	102
6.14	PDF of the normalized DE parameters ΔT^* and $\ell^* = \ell/\ell_{\rm fl}(\Delta T)$	
	weighted with the intersection area of the individual DE and	
	the flame surface.	104
6.15	Selected mean normalized mass fractions $\langle Y_{\alpha}^* \rangle = \langle Y_{\alpha} \rangle / \max Y_{\alpha, \text{fl}}$	
	and normalized CH ₄ source term $\langle \dot{\omega}_{\text{CH}_4}^* \rangle = \langle \dot{\omega}_{\text{CH}_4} \rangle / \min \dot{\omega}_{\text{CH}_4,\text{fl}}$	
	conditioned on the normalized DE parameters and the temper-	
	ature of their respective maximum value in the laminar flamelet	
	solution in the High Re case	106
6.16	Mean mass fractions $\langle Y_{\alpha} \rangle$ in the High Re case conditioned on	
	arc-length distance s to the flame surface and conditioned on	
	the normalized scalar difference ΔT^* and the normalized DE	
	length ℓ^*	107

6.17	Mean CH ₄ source term $\langle \dot{\omega}_{\text{CH}_4} \rangle$ in the High Re case condi-	
	tioned on arc-length distance s to the flame surface and scalar	
	difference ΔT^*	108
6.18	a): $\langle I_s \rangle$ conditioned on the normalized DE parameters $\ell/\delta_{\rm F}$	
	and $\Delta T/(T_{\rm b}-T_{\rm b})$ in the High Re case. b): Instantaneous	
	CH_4 source term $\dot{\omega}_{\mathrm{CH}_4}(T)$ for two exemplary DEs and the	
	laminar flamelet solution. c): $\langle I_T \rangle$ conditioned on ℓ/δ_F and	
	$\Delta T/(T_{\rm b}-T_{\rm b})$ in the High Re case	110
7.1	PDF of the normalized DE length $\ell^* = \ell/\ell_m$ directly obtained	
	DNS and obtained from the stochastic transport equation	117
7.2	The mean normalized scalar difference conditioned on the	
	normalized DE length ℓ from the high Re case and conditional	
	mean obtained from the stochastic transport equation	118
7.3	JPDF of modelled normalized DE parameters at the iso-surface	
	of $\widetilde{Z}_{\mathrm{st}}$ for three crank angle positions for the baseline case	122
7.4	Mean stoichiometric iso-surface for three different crank angle	
	positions in CFD simulation of the baseline case	123
7.5	Temporal evolution of the stoichiometric iso-surface attributed	
	to the individual regimes.	124
7.6	Integrated probability of the "Burning Flamelet" regime $\mathcal{P}_{\text{Flamelet}}$	
	in all simulated operation points	125
7.7	JPDF of the DE parameters conditioned on turbulent core	
	region (left) and TNTI region (right) in the Inert Jet case	130
7.8	short caption	131
7.9	Modelling results of the zonal PDFs $P_i(Z)$ employing the joint	
	DE statistics obtained from DNS	132
7.10	PDF of the normalized scalar difference $P(\Delta Z^*)$ and normal-	
	ized PDF of the scalar difference conditioned on arithmetic	
	mean $P(\Delta Z^* Z_{\rm m})$ in the Mixing Layer	133
7.11	PDF of the mixture fraction $P(Z)$ for five cross-stream positions	
	$y/h_{1/2}$, with the jet half width $h_{1/2}$, for the Jet Flame and	
	Inert Jet.	135
7.12	Mean density $\overline{\rho}$ obtained from the convolution of $P(Z)$ with a	100
	steady state flamelet solution for the Jet Flame	136

List of Tables

4.1	Numerical and physical initial parameters of the DNS. Where	
	needed, the parameters for the Non-Reacting case II were	
	re-computed with the given values for \overline{U}_0 and H_0	46
6.1	Simulation parameters of the reacting configurations investi-	
	gated in this chapter. The turbulence statistics are evaluated	
	at the stream-wise position of $x/l_{\rm F} = 0.6$	81
7.1	Simulated operating points in the CFD of the DI diesel engine.	120
7.2	Numerical and physical initial parameters of the DNS	128

1 Introduction and Motivation

With a growing world population and projected strong economic growth in currently underdeveloped countries, world wide energy consumption is estimated to increase by 1.4% each year for the next three decades according to the World Energy Outlook 129. Regardless of the substantial national and international efforts to reform the energy sector, this exponentially growing demand for energy will be largely met with fossil fuels. The U.S. Energy Information Administration predicts that in the year 2050, more than 70% of the primary energy consumption will still stem from fossil fuel sources 67. Combustion as the presently predominant mode of the energy conversion of fossil fuels will remain an omnipresent key technology due to its cost effectiveness and flexibility. Further, the emergence of liquid fuels processed from biomass or e-fuels as an indirect result of the increasing usage of intermittent renewable energy sources will propagate the importance of combustion technology.

It is therefore of paramount importance to further develop energy systems based on combustion technology to increase the efficiency in order to lower greenhouse gas emissions as well as to preserve the finite fossil fuel resources. Additionally, the environmental aspect of harmful pollutants such as NO_x , soot and unburned hydrocarbons associated with the operation of current combustion devices requires urgent attention.

Due to ever increasing computing resources, computational fluid dynamics (CFD) tools have become indispensable in the engineering process of combustion systems. Among the benefits of utilizing CFD are the significant reduction of the designing and development process cost as well as significant performance gains of the combustion applications enabled by the more comprehensive and complementary insights gained with this approach.

In the engineering or industrial context, combustion takes place in turbulent flow fields to greatly increase the output and efficiency. Simulating the resulting highly non-linear, multi-physics and multi-scale problem is a considerable challenge. Traditionally, this is achieved by using the Reynolds averaged Navier-Stokes (RANS) approach, or more recently, large eddy simulations (LES). In addition to the original closure problem faced in any turbulent flow and the consequent need to use turbulence models, both RANS and LES require combustion models. Therefore, the quality and the predictive

nature of CFD results is inseparably linked to the reliability of the utilized combustion model. Good simulation results have been achieved for a large variety of devices including internal combustion engines, aircraft engines, and stationary gas turbines.

State-of-the-art combustion models exploit the assumption that the chemical processes are significantly faster than the turbulent mixing processes. This assumption is well justified for a large variety of combustion devices and operation points, as evident from the widespread use and success of CFD. However, to achieve the goal of simultaneously lowering emissions while increasing the efficiency, novel avenues for combustion processes must be explored. A promising and much pursued approach is low temperature combustion (LTC). A variety of different technologies fall under this category, such as partially premixed charge compression ignition (PCCI), homogeneous charge compression ignition (HCCI) in internal combustion engines, moderate or intense low oxygen dilution (MILD) in power generation and lean direct injection in aircraft engines. These technologies all have in common that oxidizer or fuel stream are diluted to various degrees. The resulting decrease in temperature causes the chemical processes to slow down. Therefore, the assumed separation of the combustion and turbulent scales loses its validity and the resulting complex combustion phenomena must be considered in combustion models for truly predictive CFD results.

In the present thesis, these combustion conditions are investigated numerically for non-premixed and premixed combustion. To eliminate uncertainties introduced by model assumptions, these investigations are carried out using direct numerical simulations (DNS). Due to the immense computational cost of DNS, these simulations can only be carried out for highly idealized configurations on a non-dimensional basis. The sheer volume of data obtained and the high level of complexity of turbulent flows then poses significant challenges for the subsequent investigation. To overcome this challenge, a gradient trajectory based method called Dissipation Element (DE) analysis is used to compartmentalize the entire reacting turbulent flow field into small, physically meaningful sub-units. These individual sub-units are then susceptible to a more intuitive consideration. Following this approach, combustion model assumptions are tested systematically and compared to the flame structure within DEs. The observed deviations are related to DE parameters which describe the local topology of the scalar field. By combining the insight gained from the gradient trajectory based analysis of the combustion and the statistics of DE parameters, a novel methodology for combustion regime classification and combustion modelling is introduced.

2 Introduction to Reacting Turbulent Flows

The presented thesis investigates the interaction between two very complex, yet vastly different physical phenomena: turbulence and combustion chemistry. In the following chapter, a very brief introduction to both will be given to emphasize and illustrate the challenge of investigating their highly non-trivial interaction in reacting turbulent flows.

2.1 Theoretical Concepts of Turbulence

Most flows both in engineering applications and nature are turbulent. Examples range from the mixing of milk and coffee, to atmospheric flow fields all the way to the turbulent movement of young star clusters [49]. A multitude of technical processes which are taken for granted would be practically impossible without the specific characteristics of turbulence. Neither efficient internal combustion engines nor power plants would be feasible. Even though the governing equations have been known for more than a hundred years and despite the dedicated work of generations of researchers, turbulence is far from understood and a surprisingly low number of exact results exist.

In this section, the governing equations are presented followed by a brief discussion of the general properties of turbulence and traditional methods of investigating turbulent flows.

2.1.1 Governing Equations of Fluid Motion

In the continuum limit, the limit in which the mean free path of the molecules of the investigated fluid is significantly smaller than the smallest scales in the velocity field, the momentum equations governing the evolution of the velocity field u_i at all points in time and space can be written in differential form as

$$\frac{\partial \rho u_i}{\partial t} + \frac{\partial \rho u_i u_j}{\partial x_i} = \frac{\partial \tau_{ij}}{\partial x_i} + \rho f_i, \qquad (2.1)$$

¹In eq. (2.1) and throughout the remainder of this thesis, Einstein's summation convention is used. This signifies that any index appearing twice in a given equation implies a summation over said index.

with ρ being the flow density, τ_{ij} denoting the stress tensor which accounts for all forces acting in the surfaces of an infinitesimal fluid volume, and f_i being the volume forces. f_i will be neglected in the following introduction and investigation due to its subordinate influence on the subject matter. The momentum equations are complemented with the equation for mass conservation

$$\frac{\partial \rho}{\partial t} + \frac{\partial \rho u_j}{\partial x_j} = 0. {(2.2)}$$

The stress tensor τ_{ij} in eq. (2.1) can be subdivided into an isotropic and an anisotropic contribution

$$\tau_{ij} = -p\delta_{ij} + \tau_{ij,a} \,, \tag{2.3}$$

where p denotes the pressure and δ_{ij} represents the Kronecker delta. For Newtonian fluids, the anisotropic part of the stress tensor $\tau_{ij,a}$ is assumed to be proportional to the viscosity of the fluid and the local gradients of the velocity fields and modeled as

$$\tau_{ij,a} = \rho \nu \left(\frac{\partial u_j}{\partial x_i} + \frac{\partial u_j}{\partial x_j} - \frac{2}{3} \delta_{ij} \frac{\partial u_k}{\partial x_k} \right), \qquad (2.4)$$

with ν denoting the kinematic viscosity. This approximation is valid if the time scale on which fluid molecules react to changes of the velocity gradients is far smaller than the time scales on which the velocity gradients themselves are changed. This is given for the flow configurations investigated in this thesis. Substituting the modeled Ansatz eq. (2.4) for the anisotropic contribution of the stress tensor in eq. (2.1), one arrives at the Navier-Stokes equations. In a traditional introduction to the topic of turbulence, further simplifications would be performed assuming constant material properties of the investigated fluid. In the case of a homogenous distribution of the density $\rho = \text{const}$, both the mass conservation equation and the Navier-Stokes equations are simplified further. However, the reacting flows investigated in this thesis are characterized by both large spatial density and viscosity gradients. Consequently, the governing equations are more cumbersome.

It can be shown that the Navier-Stokes equations obey several transformational invariances such as the invariance regarding rotations and reflections of the coordinate systems. Further, the Navier-Stokes equations are Galilean invariant which signifies that the equations remain unchanged when written in a coordinate system which is moving with a fixed velocity.

A quantity of interest directly derived from the Navier-Stokes equations which will be utilized in the investigation in this thesis is the vorticity ω_i .

The vorticity describes the local spinning motion of the flow field which is inseparably linked to the presence of turbulence. Taking the curl of the Navier-Stokes equations yields the equation for the vorticity $\omega_i = \epsilon_{ijk} \partial u_k / \partial x_k$, where ϵ_{ijk} indicates the Levi-Civita symbol,

$$\begin{split} \frac{\partial \omega_{i}}{\partial t} + u_{i} \frac{\partial \omega_{j}}{\partial x_{i}} &= \\ \epsilon_{ijk} \frac{\partial}{\partial x_{i}} \left(\frac{1}{\rho} \frac{\partial \tau_{km,a}}{\partial x_{m}} \right) + \omega_{i} \frac{\partial u_{j}}{\partial x_{i}} - \omega_{j} \frac{\partial u_{j}}{\partial x_{j}} + \epsilon_{ijk} \frac{1}{\rho^{2}} \frac{\partial \rho}{\partial x_{i}} \frac{\partial p}{\partial x_{k}} \,. \end{split} \tag{2.5}$$

The vortex stretching term $\omega_i \frac{\partial u_j}{\partial x_i}$ constitutes a source term which is only present in three-dimensional flows. Consequently, two-dimensional and three-dimensional turbulent flows are fundamentally different. An additional source term for the vorticity, only present in non-constant density flows, is the baroclinic term $\epsilon_{ijk} \frac{1}{\rho^2} \frac{\partial \rho}{\partial x_i} \frac{\partial p}{\partial x_k}$ which stems from the misalignment of the density and pressure gradients.

2.1.2 Characteristics of Turbulent Flows

The Navier-Stokes equations can be normalized using a suitable reference length L and reference velocity U. The only non-dimensional number that emerges is the Reynolds number

$$Re = \frac{UL}{\nu} \,. \tag{2.6}$$

The Reynolds number represents one of the most important non-dimensional numbers in fluid mechanics and can be interpreted as the ratio of inertial forces to viscous forces. It is named after Osborne Reynolds who pioneered the investigation of the transition between laminar and turbulent flows in the late nineteenth century. For low values of the Reynolds number, viscous effects dominate which results in smooth and sheetlike laminar flows which are deterministic in nature. Consequently, laminar flows can be treated easily using analytical approaches. With increasing values of the Reynolds number, small perturbations in the flow field are no longer immediately damped by viscous effects and the flow becomes gradually more unstable until a fully turbulent transition is achieved. In fully turbulent flows, the small perturbations yield large fluctuations in the velocity field, and the flow completely loses its deterministic nature.

While it is difficult to give an exact definition of turbulence, there are different properties and characteristics which can be attributed to turbulence 120:

- Turbulence is inherently chaotic. Stemming from the strong non-linearity of the convective term of the Navier-Stokes equations, the solutions are very sensitive to disturbances in the initial or boundary conditions, even though the Navier-Stokes equations themselves are deterministic. As a consequence, turbulence can only be treated with statistical methods.
- Turbulence is a multi-scale and non-local phenomenon. The pressure term in the Navier-Stokes equations couples distant points with each other (in incompressible flows, every material point is dependent on all other points in the flow field). The multi-scale nature of turbulence manifests itself in the coexistence of turbulent structures of various shapes, sizes and time scales. This results in a large number of degrees of freedom which increases significantly with increasing values of the Reynolds number. Consequently, the numerical treatment of the Navier-Stokes equations in the form of direct numerical simulations (DNS) is only feasible for limited values of the Reynolds number.
- Turbulent flows are highly dissipative. Without a continuous supply of energy, either in the form of external forcing or the presence of mean shear, turbulence decays rapidly.
- Turbulence is three-dimensional. As already pointed out in eq. (2.5), the presence of turbulence is directly linked to three-dimensionality due to the vanishing vortex stretching term in two-dimensional space.
- Mixing in turbulent flows is greatly enhanced. This not only applies to momentum but also to passive and reactive scalars, e.g. the temperature, oxidizer and fuel. This very property is what makes turbulence so essential in a wide range of engineering applications.

2.1.3 Scales in Turbulent Flows

As mentioned above, turbulence is a multi-scale phenomenon. The general understanding is that kinetic energy is injected into the flow dependent large scales. From these large or integral scales, the energy is then converted in an energy cascade to consecutively smaller and smaller scales. Finally, the energy is dissipated by the viscosity at the smallest scales. The idea of this cascade of turbulent energy was introduced by Richardson [106]. During the transport of the energy to the smaller scales, the information about the large scales is progressively lost. Therefore, the smallest scales are expected to be independent of the flow type or geometry and are consequently isotropic and

homogeneous. The idea of statistical isotropy was first introduced by Taylor 116. The assumption of statistical homogeneity and isotropy significantly reduces the complexity of the equations and the analysis. The first promising attempt at quantifying the multi-scale nature of turbulence and assessing the non-locality was introduced by von Kármán and Howarth [121]. To assess the structure of turbulence, two-point correlations of the velocity field obtained at the positions x_j and x'_j with the separation vector $r_j = x_j - x'_j$ and the magnitude $r = |r_i|$ were considered. For isotropic flows, this resulted in the derivation of the equations for the longitudinal and transversal correlation functions $f = \langle u_1 u_1' \rangle / \langle u_1^2 \rangle$ and $g = \langle u_2 u_2' \rangle / \langle u_2^2 \rangle$, the so-called Kármán-Howard equation. Here and hereafter, $\langle \dots \rangle$ indicates averages. However, similar to the Reynolds averaged Navier-Stokes equations, the equations are unclosed due to a triple correlation $\langle u_i u_j u_k \rangle$ in the non-linear convective transport term [107]. Consequently, the Kármán-Howard equation constitutes only the first equation in an infinite series of consecutively higher moment equations, which in their entirety contain all statistical information [85].

Although there is a multitude of different length scales and definitions thereof, the following are used most frequently in experimental and numerical investigations of turbulent flows and are used throughout this thesis:

The integral length scale \(\ell_t\): the integral length scale is a large scale which
is characterised by the flow geometry and the boundary conditions. For
example, the characteristic geometrical length scale can be proportional
to the pipe diameter in a pipe flow, nozzle diameter in a jet flow or the
cylinder bore in an internal combustion engine. Indicating the extent of
uniformly moving fluid volumes, it is defined as

$$\ell_{t} = \int_{0}^{\infty} f(r) dr. \qquad (2.7)$$

The corresponding Reynolds number can be formulated as

$$Re_L = \frac{u'\ell_t}{\nu}, \qquad (2.8)$$

where u' is the root mean square of the velocity fluctuations indicating the characteristic velocity of integral scale eddies.

• Taylor scale λ : The Taylor scale is situated between the large and the smallest scales. Originally introduced by Taylor [116], it is related to

the curvature of the velocity two-point correlations f and g in the limit of $r \to 0$. The Taylor microscale is defined by

$$\lambda = \left(-\frac{1}{2} \left. \frac{\partial^2 f(r)}{\partial r^2} \right|_{r=0} \right)^{-1/2} . \tag{2.9}$$

Using the Taylor scale as the characteristic length scale, the corresponding Reynolds number is

$$Re_{\lambda} = \frac{u'\lambda}{\nu}$$
. (2.10)

The Taylor scale based Reynolds number is often used in flow configurations where the integral scale is less meaningful or significantly changing, as in isotropic turbulence, decaying turbulence or mixing layers. The Taylor scale based Reynolds number allows for more comparability between flows of different configurations than the integral Reynolds number.

• Instead of assessing the multi scale nature of turbulence by the correlation functions f and g, Kolmogorov [72] used structure functions in the formulations of his famous similarity hypotheses. Structure functions are the statistical moments of the velocity difference $\Delta u_i = u_i - u_i'$ at the positions separated by the previously introduced spatial separation r_j . Similar to the two-point correlations, under the assumption of isotropy, structure functions can be expressed in the form of only two velocity components without the loss of generality. The arbitrary-order structure functions are then defined as

$$D_{m,n} = \langle (\Delta u_1)^m (\Delta u_2)^n \rangle. \tag{2.11}$$

From the equation of second-order structure function $D_{2,0}$ directly followed the first similarity hypothesis which states that for asymptotically large Reynolds numbers and in the viscous range $(r \to 0)$, the structure functions are only dependent viscosity ν and dissipation rate $\varepsilon = 2\nu \langle s_{ij}^2 \rangle$, where s_{ij} is the fluctuating strain rate tensor $1/2(\partial u_i'/\partial x_j + \partial u_j'/\partial x_i)$. Therefore, from dimensional consideration followed the Kolmogorov micro scale η , which is proportional to the smallest length scales in turbulent flows at which the turbulent kinetic energy is dissipated by viscosity:

$$\eta = \left(\frac{\nu^3}{\varepsilon}\right)^{1/4} \,. \tag{2.12}$$

Of course, the substantial insight gained through structure functions is not limited to the first similarity hypothesis, but extends among many other contributions to the second similarity hypothesis and the famous 4/5-law.

The ratios of the different length scales can be expressed by the Reynolds numbers

$$\frac{\ell_{\rm t}}{\eta} \sim \text{Re}_L^{3/4},\tag{2.13}$$

and

$$\frac{\ell_{\rm t}}{\lambda} \sim \text{Re}_L^{1/2} \,. \tag{2.14}$$

With an increasing value of the Reynolds number, the ratios of the scales increase as well. Consequently, the Reynolds number indicates the scale separation or in other words, the degrees of freedom of the flow.

2.1.4 Geometries in Turbulent Flows

The inherent difficulties in understanding turbulence are linked in great part to the previously mentioned multi-scale and non-local characteristics. Today, even in the simplest and most thoroughly investigated case of isotropic decaying turbulence, no closed theory exists [75]. However, regardless of their non-deterministic, random nature and complexity, turbulent fields possess a structure. Consequently, attempts at recreating passive scalar mixing by using random Gaussian fields as a surrogate for the fluctuating velocity did not yield the desired results [74]. Different to Gaussian fields, distinct spatial structures are an important characteristic of turbulent fields. These spatial organizations in turbulent flows were first referred to as 'coherent structures' by Brown and Roshko [26] and linked to vortical motions.

Early and highly insightful statistical methods to evaluate non-local characteristics are the already introduced two-point correlations [116] and structure functions [73] [72]. However, both of these approaches face significant challenges in flows which are characterized by high levels of anisotropy. This is especially true for typical turbulent combustion configurations, where the anisotropy caused by external intermittency is additionally exacerbated by high spatial gradients of the material properties of the fluid. As a consequence, the analysis based on two-point correlations and structure functions suffers from the following challenges:

• Once isotropy no longer applies, using only two velocity components in the formulation of both structure functions and correlation functions reduces the generality of the methods. Therefore, a second transversal velocity has to be taken into consideration with implications to the derivation and interpretation of the equations.

- Due to the assumption of isotropy, statistics are independent of the direction r_j and consequently only a function of the magnitude r. In the context of reacting flows, it can be easily imagined that statistics obtained with r_j pointing in the normal direction to a flame front will differ significantly from statistics obtained tangential to it. Similarly, the absolute position x_j , which is of no consequence in an isotropic flow, may significantly affect the results obtained with the two statistical methods.
- Lastly, independent of isotropy, applying the averaging procedure \(\ldots \ldots \right) may lead to a loss of important local flow dynamics present in the instantaneous fields.

Consequently, it is questionable whether the Cartesian frame in which the traditional theories are developed might be counterproductive and if instead a flow intrinsic frame of reference might be advantageous. Corrsin [35] therefore asked the question "What types of geometry are naturally identifiable in turbulent flows?" Following this paradigm, different approaches to identifying natural geometries, usually linked to vortex structures, were pursued [110]. However, vortex tubes and sheets have the severe flaw of not allowing for a space filling and unique decomposition of the flow field. This challenge was overcome by Wang and Peters [127] with the concept of dissipation elements. This method and the turbulent structures identified in this fashion pose an integral part of this thesis. Dissipation element analysis is explained in detail in Chapter. [3.1] where its added benefits in the investigation of reacting flows are further highlighted.

2.2 Introduction to Turbulent Combustion

Complementary to the fluid motion described by the Navier-Stokes equations, the thermo-chemical state of the flow can be described by the transport equations of the species mass fractions Y_{α} , with the index α indicating the species and a form equation of the energy E. These equations and the numerical methods used in solving them are discussed in detail in Section 4.2

The fundamental difference between the equations for the species mass fraction and the temperature and the Navier-Stokes equations is the absence of the non-linear transport term present in the momentum transport eq. (2.1). Therefore, if the flow field is laminar (or the Péclet number $Pe = UL/D_{\alpha}$ is low due to a large diffusion coefficient D_{α} of the reactive scalar), both species mass fractions and temperature are deterministic. The deterministic nature of the thermo-chemical field is underlined by the results of the first mathematical description of premixed combustion, the thermal flame theory by Zeldovich and Frank-Kamenetski [131], which yielded that the laminar burning velocity $s_{\rm L}$ is largely independent of the flow field and is mostly determined by the material properties of the fuel and oxidizer.

However, once the flow field is turbulent, this no longer applies. In turbulent flow fields, the range of different size eddies, described in Section 2.1.3 induces strain and shear which greatly enhance the mixing. The sharp interfaces between these turbulent structures result in locally significantly steeper gradients of the reactants' concentrations, the heat release greatly increases in turn. The molecular mixing of fuel and oxidizer poses a requirement in the first place for any combustion process.

2.2.1 Non-dimensional Numbers in Turbulent Combustion

However, compared to the turbulent mixing of a passive scalar, a couple of differences apply. Foremost, the heat release from the combustion chemistry increases the temperature. Due to the exponential influence of the temperature on the reactivity, in turn greatly increases the heat release. In the combustion of hydrocarbons, the high value of the heat release causes this self-amplification to result in relatively thin layers in which intense chemical activity takes place. Besides the enhanced mixing aspect, this poses the question to which extent the combustion chemistry and turbulent scales interact.

Traditionally, to help gauge the scale interaction, non-dimensional numbers are used. The most widely used non-dimensional numbers which will be utilized throughout this thesis will be discussed in the following section.

• The Damköhler numbers Da are used to relate the time scales to the characteristic time scales of the transport mechanisms to the chemical time scale. In the turbulent context, the turbulent Damköhler number is defined as

$$Da_{\tau} = \frac{\tau}{t_{\rm F}} \,. \tag{2.15}$$

Therefore, Da_{τ} can be interpreted as the ratio of the integral turbulence time scale to the characteristic flame time scale $t_{\rm F}$. There are multiple definitions of the characteristic flame time scale depending on the context.

For example, in premixed combustion, the characteristic flame time scale may be defined as $t_{\rm F} = \ell_{\rm F}/s_{\rm L}$ with the flame thickness $\ell_{\rm F}$. In non-premixed combustion, a common definition is $t_{\rm F} = \chi_{\rm q}^{-1} Z_{\rm st}^2 (1 - Z_{\rm st})^2$ with Z_{st} denoting the stoichiometric mixture fraction and $\chi_{\rm q}$ denoting the quenching scalar dissipation rate at stoichiometric conditions in a laminar counterflow configuration.

• To compare the other end of the turbulent spectrum to the flame scales, the Karlovitz number *Ka* is utilized

$$Ka = \frac{t_{\rm F}}{t_n} \,. \tag{2.16}$$

It constitutes the ratio of the characteristic flame time scale to the smallest turbulent time scale. For premixed combustion, the Karlovitz number can also be defined in terms of length scales

$$Ka = \frac{\ell_{\rm F}^2}{\eta^2} \,.$$
 (2.17)

Consequently, different characteristic length scales of the flame can be used to define the Karlovitz number.

As these two non-dimensional numbers represent a comparison of the flame scales with both ends of the turbulence spectrum, they can be related to the integral Reynolds number in unity Schmidt number flows [91]

$$Re_L = Da_\tau^2 K a^2 \,. \tag{2.18}$$

This relation neatly demonstrates the increased complexity of adding combustion to turbulent flows. For typical combustion conditions and the corresponding values for the Damköhler number and the Karlovitz number encountered in engineering applications, the resulting Reynolds number is likewise very high. The already large number of degrees of freedom stemming from the flow field is then greatly expanded by the number of reacting scalars needed in the description of the thermo-chemical state.

For premixed combustion, the degrees of interaction between turbulence and combustion can be organized in the form of a regime diagram, the so-called "Borghi-Peters-diagram" $\boxed{19}$ $\boxed{95}$. Here, regimes of premixed combustion are defined by both length scale and velocity ratios. Utilizing the relation eq. $\boxed{2.18}$, the combustion regime boundaries are expressed with the non-dimensional numbers Re and Ka. Self-evidently, the former is used to distinguish between

laminar and turbulent combustion. The Karlovitz number is defined twofold; once as shown in eq. (2.17) relating the flame thickness Kolmogorov micro scale and using a much smaller characteristic flame scale, relating η to the thickness of the inner reaction zone ℓ_{δ}

$$Ka_{\delta} = \frac{\eta^2}{\ell_{\delta}^2} \,. \tag{2.19}$$

For Ka < 1, the laminar flame structure is expected to be unperturbed, as it is exceed in size by even the smallest turbulent structures. These combustion conditions are additionally classified by $u' < s_{\rm L}$ into the "wrinkled flamelets" regime, in which the influence of turbulence is further diminished as even the integral sizes eddies are outpaced by the laminar flame speed and by $u' > s_{\rm L}$ into the "corrugated flamelet" regime.

The combustion conditions with Ka > 1 and $Ka_{\delta} < 1$ are classified as the "thin reaction zones" regime. Here, turbulent eddies can penetrate the diffusive-reactive flame structure. As a consequence, a thickening of the preheat zone is expected as turbulence transports the temperature ahead of the propagating flame front. However, due to scale separation, the inner reaction zone remains unaffected. Lastly, for $Ka_{\delta} > 1$ in the "broken reaction zones" regime, turbulent mixing affects the highly reactive species in the inner reaction zone.

These considerations are among many other aspects immensely helpful in gaining an intuitive access to the complicated subject of turbulent combustion. However, the presented regime diagram is in essence limited to two characteristic flame scales, $\ell_{\rm F}$ and ℓ_{δ} . Yet, each of the vast number of elementary reactions present in the combustion of hydrocarbons possess an individual characteristic time scale. Therefore, once the unity Karlovitz number is departed, the interaction between turbulence and combustion chemistry will be governed by an increasing overlap and the consequent interplay of two spectra of turbulence scales and flame scales.

2.2.2 Models for Turbulent Combustion

As previously established, the large number of degrees of freedom and lack of analytical solutions make a direct numerical approach for solving the extensive system of equations comprised of the conservation of mass, momentum, species and energy equations unfeasible in real world conditions. Further exposition and a more detailed estimate of calculation costs will be discussed in Chapter 4. Therefore, to resolve the crucial task of solving engineering problems involving turbulent combustion, models for turbulent combustion are indispensable.

Thereby, the development of turbulent combustion models draws from the insights and success of turbulence models employed in non-reacting flows. In these largely statistical moment based approaches, the important yet unclosed turbulent mixing (or sub-filter transport in large eddy simulations) is solved by closure hypotheses which rely on dimensional arguments and require empirical input. In addition to the unclosed transport, the source terms in the species and energy equations present an additional closure problem faced in reacting flows. Due to the exponential dependency of the reaction rate coefficient on the temperature, even small turbulent fluctuations of the temperature field can lead to a significant increase or decrease of the reactivity. Due to this highly non-linear behavior, the traditional moment method closures adopted from non-reacting turbulence models are less suitable.

To overcome this challenge, the previously introduced non-dimensional numbers are used to describe the interaction between turbulence and the combustion chemistry and classify the combustion into regimes. Model assumptions are then applied based on these regimes.

- In the limit of $Da_{\tau} \to \infty$ or $Ka \ll 1$, the turbulent scales greatly exceed the combustion scales to the point where the scale separation causes the source terms to be completely unaffected. From the 'perspective' of the turbulence, the chemistry is infinitely fast and modeled accordingly. Characteristic examples for these models are the Burke-Schumann model [28] for non-premixed combustion or the Bray-Moss-Libby model [23] for premixed combustion.
- In the completely opposite limit, $Da_{\tau} \to 0$, the turbulent mixing is infinitely fast compared to the chemical time scales. Consequently, the reacting fluid is perfectly homogenized by turbulent mixing $(\partial/\partial x_i = 0)$ and the vanishing transport terms in the governing equations lead to a system of ordinary differential equations; the homogeneous reactor.
- Finally, for $1 \ll Da_{\tau} \ll \infty$ or Ka < 1, the limit of fast but not infinitely fast chemistry, the combustion chemistry is affected by the turbulent flow field. However, due to the still very thin nature of the reaction layers, the coupling between the turbulent velocity field and the chemistry can be fully described with adequate turbulent one-point quantities. Therefore, only very limited, non-local information is required, which is usually supplied in the form of meaningful gradient based quantities such as the scalar dissipation rate χ or the strain rate a. These conditions are commonly referred to as the "Flamelet Regime" in which the combustion resembles an ensemble of thin stretched laminar flames attached to a

turbulently wrinkled flame front. The Flamelet Model for non-premixed combustion [93] and for premixed combustion [24] or the *G*-equations for the thin reaction zones regime [95] are a few examples for combustion models in these conditions.

2.3 Outline of the Thesis

The previous short introduction to turbulent combustion and the combustion regimes left two elementary questions unanswered. Foremost, what are the combustion conditions as the regime of high scale interaction $Da_{\tau} \approx 1$ is approached? The expected interplay between fine scale turbulent mixing and the short lived radical species usually only found in the inner reaction zone implies that the traditional view of the flame as a diffusively dominated structure is dissolved. The inherent difficulty in both analyzing and modeling these conditions lies in the problem that two structures of finite sizes are interacting and thus have to be compared. To reiterate, the advantage in viewing either turbulence or the combustion chemistry as thin/fast compared to the other allows for the justified assumption of treating the coupling between the velocity field and the reacting scalars with one-point statistics. Consequently, the need for a definition of a turbulent structure is avoided. As briefly discussed in Section 2.1.4 defining coherent structures in the chaotic turbulent fields is a substantial challenge. This challenge is further complicated by the additional requirement that the definition of the turbulent structures must be meaningful in the given context of turbulent combustion.

The second elementary question follows implicitly from the usage of combustion models. The quality of the modeling results is directly linked to the correct assumptions regarding the combustion regime. This traditionally requires a certain experience and a limited preexisting knowledge of the system to be simulated. In a substantial number of operation points or in the very limits of infinitely fast or slow chemistry, this seems trivial. However, at which point does the assumption of fast chemistry quantitatively cease its validity? In a large variety of combustion systems, like internal combustion engines, the boundary conditions of the combustion process change rapidly and drastically in time. Similarly, the combustion regimes are expected to change. Other effects which cause uncertainties with regards to this choice might be linked to the high anisotropy observed in these flows which results in locally lower or higher values for the Damköhler number. Lastly, given the multi-scale nature of turbulence, the coexistence of combustion regimes in a turbulent flow seems very plausible. This poses the question if, instead of

relying on fixed regime assumptions, a systematic identification and prediction and consequent modeling of combustion conditions is feasible. To not average out flow dynamics or locally existing regimes, the investigation of this question is again directly linked to a robust definition of turbulent structures to achieve a local flame analysis instead of a purely statistical approach.

The method of choice of identifying coherent structures in this thesis is the Dissipation Element (DE) analysis. In Chapter [3] an introduction to the DE analysis is given. DEs provide a procedure for compartmentalizing scalar fields into physically meaningful sub-units which provide a direct measure for turbulent scales. Furthermore, DEs enable a variety of additional ways of investigating non-local effects in reacting and non-reacting turbulent flows. After the underlying physical ideas of dissipation elements are explained and a parameterization of DEs is defined, the method of detecting DEs with gradient trajectories is explained and physical and numerical prerequisites to the analyzed flows are presented. Common characteristics of DEs are interpreted and self-similar properties of DE parameter statistics are highlighted which make an approach using DEs especially desirable for potential combustion models.

In Chapter 4 a short introduction to direct numerical simulations (DNS) of reacting turbulent flows on theoretical and methodological grounds is given. The configurations of the DNS conducted for this thesis are explained and the specific combustion conditions, which focus on the departure from the flamelet regime, are justified. The chapter is concluded with a short flame analysis of the conducted DNS.

Chapter 5 is dedicated to the investigation of turbulent non-premixed combustion. To investigate non-premixed combustion, DE analysis is applied to the mixture fraction fields of a series of datasets from DNS of non-premixed temporally evolving jet flames with jet Reynolds numbers ranging from 4,500 to 10,000 and varying stoichiometric mixture fractions. Statistics of the DE parameters of non-premixed flames are compared to those obtained from non-reacting jets. It is found that the universality of the normalized length distribution of the DEs observed in non-reacting cases also holds true for the reacting flows. The characteristic scaling with the Kolmogorov scale η is obtained as well. The effects of combustion on the scalar difference in the DEs are shown and are found to diminish as the Reynolds number and the fuel dilution are increased. The DEs provide the means for a local comparison of the turbulent and characteristic flame scales. A regime diagram for non-premixed combustion is introduced using the DE parameters for a local classification of the turbulent flame surface into flamelet-like zones and fine-scale mixing

zones in addition to the burning and non-burning zones. The soundness of the regime diagram and the potential consequences for combustion modeling in the individual regimes is demonstrated by the investigation of the correlation between the chemical field and the DE parameters in the individual regimes.

Premixed combustion is analyzed in Chapter 6. DE analysis is applied to the temperature fields of a set of DNS of spatially evolving premixed jet flames at different values for the Reynolds number and approximately constant Karlovitz numbers. The variation of the jet Reynolds number, ranging from 5,600 to 22,400 is achieved by increasing the width of the jet and keeping the bulk velocity constant, which also implies an approximately constant value of the turbulence intensity across the flames. The flames considered are nominally situated in the thin-reaction zones regime.

Again, the invariance of the normalized length distribution of the DEs toward changes in the Reynolds number observed in non-reacting flows holds true for the reacting cases and the characteristic scaling with Kolmogorov micro-scale is reproduced. However, the joint DE statistics reflect the influence of the chemical source term present in the temperature field and the resulting imprint of the premixed flame structure on the turbulent scalar fields.

Further, an analysis of the combustion process along gradient trajectories is presented. The thickening of the inner reaction layer and its enhancement with increasing values for the Reynolds number is linked here to the presence of extremal points in the temperature field in the vicinity or inside the inner reaction layer, and therefore to the interruption of the flamelet structure by turbulence and not by the thickening of the entire flamelet itself. In addition to the expected strong thickening of the formaldehyde layer, the layers of species which are not usually present in the preheat zone, show a significant thickening and these species are observed several flame thicknesses ahead of the turbulent flame surface. Finally, it is shown that in the regions where the inner reactive layer is thickened, the local fuel consumption rate is reduced in comparison to a laminar planar flame. However, the total burning rate integrated over the entire flame structure across the flame surface is larger due to the increased volume of the reactive layer. These observations highlight the importance of assessing the balance between two competing phenomena related to high Karlovitz numbers, the effect of turbulence strain and stirring on the chemistry, which usually decreases the local burning rate, and the effect on the species fields. These species fields then might experience modifications in their topology, such as the introduction of local extremal points and significant thickening of the volumes between their iso-surfaces.

This thesis concludes in Chapter 7 with the application of the insights

gained from the investigation presented in the previous chapters to combustion modeling. The DE parameter based regime diagram for non-premixed combustion is used in conjunction with the characteristic scaling of the DE parameters and the self-similarity of the DE parameter statistics in a modelling framework for the prediction of combustion regimes in computational fluid dynamics simulations (CFD) of engineering applications. The prediction modeling framework is applied to simulations of a passenger car direct injection diesel engine in multiple operation points. The results of the modeling procedure are presented and critical operation parameters are discussed.

Finally, a novel modeling approach for the probability density function (PDF) of the mixture fraction is proposed which uses DE paramter based statistics. The PDF of the mixture fraction is of integral importance to a large number of combustion models. Here, while being restricted to the commonly used mean and variance of the mixture fraction, this model approach individually considers contributions of the laminar regions as well as the turbulent core and the turbulent/non-turbulent interface region. The latter region represents a highly intermittent part of the flow which is of high relevance to the non-premixed combustion of pure hydrocarbon fuels. The new DE based model is validated against the DNS datasets and a comparison with the predominantly used β -PDF is presented.

3 Introduction to Dissipation Element Analysis

3.1 Introduction to Dissipation Elements

The sheer volume of data obtained from direct numerical simulations (DNS) poses a challenge in itself for any analysis of turbulence and turbulent combustion. If the non-deterministic behavior of turbulence is added on top, the complexity is increased to a point where novel methods of analysis are inevitably required to gain deeper insight into this physical phenomenon that defies complete comprehension regardless of the best efforts of many generations of researchers. A desirable quality of a method for the analysis of turbulent flows is the ability to break down the complexity of the entire turbulent domain into smaller structures which are ideally simple enough for an intuitive consideration. At the same time, this method of analysis needs to be robust and efficient enough to cope with the vast amount of data generated by modern large scale DNS. A potential method for the analysis for turbulent flows that fulfills these requirements is the dissipation element (DE) analysis.

3.1.1 Definition of Dissipation Elements

The inherent challenge of analyzing turbulent flows stems from the complexity introduced by the chaotic and multi-scale nature of turbulence. A way to overcome this challenge and gain a deeper insight is to compartmentalize the entire turbulent field and its scales into simpler sub-units. If the criteria for compartmentalization are chosen sensibly, the analysis of these sub-units is far less complex and the comprehension of more detailed structures and correlations is possible.

Other scale-decomposing methods exist including the Fourier transform, the wavelet transform and proper orthogonal decomposition, and these methods have their individual advantages for linear problems. However these methods are less valuable for the understanding of the nonlinear interactions in turbulence or have limited applicability in flow configurations which display high levels of anisotropy.

Another desirable characteristic of a compartmentalization method for turbulent flows is the space-filling and non-overlaping nature of the sub-units.

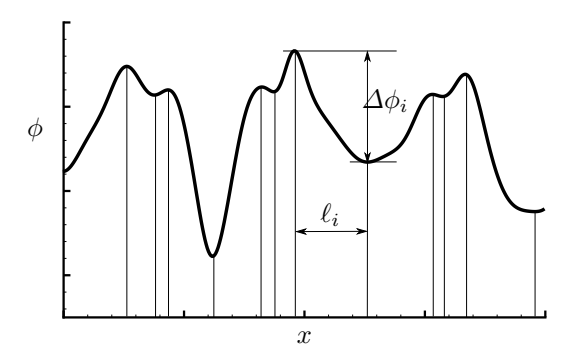


Figure 3.1: Schematic representation of a DE and its parameters in one-dimensional space. ℓ_i indicates the linear distance and $\Delta\phi_i$ the scalar difference of the *i*th DE in the scalar profile.

To ensure that all physical effects in the turbulent domain are considered, all material points must be uniquely assigned to a sub-unit. While systematic approaches for the space-filling decomposition exist, such as the velocity gradient tensor Q and pressure p based approach $\boxed{130}$, these methods suffer from the arbitrariness introduced from the setting of threshold levels. Finally, the method to decompose turbulent domains should ideally yield results that are easy to interpret in a physical way, as well as the potential for a model development.

A physically motivated method for such a compartmentalization of scalar fields in turbulent flows that meets all mentioned requirements is the dissipation element (DE) analysis [98]. DEs are ensembles of material points in which the underlying scalar behaves monotonically, i.e., the space in between the turbulence-introduced extremal points. To illustrate the identification of DEs in a one-dimensional setting, a schematic profile of a scalar ϕ in physical space is shown in Fig. [3.1]. An intuitive way for a quick estimation of scales in turbulent profiles or signals is to observe the local extremal points and judge the spacing between the minima and the maxima. In 1D, DE analysis does the exact same procedure: first, all extremal points in the scalar field are identified. Second, the segments of space linking individual pairs of minima and maxima are then classified as DEs. The DE identified in this way can then be parametrized by its pair of extremal points. The DE length of the ith DE is defined as the separation distance of the minima and maxima in physical space $\ell_i = |x_{\text{max},i} - x_{\text{min},i}|$ and the DE scalar difference is defined

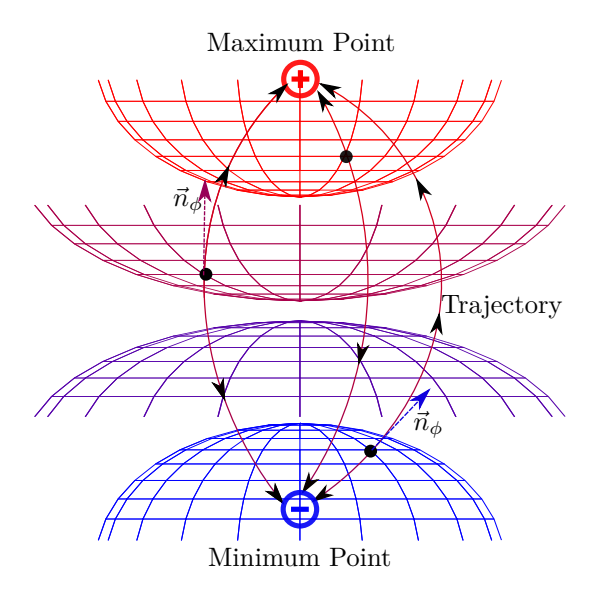


Figure 3.2: Schematic representation of gradient trajectories connecting the same extremal points in three dimensional space. The grids represent different iso-surfaces of the scalar ϕ . The black dots indicate material points where gradient trajectories are started in the DE detection process.

as the difference of the scalar in these extremal points $\Delta \phi_i = \phi_{\max,i} - \phi_{\min,i}$. These two parameters are henceforth called DE parameters. Additionally, the mean DE scalar gradient is calculated as $g_i = \frac{\Delta \phi_i}{\ell_i}$, which takes the steepness of the entire sub-unit into consideration.

The numerical procedure of DE analysis is trivial for a 1D case, but serves to illustrate the underlying intuitive idea of obtaining scales in this fashion. In higher dimensional spaces, the number of DEs linked to each extremal point is not limited to two. Additionally, the treatment of critical points in the scalar fields gets more complicated as the dimensionality is increased. To link the extremal points in scalar fields in 2D and 3D space, gradient trajectories of ϕ are employed. Starting from any material point, the direction of the scalar gradient $\vec{n}_{\phi} = \frac{\nabla \phi}{|\nabla \phi|}$ is calculated. The gradient trajectory can be determined by tracing along descending $-\vec{n}_{\phi}$ and ascending directions \vec{n}_{ϕ} . This can be interpreted as moving in the normal direction from each iso-surface of ϕ to the next. The gradient trajectories are traced until they terminate at a maximum in the ascending direction and at a minimum in the

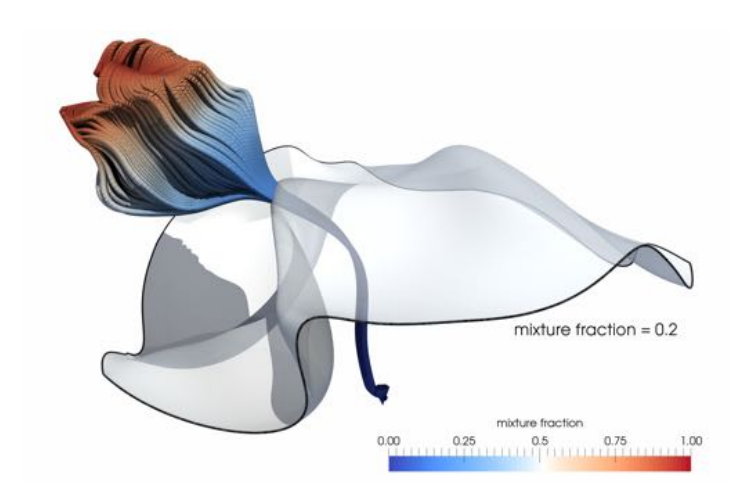


Figure 3.3: A DE in the mixture fraction field Z in a DNS of non-premixed temporally evolving jet flame. The DE is represented by the gradient trajectories used in the detection process. The gradient trajectories are colored by the local value of the passive scalar. The grey iso-surface indicates the position of the stoichiometric mixture fraction.

descending direction, whereby the definition of extremal points the gradient of ϕ is zero. This procedure in 3D space is illustrated for three exemplary material points and their gradient trajectories in Fig. [3.2]. The ensemble of material points linked to the same pair of extremal points in a scalar field is then classified as a DE. It is easy to see that each material point is uniquely assigned to a single DE and since all material points can be assigned, the method provides a space-filling compartmentalization. Therefore, the scalar field itself provides the geometry of the sub-units and the obtained scales are an intrinsic result of the flow.

While the definition of the DE scalar difference $\Delta\phi$ remains the same in higher dimensional fields, the DE length is defined as the Euclidian distance between the minimum and the maximum $\ell = |\vec{x}_{\rm max} - \vec{x}_{\rm min}|$. The arc-length s of the gradient trajectories between the extremal points might be a more obvious choice to characterize the length of the DE, but s differs slightly based on the location of the different material points in one DE and is therefore not unambiguous.

A DE obtained from a scalar field from a 3D DNS of a planar temporally

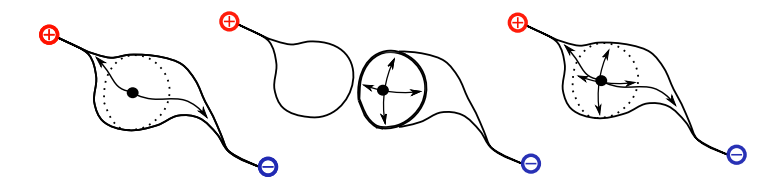


Figure 3.4: Schematic representation of the potential methods of obtaining spatial statistics in the DE decomposed space. Left: obtaining statistics along the gradient trajectories of the individual DE. Middle: obtaining statistics on an iso-surface (such as mixture fraction or temperature) intersecting the DE. Right: using the DE volume as a frame of reference for statistics.

evolving non-premixed jet flame is shown in Fig. 3.3 Additionally, a section of an iso-surface of the scalar is shown to further illustrate the tracing of gradient trajectories in the normal direction from iso-surface to iso-surface. In the three-dimensional space, DEs display various shapes and sizes. The overall orientation of each DE, as well as the trajectories used in its detection, proceed approximately in the direction of the straight line connecting the two extremal points. A common characteristic shared by most DEs is the converging of all gradient trajectories as the extremal points are approached. As a multitude of DEs are connected to a single extremal point, these elements form interwoven and entangled structures in 3D space.

While the space-filling parametrization of the turbulent scalar fields by means of the DE already yields a plethora of applications in the analysis of turbulent flows, a lot of physical insight can be gained by using individual DEs as a non-abitrary and meaningful frame of reference for obtaining spatial statistics. As mentioned above, DEs are regions of monotonic scalar between extremal points. The diffusive flux of ϕ is defined as $J = -D_{\phi}\nabla\phi$, where D_{ϕ} is the diffusion coefficient of the scalar. Therefore, it is easy to see that the diffusive flux is interrupted in the extremal points of the scalar field as J = 0, since by definition in these points $\nabla \phi = 0$.

Selected methods of using DEs for obtaining spatial statistics are shown in Fig. 3.4. In the cartoon of a DE on the left side, the gradient trajectories are used for obtaining statistics in the normal direction. This provides the ability to obtain structure-function-like statistics along physically meaningful directions and overcome the inherent difficulties in anisotropic flows. A second method is to obtain statistics in the tangential direction on the intersection area of an iso-surface and a DE. This is shown for the cartoon of a DE in

the middle of Fig. 3.4 Material points on the vertices of the iso-surface of ϕ are chosen as the starting points of the gradient trajectories, uniquely linking sections of the iso-surface to DEs. This is especially useful for scalars which possess physically meaningful absolute values. An example of this was already shown in Fig. 3.3 where the indicated iso-surface is the stoichiometric mixture fraction $Z_{\rm st}$ which indicates the position of the reaction zone in non-premixed flames. Finally, as shown by the DE cartoon on the right side of Fig. 3.4 the entire DE volume can be used to obtain statistics like variances, minimum or maximum values and other quantities of interest in each DE.

DE analysis lends itself for tracking the temporal evolution of features in time-varying data. Especially when temporal events involving the DEs, like splitting, merging or annihilation, can be meaningful interpreted in the context of the analyzed scalar and physics, this becomes a very powerful tool. Recently, a robust algorithm was developed which determines the assignment of DEs between two successive time-steps by solving two graph optimization problems 109. It first resolves one-to-one assignments of DEs by computing a maximum-weight, maximum-cardinality matching on a weighted bi-partite graph. Second, the algorithm detects temporal events by creating a graph of potentially conflicting event explanations and finding a weighted, independent set in it.

3.1.2 Physical and Numerical Considerations

The applicability of the DE analysis to a given scalar field depends on several prerequisites, which are of the physical nature of the scalar field and numerical properties of the simulation which provided the scalar field.

Whether a scalar field can be sensibly decomposed into DEs depends on the following characteristics of the scalar [123]:

- 1. Gradient trajectories must end at definite points without spiralling infinitely.
- 2. Trajectories and DEs should not be trivial, but display natural and intrinsic characteristics of turbulent fields. For instance, trajectories should neither pass through the entire flow field to be infinitely long, nor be infinitesimally small.
- 3. The tracing process of trajectories should be relatively stable both analytically and numerically, to resist the perturbation from the inaccuracy of flow fields, or else a unique decomposition of the entire flow field into DEs will not be possible.

Most scalar fields obtained from DNS of turbulent flows satisfy these three conditions if certain numerical prerequisites in the DNS are met. Regarding the first characteristic, it was shown that in a sufficiently smooth scalar field the length of a gradient trajectory will be finite [37]. This implies that since the length of the gradient trajectory is bounded, an infinite spiralling loop should not be possible if the numerical schemes and resolution in the DNS are adequate to provide a sufficiently smooth scalar field.

Satisfying the second condition is linked to a significantly high enough Reynolds number of the flow. If the gradient trajectories can extend over the entire integral scale of the flow, characteristics of the turbulent scales will not be reflected by the DEs due to the lack of scale separation. Transport of most scalars in turbulent flows is governed by the balance of advective and diffusive terms. The former introducing extremal points and the latter removing them. A scalar field dominated by diffusive transport makes a poor choice for DE analysis. Therefore, additional attention should be paid to the Schmidt number of the scalar $Sc_{\phi} = \nu/D_{\phi}$, where ν is the kinematic viscosity. Scalars with very low values of Sc_{ϕ} may not be suitable to estimate turbulent scales accurately even if the the Reynolds number is sufficient to result in a well developed turbulent flow field.

The third requirement of the robustness of the traced trajectories against small perturbations is ensured by the previously mentioned diffusion processes in turbulent flows. In the inertial range of turbulence, where viscous effects can be neglected, the random motions of eddies will cause the iso-surfaces of scalars to be highly corrugated. Recalling the analogy between the gradient trajectory tracing and the movement in normal direction from iso-surface to iso-surface, small perturbations caused by inaccuracies will quickly lead to faulty pathing of the gradient trajectories. However, in the viscous range, diffusion smooths the corrugation of the iso-surfaces caused by the turbulent eddies. It follows that the tracing of the gradient trajectories must be performed well below the inertial scale 123. The consequence for the DNS is the requirement of well resolved viscous scales. This observation implies that DE analysis for scalars obtained from large eddy simulations or experiments that do not resolve the viscous turbulent scales might be problematic.

Treatment of Critical Points

In a scalar field, all material points can be classified as critical points and noncritical points. If $\nabla \phi = 0$ is zero at a certain point, this point will be critical. The tracing of the gradient trajectories relies on a well defined direction \vec{n}_{ϕ} . Due to the previously mentioned physical characteristics of typical scalars

in turbulent flows, this is ensured in noncritcal points. Therefore, critical points need to be treated differently. In 3D space, based on the eigenvalues of the Jacobian $\vec{J}_{\phi} = \nabla \nabla \phi$, four types of critical points can be classified for viscous scalar fields: sources, sinks, repelling node saddles and attracting node saddles [50]. As trajectories converge or diverge in straight lines in all of these critical points, analysis and treatment is fairly simple. Regardless, differences between the extremal points and saddle points need to be taken into account.

Saddle points are mathematically not stable and the trajectories in the vicinity of these points can be diverted by a small perturbation, while extremal points are stable and their position can be identified in a robust manner even if small perturbations are present. Due to the fact that the scalar fields used to trace trajectories are diffusion controlled at small scales, the scalar gradient vectors around extremal points will point away from a minimum and in a straight line towards a maximum without rotation.

As soon as the scalar gradient decreases below a certain value compared to the mean gradient in the proximity, an extremal point is expected in the immediate vicinity. Therefore, Wang [123] defines the detection threshold ϵ as the ratio of the local scalar gradient to the mean gradient in the surrounding grid points. The extremal point will be encapsulated by a spherical iso-surface of a scalar value close to the one in the extremal point. The radius of this sphere r depends on the threshold ϵ . For an exemplary threshold of $\epsilon = 2 \cdot 10^{-5}$ (which was used in all of the DE analyses shown in the following sections) the radius of the containing sphere will be $r = 0.02\Delta$, with Δ being the grid spacing between surrounding points. Under the assumption of sufficient numerical resolution and the assumption that the expected critical point is located exactly at the center of the sphere, the local curvature $\kappa = \nabla \cdot \vec{n}$ can then be used to identify the type of critical point. For $\kappa = -6$ a maximum is detected, while for, $\kappa = 6$ a minimum and $-2 \le \kappa \le 2$ a saddle are identified.

In case of a detected extremal point, the gradient trajectory tracing can be stopped for the material point. In case of the a saddle point, the gradient trajectory needs to be artificially perturbed, i.e. numerically moved for a small step size in a random direction. However, this procedure is only necessary in the exceedingly rare event that a chosen material point is situated on a saddle point.

From these considerations, it is easily seen that the requirements of the resolution of the DNS exceed the commonly used minimum requirements of $\Delta/\eta \leq 2.1$ [104]. Based on the numerical schemes employed in the DNS, lacking numerical resolution leads to an introduction of false extremal points, if spectral methods are used. Otherwise, extremal points are removed if

the numerical diffusivity of the scheme is too high. Clearly, both effects might change the results of the DE analysis. For DNS of isotropic turbulence employing spectral methods, it was found that results of DE analysis do not change for resolutions of $\Delta/\eta \leq 1$ 123. The same restrictions of $\Delta/\eta \leq 1$ apply to central finite difference schemes and weighted ENO 68 schemes used in the DNS in this work.

3.2 Statistics of Dissipation Element Parameters

Instead of indirectly obtaining turbulent scales by relating other statistical turbulence quantities to each other, for example expressing the integral length scale as $l_t \sim k^{3/2}/\varepsilon$, with the turbulent kinetic energy k and the dissipation rate ε , DE parameters provide scales which are obtained directly from the turbulent flow. The statistics of these parameters allow for some fundamental insight into the governing physical mechanisms and shall be discussed in this section.

3.2.1 Marginal Statistics and Scaling of mean DE Parameters

The probability density function (PDF) of the DE length $P(\ell)$ displays interesting characteristics as well as helps to understand the physical mechanisms governing the DE formation and annihilation. DE analysis was first applied to isotropic turbulence [127]. It was found that the PDF of the normalized DE length $\ell^* = \ell/\ell_m$, with the volume average mean DE length ℓ_m , shows a remarkable invariance towards changes in the Reynolds number. This invariance is independent of the scalar field the DE analysis is applied to and carries over to non-isotropic configurations [53], reacting flows [41] and was confirmed in experiments [52]. To demonstrate this, $P(\ell^*)$ is shown for isotropic turbulence as well as other selected cases in Fig. 3.5. These DNS include isotropic turbulence [20], a planar spatially evolving mixing layer [5], a planar temporally evolving non-premixed jet flame [38] and a planar spatially evolving premixed jet flame [41]. Even though the cases are vastly different in terms of the flow configuration and physical properties of the scalar, the PDFs show almost perfect collapse. All PDFs display two distinct features. For small ℓ , a linear increase is observed in the linear/linear scaled plot in Fig. 3.5 a). This linear increase corresponds to the diffusive drift of the extremal points towards each other and the subsequent annihilation of DEs. The second feature is the random cutting and reconnection of large DEs by turbulent eddies. This manifests itself in the exponential decrease of the PDF for large

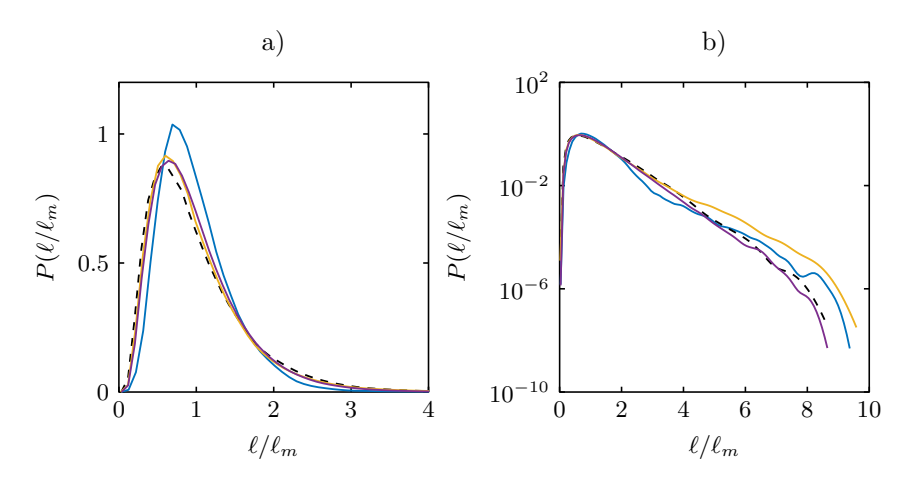


Figure 3.5: PDF of the normalized DE length ℓ/ℓ_m in a): linear/linear scale and b): linear/logarithmic scale obtained from DNS of various inert and reacting cases. (-): passive scalar in isotropic turbulence, (-): passive scalar in spatially evolving mixing layer, (-): mixture fraction in temporally evolving diffusion jet flame and (-): temperature in spatially evolving premixed jet flame.

 ℓ , which can be observed in the linear/logarithmic scale plot in Fig. 3.5 b). The scaling of the mean DE length is demonstrated in Fig. 3.6, where the ratio of the mean DE length and the Kolmogorov micro scale $\ell_{\rm m}/\eta$ is shown for selected flow configurations and Reynolds numbers. A clear Kolmogorov scaling can be observed for all cases. The absolute value of the ratio depends slightly on the scalar field the DE analysis was applied to. Therefore, normalizing ℓ with the η instead of $\ell_{\rm m}$ yields similar results with regards to the collapse of the PDFs, which was observed in Fig. 3.5

3.2.2 Joint Statistics

Adding the second DE parameter to the statistical analyses helps to gain further insight. The joint probability density function (JPDF) of both DE parameters $P(\ell, \Delta \phi)$ is expected to suffice for a complete statistical description of a scalar field [127]. The JPDF of both normalized DE parameters is shown for selected cases in Fig. [7.7] The DE scalar difference was normalized in the same fashion as the DE length, $\Delta \phi^* = \Delta \phi/\Delta \phi_{\rm m}$, with the volume averaged scalar difference $\Delta \phi_{\rm m}$. Analogous to the marginal PDF in Fig. [3.5] regions in the JPDF can be attributed to different physical mechanisms. These regions

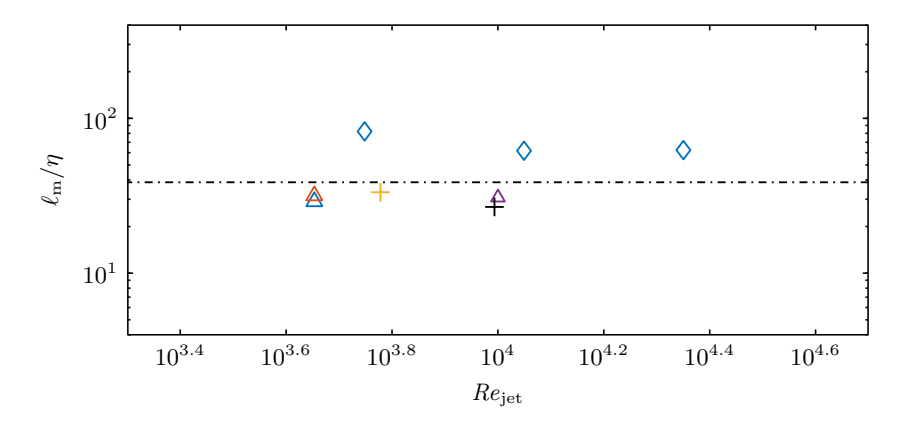


Figure 3.6: Ratio of the Kolmogorov micro scale η to the mean DE length ℓ_m for various inert and reacting cases. Diamonds: spatially evolving premixed jet flames, triangles: temporally evolving diffusion jet flames and crosses: inert temporally evolving jets. The dash dotted line indicates the average ratio obtained from isotropic turbulence. The line is placed arbitrarily as no jet Reynolds number is defined in homogeneous isotropic turbulence.

are marked in Fig. 7.7 a). The diffusive drift region is characterized by small ℓ and $\Delta\phi$. The random splitting and reconnection region is indicated for intermediate to large ℓ and $\Delta \phi$. Additionally, the probability density of cliff structures in the scalar fields, the common feature of turbulent scalars [65], can be observed for small ℓ and large $\Delta \phi$. While the scalar difference between the extremal points in Figs. (7.7a)-c) is solely governed by diffusive and convective transport, for the temperature field in Fig. 7.7a) a source term is present in the governing equations. While the normalized spatial distribution of the extremal points remains the same, c.f. Fig. 3.5, the scalar difference is significantly influenced by the source term. The presence of the strongly coherent and robust flame front results in a high probability of cliff structures in the JPDF. The motion of turbulent eddies will introduce extreme points in the temperature field in the vicinity of the flame front, creating smaller scalar differences. However, the inherent difference in the source terms in these newly created points will counteract this. The difference between the fairly universal JPDF of the passive scalar ϕ and the JPDF of a reactive scalar, in this example the temperature T, can be used to gauge the level of scale interaction between turbulence and the physical mechanism governing the source term.

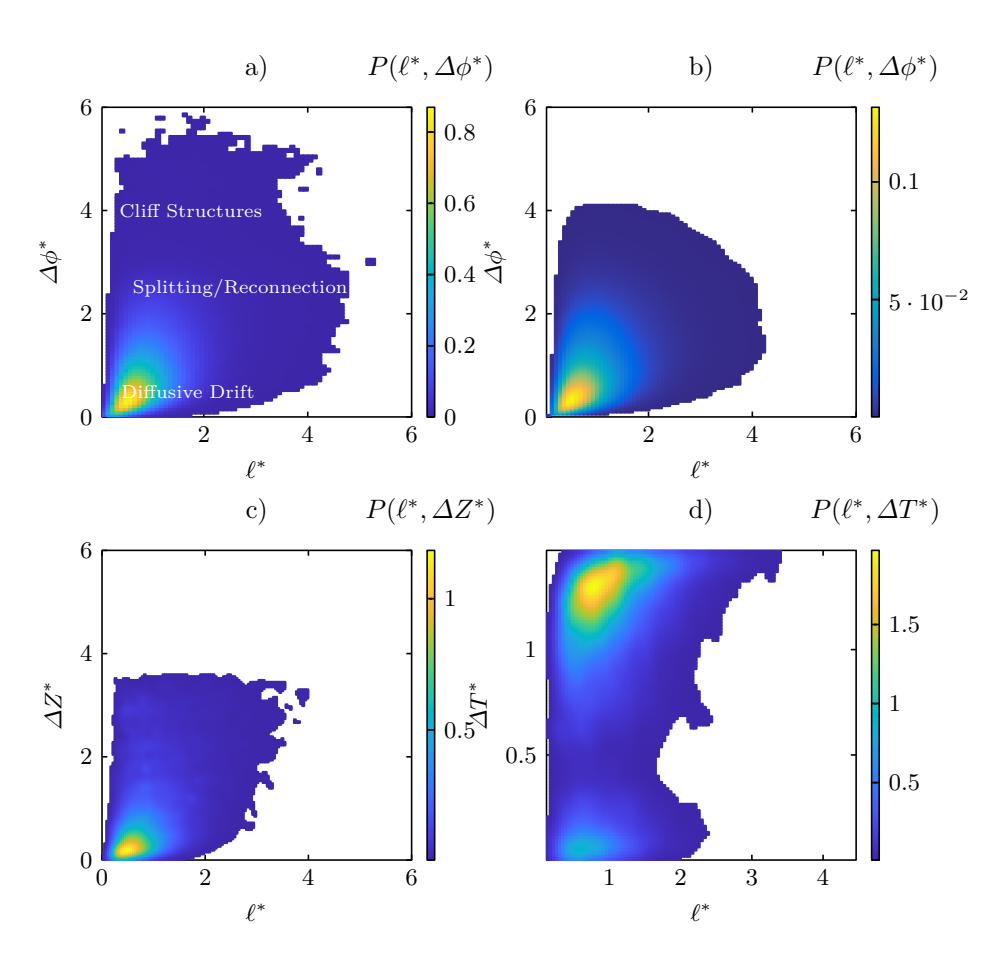


Figure 3.7: JPDFS of the normalized DE length and DE scalar difference for various fields in different flow configurations. a): passive scalar in an inert temporally evolving planar jet, b): passive scalar in an inert spatially evolving mixing layer, c): mixture fraction in a planar temporally evolving non-premixed jet flame and d): temperature in a planar spatially evolving premixed jet flame.

Besides providing turbulent scales, the DEs provide a multitude of ways to analyze turbulent flows or enhance existing methods of analysis. A few examples, which are not limited to inert flows, shall be given in the following section.

It is possible to relate DEs to a different and commonly used method of analysis. As remarked in Chapter 2 structure functions are a common tool to study the multi-scale nature of turbulence to overcome the challenge of non-locality in turbulent flows. Analogous to the structure functions of the velocity field eq. (2.11), structure functions of the scalar field of order n are defined as:

$$S_n(\vec{r}) = \langle (\phi(\vec{x} + \vec{r}) - \phi(\vec{x}))^n \rangle, \qquad (3.1)$$

with \vec{r} being the spatial separation between the two points and $\langle \dots \rangle$ indicating an appropriately defined statistical average. Besides the simple case of isotropic turbulence, choosing a physically meaningful \vec{r} can prove to be challenging in non-homogeneous or non-isotropic flows. A straightforward way of choosing \vec{r} is employing the gradient trajectories of the DEs. The difference of the quantity of interest can be conditioned on the arc length distance s of any point on the gradient trajectory starting in a respective material point as shown by $\boxed{55}$. Even more simplified, only the extremal point pairs of individual DEs can be used to obtain structure functions based on DEs:

$$S_n \sim \langle \Delta \phi^n | \ell \rangle$$
. (3.2)

The scalar difference to the *n*th power conditioned on the DE length $\langle \Delta \phi^n | \ell \rangle$ represents a structure function where the distance \vec{r} , in this case ℓ , is not arbitrarily chosen, but is determined by the two extremal points of each dissipation element. The statistical average will be done for dissipation elements with the same lengths, instead of using arbitrary points with same separating distances.

The results for the normalized first order scalar structure function in isotropic turbulence are shown in Fig. 3.8a). The theoretical scaling with this exponent of 1/3 is recovered in this way of obtaining the structure function 127. In isotropic turbulence, other theoretical scalings of the structure functions, such as the value of of the scaling exponent of 2/3 for the structure function of the turbulent kinetic energy $\langle (k(\vec{x}+\vec{r})-k(\vec{x}))\rangle \sim \langle \Delta k|\ell\rangle$, can be recovered as well 55. However, in free shear flows, the presence of mean shear has an influence on the scaling of the structure functions. This can be investigated accurately with the DE conditioned structure functions as well, as demonstrated for selected shear flow configurations in Fig. 3.8b).

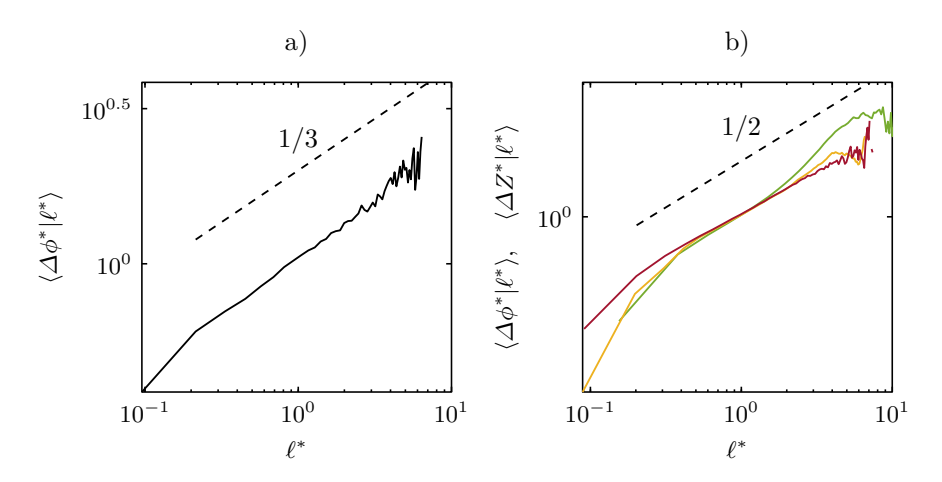


Figure 3.8: Mean DE scalar difference conditioned on the DE length for various flow configurations. —: isotropic turbulence, —: planar temporally evolving non-premixed jet flame, —: inert temporally evolving planar jet and —: inert spatially evolving mixing layer. The dashed black lines indicate in a): the theoretic scaling and in b): actual scaling observed in free shear flows.

Even though the cases are vastly different, the conditional structure functions display a seemingly universal scaling exponent of 1/2.

Obtaining structure functions in this way is, of course, not limited to the first order, but for the sake of brevity, additional orders are not shown here.

3.2.3 DE analysis of Reacting Flows

There are many different physical phenomena in turbulent flows which strongly interact with a certain range of turbulent scales. As the DE analysis provides turbulent scales, a local comparison with the characteristic scales of the additional physical phenomenon is straightforward. The investigation of scale interaction by means of DE analysis is illustrated here in the context of turbulent combustion. This subject lends itself to a DE analysis because in the asymptotic limits of no scale interaction or very limited interaction, turbulent combustion is fairly well understood and can be modeled appropriately, while the intense interaction of flame scales and turbulent scales is still the subject of research.

For premixed combustion, the idea of varying levels of scale interaction leads to the construction of the so-called "Borghi-Peters diagram" [95]. Turbulent

scales, such as the Kolmogorov length η are compared to different scales of the flame. Using the DE length ℓ obtained from the temperature field for the local estimation of the turbulent length scales to be compared to the flame thickness $l_{\rm F}$, consistent results with regards to the expected combustion regimes were obtained $\boxed{41}$.

However, for non-premixed flames this comparison is not as clear as the flame scales strongly vary in space and depend on the local gradient of the mixture fraction Z. The mixture fraction is the most meaningful scalar field in the context of non-premixed flames 95 and is therefore the prime candidate for the DE analysis.

A common configuration to investigate non-premixed laminar flames is the counterflow configuration [101]. An exemplary mixture fraction profile in a counterflow flame is shown in Fig. [3.9a). In the limit of fast, but not infinitely fast chemistry, the so called "flamelet regime," a corresponding heat release profile in mixture fraction space can be obtained from the steady-state flamelet solution. This heat release profile is shown in Fig. [3.9b). The decisive parameter linking the flow field and the chemical field in this regime is the scalar dissipation rate at stoichiometric conditions

$$\chi_{\rm st} = 2D \left(\nabla Z \right)_{\rm st}^2 \,. \tag{3.3}$$

Conveniently, the DE gradient $g = \Delta Z/\ell$ can be used analogously to the scalar dissipation rate. In the limit of small DEs, the following relation is true:

$$\lim_{\ell \to 0} g = |\nabla Z| \ . \tag{3.4}$$

From this follows the proportionality of the scalar dissipation rate χ and the DE gradient g,

$$\chi \sim Dq^2 \,. \tag{3.5}$$

The strong correlation between g and χ was first observed in isotropic turbulence $\boxed{127}$, but also in free shear flows $\boxed{53}$ and in reacting flows $\boxed{58}$.

Now let us assume that the mixture fraction field is affected by turbulence of different intensities leading to the introduction of extremal points in the mixture fraction profile in Fig. 3.9a). Consequently, DEs will form around the position of the stoichiometric mixture. Three exemplary conceivable DEs are plotted in Fig. 3.9a); a long DE, an intermediate DE and a short DE. Let all three DEs have the same mixture fraction gradient at stoichiometric conditions of a laminar flamelet profile so that the scalar dissipation rate $\chi_{\rm st}$ is the same. The introduced extremal points signify a forced interruption of the diffusive transport on which the flamelet structure relies. The points of

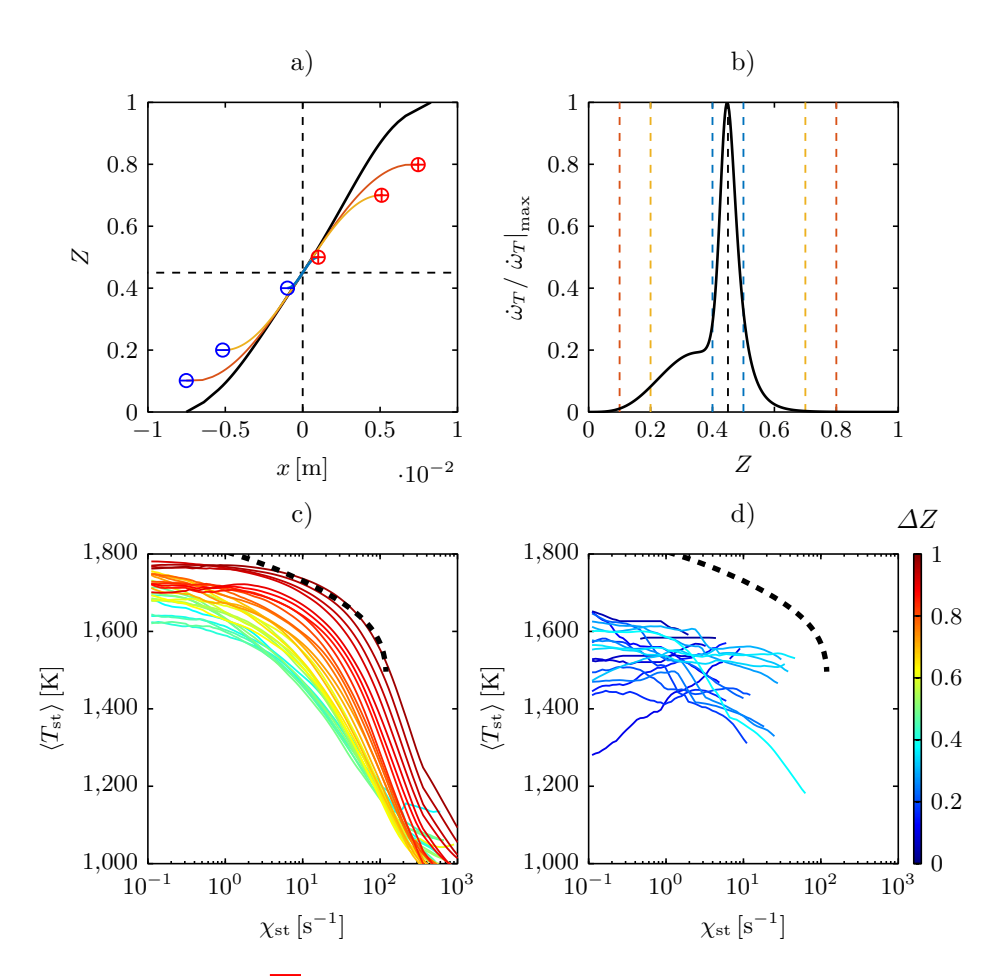


Figure 3.9: a): (—): Mixture fraction Z profile in physical space obtained from a counterflow configuration, the black dashed lines indicate the position and the value of the stoichiometric mixture fraction. (—): schematic long DE, (—): schematic intermediate and (—): schematic short DE. b): (—): Corresponding stationary flamelet solution of the normalized heat release $\dot{\omega}_T$ in mixture fraction space. The colored dashed lines indicate location of the extremal points in mixture fraction space of the respective schematic DEs. c) and d): mean stoichiometric temperature $\langle T_{\rm st} \rangle$ in a DNS of planar non-premixed jet flame conditioned on the stoichiometric scalar dissipation rate $\chi_{\rm st}$ (c): $\Delta Z \geq \Delta Z_{\rm r}$ and d): $\Delta Z \leq \Delta Z_{\rm r}$). The scalar difference ΔZ is indicated by the color of the lines, ranging from blue ($\Delta Z = 0.01$) over yellow to red ($\Delta Z = 1$). (••): stationary flamelet solution in the counterflow configuration.

interruption with regards to the heat release for three exemplary DEs are marked in Fig. 3.9b). The long DE interrupts the profile in points of negligible heat release and no effect on the flame structure is expected. However, it is already questionable if the traditional flamelet structure will form for the intermediate DE. In contrast, for the short DE, the formation of an intact flamelet structure can be ruled out. It is straightforward to see that comparing the DE scalar difference ΔZ to the range of Z values in the flamelet in which significant values of the heat release are present is a convenient way to judge wether a conventional flamelet structure is feasible. To this end, a reaction zone thickness $\delta Z_{\rm r}$ in Z-space needs to be defined. Even though the reaction zone thickness varies greatly depending on the fuel and oxidizer composition, $\delta Z_{\rm r}$ can to be easily approximated by fitting the heat release of the flamelet solution for the given composition with a gaussian:

$$\delta Z_{\rm r}' = 2 \left(-2 \ln(2) \dot{\omega}_{\rm max} \left. \frac{\partial^2 \dot{\omega}_T}{\partial Z^2} \right|_{Z = Z_{\dot{\omega}_{\rm max}}}^{-1} \right)^{0.5}, \tag{3.6}$$

with the maximum heat release in the stationary flamelet solution $\dot{\omega}_{\rm T,max}$ for a given $\chi_{\rm st}$ and $Z_{\dot{\omega}_{\rm max}}$ being the mixture fraction value for which the maximum heat release is observed. In essence, $\delta Z_{\rm r}'$ provides a meaningful, non-abitrary and easily obtainable flame scale for non-premixed combustion for different values of $\chi_{\rm st}$ to be compared to the turbulent scale provided by ΔZ .

This concept is applied to a DNS of a temporally evolving planar non-premixed jet flame. The temperature at stoichiometric conditions is conditioned on the scalar dissipation rate as well as the DE scalar difference ΔZ . This is shown in Fig. $3.9\mathrm{c}$) for large ΔZ . For DEs with $\Delta Z \approx 1$, the stationary flamelet solution is obtained. As the DE scalar difference is reduced, the temperature is lowered as well. The original flamelet profile is compressed along the χ_{st} -axis, but the expected clear correlation with the temperature is still observed. However, for small $\Delta Z < \delta Z_{\mathrm{r}}$, this correlation ceases as the inner flame structure is interrupted by extremal points. This is shown in Fig. $3.9\mathrm{d}$), where no discernible relation between χ_{st} and $\langle T_{\mathrm{st}} \rangle$ is observed.

This example shows how the DE scalar difference ΔZ can be used in the context of non-premixed flames to judge the scale interaction between the flame and turbulence. ΔZ symbolizes the maximum length in Z-space in which a diffusive transport dominated structure, like a flamelet, can exist.

4 Direct Numerical Simulations of Turbulent Reacting Flows

In this chapter, a brief introduction and overview of direct numerical simulations (DNS) is given, and the numerical methods employed in conducting the DNS cases discussed in this thesis are summarized. Important quantities and non-dimensional numbers which characterize the cases are showcased. The chapter is concluded with a brief flame analysis of the performed cases.

4.1 Introduction to Direct Numerical Simulations

As outlined in Chapter 2 the characteristics of turbulence lead to a lack of analytical solutions. Consequently, to validate theoretical predictions and models, the ground truth or 'reality' needs to be established. To acquire a reliable turbulent solution, there are two approaches. Traditionally, experiments were used with the advantage that no model assumptions are needed (not even the Navier-Stokes equations in which the viscous stress tensor constitutes a modelled term.) Nonetheless, the crucial benefit lies in the high values of the Reynolds number achievable in experiments. However, in addition to the difficulty of controlling the boundary conditions and the substantial uncertainties this causes in experiments, the signal to noise ratio in the recorded data lessens the quality and requires post-processing algorithms. More importantly, it is typically unfeasible to obtain three dimensional data fields of large fluid volumes with the desired temporal and spatial resolution. Due to the one-point or planar measurements possible with cameras and lasers, the recreation of three-dimensional data fields relies on Taylors' hypothesis. All these effects are exacerbated in reacting flows where the high density gradients and radiation of the reactants severely complicate the measurements or prevent the utilization of certain experimental techniques completely. Furthermore, quantities of paramount importance, such as most species mass fractions or the heat release, cannot be obtained in a three-dimensional fashion in turbulent reacting flows with state-of-the-art experimental methods.

These drawbacks do not apply to DNS where the full Navier-Stokes equations are solved numerically for all turbulent scales for a given problem. To accomplish this, the computational domain, on the one hand, needs to span

several integral scales $\ell_{\rm t}$ to capture important large scale flow characteristics. On the other hand, the grid has to be fine enough to resolve the viscous subrange adequately. For simple, first order statistics and likewise simple quantities, Pope 104 estimates a maximum grid spacing Δ of

$$\Delta \le 2.1\eta. \tag{4.1}$$

However, Boschung et al. [22] showed that the cut-off length scales in the viscous range are both dependent on the Reynolds number and the order of the statistics to be investigated. Depending on the configuration and the goal of investigation, the required grid resolution needs to be significantly finer than the originally proposed ratio.

The first numerical study of turbulence using DNS was performed by Orszag and Patterson [87]. These were DNS of forced isotropic turbulence in a periodic box employing pseudo-spectral methods. Unlike the DNS performed for this thesis, which utilize finite difference schemes, the Navier-Stokes equations were solved in wave number space using highly accurate spectral methods.

Due to breakthroughs and significant advances in computer engineering science, computational power has increased exponentially since this early groundwork of DNS. However, the most serious shortcoming of DNS remains the tremendous calculation costs associated with them. Even with the aide of state-of-the-art supercomputers and massively parallelized codes, the achievable Reynolds number is still very limited.

Accounting for the larger computational grids as a result of the increasing scales separation and the smaller time step sizes to satisfy the Courant-Friedrichs-Lewy condition, Pope $\boxed{104}$ estimated the computational costs C required for a statistical convergence of a turbulent flow as

$$C \sim Re_{\lambda}^6$$
 (4.2)

The predicted steep rise in computational costs with increasing Re_{λ} signifes the inherent difficulties of increasing the Reynolds number in DNS. Further, the most numerically 'cost effective' configuration of forced isotropic turbulence does not lend itself to the study of a variety of important phenomena interacting with the combustion chemistry encountered in reacting turbulent flows. Such phenomena include the shear generated turbulence and the inherent anisotropy associated with it, the presence of the turbulent/non-turbulent interface and external intermittency. As the idealized free-shear flow configurations used for studying the aforementioned phenomena possess only limited regions of turbulence production (unlike the forcing in the entire domain of the isotropic turbulence cases), high turbulence intensity and consequently

the Reynolds number are significantly lower for the same expenditure of calculation resources.

Finally, resolving not only the turbulent but also all chemical scales further increases the costs of DNS of reacting turbulent flows drastically. For the values of the Damköhler number and the resulting combustion conditions investigated in this thesis, this resulted in twice as fine grid spacing than what would be considered necessary to adequately resolve the viscous range of the turbulent scales. Due to the high density gradients encountered in the combustion of hydrocarbons, the Poisson equation is noticeably more costly to solve. The significant added cost of the DNS by the additional scalar transport of the species mass-fractions is proportional to the number of species required in the approximation of the combustion chemistry. Even more impactful to the overall cost are the chemical source terms which require the solution of a large, stiff system of equations on time scales well below that of the flow field. Besides the numerical aspects, the strong heat-release effects present in the combustion of hydrocarbons modify transport properties and further decrease the turbulent Reynolds number as a result of the increase of kinematic viscosity with temperature [63].

As a result, the computational costs for DNS utilizing finite rate chemistry with detailed chemical mechanisms for a simple fuel such as methane, is increased by two orders of magnitude compared to a non-reacting flow with a comparable turbulent Reynolds number.

Consequently, compromising with regards to limiting the potential insights, early investigations employing 3D-DNS of turbulent combustion forwent the use of a detailed description of chemistry in favor of irreversible one-step chemistry [88], [112], [100], [76] or used three-step of four-step global reactions to approximate the combustion chemistry [89], [14]. DNS of reacting flows employing detailed finite rate chemistry with meaningful values of the Reynolds number were performed only very recently [62], [119], [83].

Even using simplified chemical mechanisms, the Reynolds number required to simulate the combustion conditions in real life engineering applications will regrettably be unobtainable for decades to come. Therefore, concessions to the numerical setup need to be made, which usually result in smaller integral scales and a significantly smaller inertial subrange in DNS. As a consequence of the limited achievable Reynolds number in state-of-the-art DNS of reacting flows, certain statistics are contaminated by viscous effects. However, the described finite Reynolds number effects are not limited to DNS but are also present in experiments [1].

Despite the drawbacks of DNS, it has become an important tool in the

investigation of reacting and non-reacting flows, which will only become more prominent as calculation capacities increase. The access to all relevant instantaneous flow and scalar fields and the quantities derived thereof poses a prerequisite for the entire investigation presented in this thesis.

4.2 Numerical Methods and Algorithms

In the following, the specific numerical methods employed in the conduction of the DNS cases will be listed.

The computational code is an in-house code called CIAO, which was under the guidance of Prof. Pitsch at the Center for Turbulence Research at Stanford University. The simulations of the reacting flows conducted for the completion of this thesis, CIAO was used to solve the reacting Navier-Stokes equations in the low-Mach limit,

$$\frac{\partial \rho}{\partial t} + \frac{\partial \rho u_i}{\partial x_i} = 0, \qquad (4.3)$$

$$\frac{\partial \rho u_j}{\partial t} + \frac{\partial \rho u_i u_j}{\partial x_i} = -\frac{\partial \Pi}{\partial x_j} + \frac{\partial \tau_{ij,a}}{\partial x_i}, \qquad (4.4)$$

$$\frac{\partial \rho Y_{\alpha}}{\partial t} + \frac{\partial}{\partial x_{i}} \left(\rho \left(u_{i} + V_{i,\alpha} \right) Y_{\alpha} \right) = \dot{m}_{\alpha}, \tag{4.5}$$

$$c_{\mathbf{p}}\frac{\partial\rho T}{\partial t} + c_{\mathbf{p}}\frac{\partial u_{i}\rho T}{\partial x_{i}} = \frac{\partial}{\partial x_{i}}\left(\kappa\frac{\partial T}{\partial x_{i}}\right) + \rho\frac{\partial T}{\partial x_{i}}\sum_{\alpha=1}^{n}c_{\mathbf{p},\alpha}Y_{\alpha}V_{i,\alpha} + \sum_{\alpha=1}^{n}h_{\alpha}\dot{m}_{\alpha}.$$
(4.6)

In the governing equations, ρ denotes the density, u_{α} the velocity, Π the disturbance pressure, $\tau_{ij,a}$ the stress tensor, Y_{α} the mass fraction of species α , $V_{i,\alpha}$ the diffusion velocity of species α , \dot{m}_{α} the net mass production rate of species α due to chemical reactions, $c_{\rm p}$ the specific heat capacity of the mixture, T the temperature, κ the conductivity of the mixture, h_{α} the enthalpy of species i, and n the number of species. For the stress tensor $\tau_{\alpha\beta,a}$, the model for Newtonian fluids eq. (2.4) is used. The diffusion velocity follows the Curtiss-Hirschfelder approximation [64] with

$$V_{i,\alpha} = -\frac{1}{Y_{\alpha}} D_{\alpha} \frac{M_{\alpha}}{M} \frac{\partial X_{\alpha}}{\partial x_{i}} + V_{i}^{c} \quad \text{and} \quad V_{i}^{c} = \sum_{\alpha=1}^{n} D_{\alpha} \frac{M_{\alpha}}{M} \frac{\partial X_{\alpha}}{\partial x_{i}}, \tag{4.7}$$

where D_{α} denotes the diffusivity of species α , M_{α} the molecular mass of species α and M the molecular mass of the gas mixture. Radiative heat loss $\dot{q}_R = 0$ was neglected due to its very limited effect in the simulated combustion conditions.

The temperature and species equations, eqs. (4.5) and (4.6), are advanced by introducing a symmetric operator split of Strang 114. The two independent operators account for transport and reaction.

The chemistry operator is noted as \mathcal{F}^{C} and is described by the following set \mathcal{F}_{dt}^{C} of ordinary differential equations

$$\mathcal{F}_{dt}^{C}: \begin{cases} \frac{\partial \rho Y_{\alpha}}{\partial t} = \dot{\omega}_{\alpha} \\ c_{p} \frac{\partial \rho T}{\partial t} = \sum_{\alpha=1}^{n} h_{\alpha} \dot{\omega}_{\alpha}. \end{cases}$$
(4.8)

Similarly, the operator for transport $\mathcal{F}_{\mathrm{d}t}^{\mathrm{Trans}}$ is governed by

$$\mathcal{F}_{\mathrm{d}t}^{\mathrm{Trans}} : \begin{cases} \frac{\partial \rho Y_{\alpha}}{\partial t} + \frac{\partial}{\partial x_{i}} \left(\rho \left(u_{i} + V_{i,\alpha} \right) Y_{\alpha} \right) = 0 \\ c_{\mathrm{p}} \frac{\partial \rho T}{\partial t} + c_{\mathrm{p}} \frac{\partial u_{i} \rho T}{\partial x_{i}} = \frac{\partial}{\partial x_{i}} \left(\kappa \frac{\partial T}{\partial x_{i}} \right) + \rho \frac{\partial T}{\partial x_{i}} \sum_{\alpha=1}^{n} c_{\mathrm{p},\alpha} Y_{\alpha} V_{i,\alpha}. \end{cases}$$

$$(4.9)$$

Combining these two operators, the solution at a new time step $(Y_{\alpha}^{m+1}, T^{m+1})$ is computed as

$$\mathcal{F}_{\mathrm{d}t}\left(Y_{\alpha}^{m},T^{m}\right) = \mathcal{F}_{\mathrm{d}t/2}^{\mathrm{Trans}}\mathcal{F}_{\mathrm{d}t}^{\mathrm{C}}\mathcal{F}_{\mathrm{d}t/2}^{\mathrm{Trans}} \longrightarrow \left(Y_{\alpha}^{m+1},T^{m+1}\right),\tag{4.10}$$

where m denotes the m^{th} time step.

Combustion chemistry is modeled using a reduced mechanism for the oxidation of methane comprising 28 species and 102 reactions [99]. Additionally, the formation of NO is included by means of the Zeldovich mechanism [78].

Time integration is achieved using a Crank-Nicolson 36 time advancement scheme. Spatial and temporal staggering is used to increase the accuracy of stencils. The Poisson equation for the pressure is solved by the multi-grid HYPRE solver 47. Momentum equations are spatially discretized with a fourth order scheme. Species and temperature equations are discretized with a fifth order weighted ENO 68 scheme.

The chemistry operator uses a time-implicit backward difference method, as implemented in CVODE [27], which is a widespread software package for integrating stiff ODEs. For further details about the applied numerical

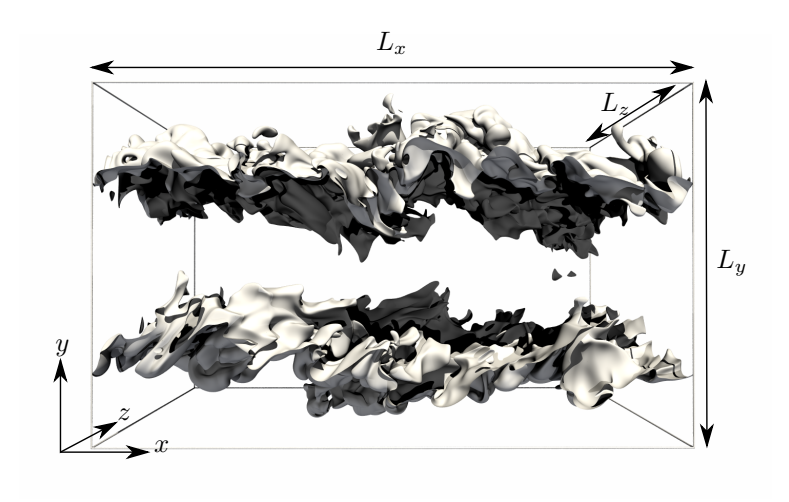


Figure 4.1: General setup of the non-premixed DNS investigated in this thesis. The grey iso surface indicates the position of the stoichiometric mixture fraction.

algorithms and code verification, the reader is referred to 43. The code uses the widely known message passing interface (MPI) standard. The parallelization strategy is to decompose the rectangular simulation domain into cubes and assign a processor to each of these cubes in order to minimize the cost of communication.

4.2.1 Numerical Methods of the Non-Reacting Cases

The DNS of the non-reactive cases are performed by solving the non-dimensional unsteady incompressible Navier-Stokes equations employing the in-house Solver psDNS [60]. Additionally, an advection-diffusion equation is solved for a passive scalar. Spatial derivatives are calculated by the implicit sixth-order finite difference compact scheme introduced by Lele [79]. The temporal integration is performed by employing a low storage fourth-order Runge-Kutta method. The Poisson equation is solved in spectral space by adapting a Helmholtz equation [34].

4.3 Configurations and Case Descriptions

The configuration selected for the DNS of the non-premixed cases for this thesis is the temporally evolving planar jet. Three different jet Reynolds numbers $Re_{\rm jet} = \overline{U}_0 H_0 / \nu_{\rm fuel}$, with initial mean jet bulk velocity \overline{U}_0 , initial jet width H_0 , and kinematic viscosity ν_{fuel} of the fuel, were realized. The values of the Reynolds numbers range from 4,500 to 10,000. Multiple Reynolds numbers are required to investigate the distinctive scaling of DE parameters, which was observed in non-reacting flows by Wang and Peters [127, 128, 126]. In addition to the change in Reynolds numbers, two different dilutions of the fuel stream were used for the lowest Reynolds number. These four cases will be referred to as the low Re low dilution case, the low Re high dilution case, the intermediate Re case and the high Re case. The turbulent Damköhler number $Da = \chi_0 H/U_{c,0}$ is set to Da = 0.125 for the low Re low dilution case and the low Re high dilution case and to Da = 0.15 for the other two high dilution cases. These values were chosen to induce local extinction and provide the basis for the investigation of extinction processes. At the final time step of the simulation, this resulted in approximately 5\%, 11\%, 16\% and 24% of extinguished flame surface for the Re low dilution case, for the Re high dilution case, for the intermediate Re case, and high Re case, respectively.

The oxidizer stream in all reacting cases is air, consisting of oxygen $Y_{O_2,1}=0.232$ and nitrogen $Y_{N_2,1}=0.768$. The fuel stream consists of highly diluted methane with $Y_{\text{CH}_4,2}=0.232$ for the low dilution case and $Y_{\text{CH}_4,2}=0.07$ for the high dilution cases. The indices 1 and 2 indicate the oxidizer and the fuel properties, respectively. The dilution of the fuel stream is achieved with N_2 . This results in a stoichiometric mixture fraction of $Z_{\text{st}}=0.2$ for the low Re low dilution case and $Z_{\text{st}}=0.45$ for the low Re high dilution case, the intermediate Re case and the high Re case. These high dilutions were chosen for two reasons; first, to provide sufficient distance between the turbulent/non-turbulent interface (TNTI) and the flame surface. Second, to provide a wide reaction zone thickness in mixture fraction space δZ_{r} . The temperature for both oxidizer and fuel was set to $T_1=T_2=500\,\text{K}$ for the low dilution case. To increase the resistance to the turbulence-induced strain, the temperature for the high dilution cases was raised to $T_1=T_2=680\,\text{K}$. The quenching dissipation rate for all cases is $\chi_{\text{q}}=120\,\text{s}^{-1}$.

The flow configuration of the reacting cases is shown schematically in Fig. 4.1 The domains are periodic in the stream-wise x-direction and spanwise z-direction. Boundary conditions in the crosswise y-direction were chosen as outlets 86.

The resolution was chosen to ensure a sufficiently resolved reaction zone with a minimum thickness of the OH-layer of 10 grid points at all times. This resolution was used in a number of DNS studies of non-premixed combustion for similar configurations [62] [11], where the quality of the results and the resolution requirements where assessed in detail. The minimum Kolmogorov scale is $\eta=209^-\mathrm{m}$, with $\eta=\nu^{3/4}\varepsilon^{-1/4}$, for the low Re low dilution case, $\eta=281^-\mathrm{m}$ for the low Re high dilution case, $\eta=245^-\mathrm{m}$ for the intermediate Re case, and $\eta=233^-\mathrm{m}$ for the high Re case. From this follows that $\Delta/\eta\approx0.76$, $\Delta/\eta\approx0.74$, $\Delta/\eta\approx0.85$, and $\Delta/\eta\approx0.86$, respectively. This high resolution is required for a meaningful result of a DE analysis [127]. Additional details regarding the numerical and physical parameters of the DNS are summarized in tab. [7.2]

The velocity field in the jet core was initialized with instantaneous realizations of turbulent channel flows. The mixture fraction field was initialized by integrating $\chi(Z) = a \exp(-2[\operatorname{erfc}^{-1}(2Z)]^2) = 2D(Z)(\partial Z/\partial y)^2$ in y-direction from Z=0 (oxidizer) to Z=1 (fuel). The mixture fraction profile starts at the edge of the channel velocity profile at $y=\pm 0.5H_0$ to provide a wider fuel slab to maintain combustion during later time steps and allow the velocity field to develop. The parameter a was chosen so that the dissipation rate at stoichiometric conditions $\chi_{\rm st}$ is set to $\chi_{\rm st}=40{\rm s}^{-1}$ for the low dilution case and $\chi_{\rm st}=10\,{\rm s}^{-1}$ for the high dilution cases. This difference in the initial scalar dissipation rate is chosen because of the significantly closer proximity of the position of the initial stoichiometric mixture to the velocity profile for the high dilution cases. The temperature and species mass fractions are mapped onto the mixture fraction field from a steady state flamelet solution with a non-unity Lewis number obtained in a counterflow configuration following Pitsch and Peters [101].

The initial profiles of the stream-wise velocity component and the mixture fraction are shown in Fig. 4.2 The normalized initial velocity profiles of the reacting cases differ slightly due to the different Reynolds numbers of the turbulent channel flows used in the initialisation.

In addition to the three reacting cases, a DNS of a non-reacting planar temporally evolving jet was conducted. This DNS will be referred to as non-reacting case I. The numerical setup, domain dimensions, and initial Reynolds number mirror the intermediate Re case. The initial velocity field is initialized using the same instantaneous velocity field of a turbulent channel flow employed in the initialization of the intermediate Re case. Material properties of the flow are homogeneous and obtained from the fuel composition of the reacting cases of $Y_{CH_4,2} = 0.07$ and $Y_{N_2,2} = 0.93$ at $T = 680 \, \text{K}$. A

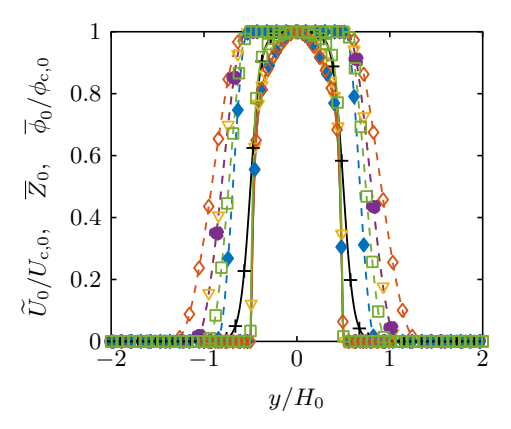


Figure 4.2: Starting profiles of the stream-wise mean velocity component \widetilde{U}_0 (solid lines) and starting profiles of the mixture fraction \overline{Z}_0 and passive scalar ϕ_0 (dashed lines). (\bullet): low Re low dilution case, (\bullet): low Re high dilution case, (\bullet): intermediate Re case, (\bullet): non-reacting case I and (\bullet): non-reacting case II

passive scalar ϕ was added, ranging from 0 to 1. The initial ϕ is that of the mixture fraction profile of the reactive case of the same Reynolds number. The Schmidt number of the passive scalar was set to $Sc_{\phi} = 0.77$. The ratio of the minimum Kolmogorov scale to the grid resolution is $\Delta/\eta \approx 1.1$.

Finally, a non-dimensional, non-reacting DNS, from this point on referred to as non-reacting case II, will serve as another dataset to include a more widely used jet configuration with traditional initial solution at a higher Reynolds number [113], [115], [66]. This configuration possesses periodic boundary conditions in both the stream-wise x- and the span-wise z-direction and free-slip conditions in the cross-stream direction y. The non-dimensional size of the domain is $L_x \times L_y \times L_z = 6\pi \times 12.5 \times 6\pi$. Nondimensionalization of the transport equations is performed with the initial velocity \overline{U}_0 , the initial jet thickness H_0 , and the maximum initial scalar value $\phi_{\rm max,0}$. The stream-wise velocity component and the passive scalar field are prescribed via a hyperbolic tangent profile. In the core region, the initial velocity is perturbed with a broadband random Gaussian velocity field derived from a one-dimensional turbulent energy spectrum to speed up the laminar-turbulent transition. The initial jet Reynolds number is set to $Re_{\rm jet} = \overline{U}_0 H_0/\nu = 9850$. The resolution in the core region is $\Delta/\eta \approx 1.4$.

	$\begin{array}{c} \text{Low } Re \\ \text{low dilution} \\ \text{case} \end{array}$	Low Re high dilution case	Intermediate Re case	High Re case	Non- reacting case I	Non- reacting case II
$\overline{U}_0 [\mathrm{m s}^{-1}]$	12.1	16.0	16.0	20.7	16.0	1.0
H_0 [mm]	15	18.7	25	32.3	25	1.0
$Re_{ m jet,0}$	4500	4500	6000	10000	6000	9850
Da	0.125	0.125	0.15	0.15	-	-
$Z_{ m st}$	0.2	0.45	0.45	0.45	-	-
L_x/H_0	8	8.2	8.5	8.5	8.5	6π
L_y/H_0	10	10.2	8.0	8.2	8.0	12.5
L_z/H_0	5.3	5.5	6.4	6.4	6.4	6π
N_x	768	768	1024	1280	1024	2560
N_y	1024	768	768	960	768	1312
N_z	512	512	768	960	768	2560
Δ/η	0.76	0.74	0.85	0.86	1.23	1.4
Total time [ms]	20	25	30	30	30	30
Symbol	+	→	₹	-	•	+

Table 4.1: Numerical and physical initial parameters of the DNS. Where needed, the parameters for the Non-Reacting case II were re-computed with the given values for \overline{U}_0 and H_0 .

4.4 Turbulent Flame Analysis

The overall flame evolution is shown for two different normalized time instants $t^* = 10$ and $t^* = 20$ in Figs. 4.3 4.4 The non-dimensional time t^* is defined as $t^* = (t - \Delta t_{\widetilde{\chi_{\rm st}''^2}=0})/t_{\rm j}$. The jet time is defined as $t_{\rm j} = H_0/\overline{U}_0$. In addition, the duration for which the variance of the scalar dissipation rate at stoichiometric conditions is zero $\Delta t_{\widetilde{\chi_{\rm st}''^2}=0}$ is introduced. The subtraction with $\Delta t_{\widetilde{\chi_{\rm st}''^2}=0}$ accounts for the varying time among the cases before the turbulent central flow reaches the surface of the stoichiometric mixture fraction due to the different initial fuel slab sizes. The two time steps correspond to the time of the maximum variance of the scalar dissipation rate at stoichiometric conditions, $t^* = 10$, and the final time step in the simulations $t^* = 20$.

The mixture fraction Z is shown in Fig. 4.3. The increase in wrinkling and folding of the flames due to turbulent advection, while present in the low dilution case, is more pronounced in the high dilution cases. To indicate local extinction, regions where the scalar dissipation rate exceeds the quenching dissipation rate of the stationary flamelet solution $\chi \geq \chi_{\rm q}$ are encompassed by a black contour. The regions of high χ are predominantly present in the rich regions of flow close to $Z_{\rm st}$. To indicate the burning flame regions and extinguished regions of the flame, a threshold of the OH mass fraction obtained from the steady state flamelet solution $Y_{\rm OH}(x_i) = 0.01 Y_{\rm OH}(Z_{\rm st}, \chi_{\rm q})$ is plotted

as a white iso-line. While all the cases display mostly intact flames, the later times show extinguished regions at low scalar dissipation rates indicating that these were extinguished earlier and are in the process of re-ignition. The slices of the temperature field for the same time steps of $t^* = 10$ (top) and $t^* = 20$ (bottom) are shown in Fig. 4.4 Extinct regions of flames are also evident in the temperature field.

The temporal evolution of the normalized mean $\widetilde{\chi_{\rm st}}$ at stoichiometric conditions is shown in Fig. 4.5a). Qualitatively, the temporal evolutions display the same features for all cases. The shape of the temporal evolution of $\widetilde{\chi_{\rm st}}$ is characteristic to the configuration of the planar temporally evolving jet and is observed also in other reacting and non-reacting jets 9, 66. The steep increase of $\widetilde{\chi_{\rm st}}$ is a result of increasing gradients caused by the formation of turbulence. The scalar dissipation rate experiences a peak and then enters an equilibrium state with the other turbulent fields, indicated by the exponential decay. Here, gradients decrease again as a result of the increasing length scales of the system.

The temporal development of the total surface area of the stoichiometric iso surface $A_{\rm st}$ is shown in Fig. 4.5b). $A_{\rm st}$ is normalized with the initial stoichimetric iso surface area $A_{\rm st,0} = 2L_xL_z$. The significantly bigger difference in stoichiometric iso surface growth between the low dilution case and high dilution cases is indicative of a higher influence of the stoichiometry than the Reynolds number in these simulations. The low Damköhler number causes local extinction, as already observed in Figs. 4.3 and 4.4. The burning part of the flame surface area $A_{\rm st,burning}$ is calculated from regions with at least 10% of the mass fraction of OH of the stationary flamelet solution at χ just below quenching conditions. The influence of localised extinction manifests itself in the departure of $A_{\rm st,burning}$ from $A_{\rm st}$ after $t^* \approx 3$, which results in a final ratio of the burning area to the extinct area of the stoichiometric iso surface of 0.95, 0.87, 0.80, and 0.75 for the low dilution low Re case, the high dilution low Re, intermediate Re case, and high Re case, respectively. The overall level of extinction is in good agreement with the magnitude of $\chi_{\rm st}$ in Fig. 4.4a). The trends observed in the temporal evolution of $\widetilde{\chi}_{\rm st}$ and $A_{\rm st}$ are qualitatively consistent with the observations of the extinction behavior of turbulent non-premixed flames of Lignell, Chen, and Schmutz 80.

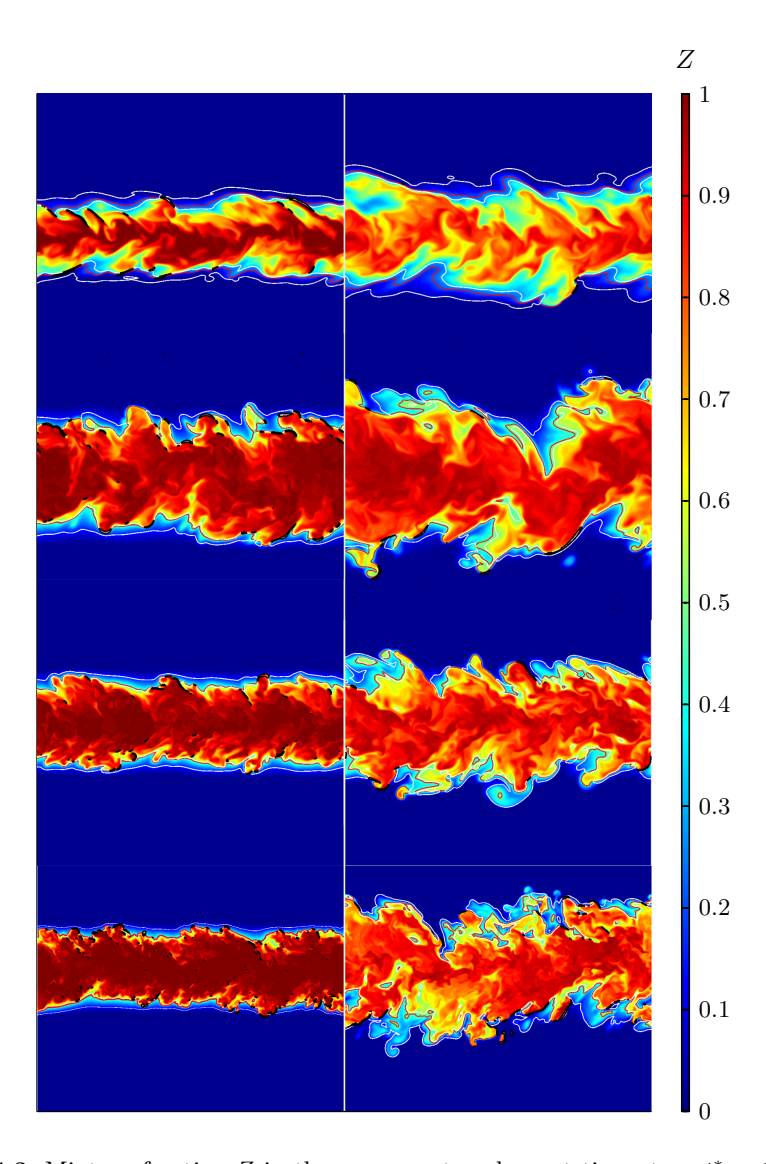


Figure 4.3: Mixture fraction Z in the x-y center plane at time steps $t^*=10$ (left) and $t^*=20$ (right). Top to bottom: low Re low dilution case, low Re high dilution case, intermediate Re case, and high Re case. The red color indicates the fuel stream, blue the oxidizer. The iso contour of the stoichiometric mixture fraction is indicated by a red line. The presence of OH is indicated by the iso contour of $Y_{\rm OH}=0.01Y_{\rm OH,flamelet}(Z_{\rm st})$ by the white lines. The regions of quenching dissipation rates $\chi \geq \chi_{\rm q}$ are indicated by black contours.

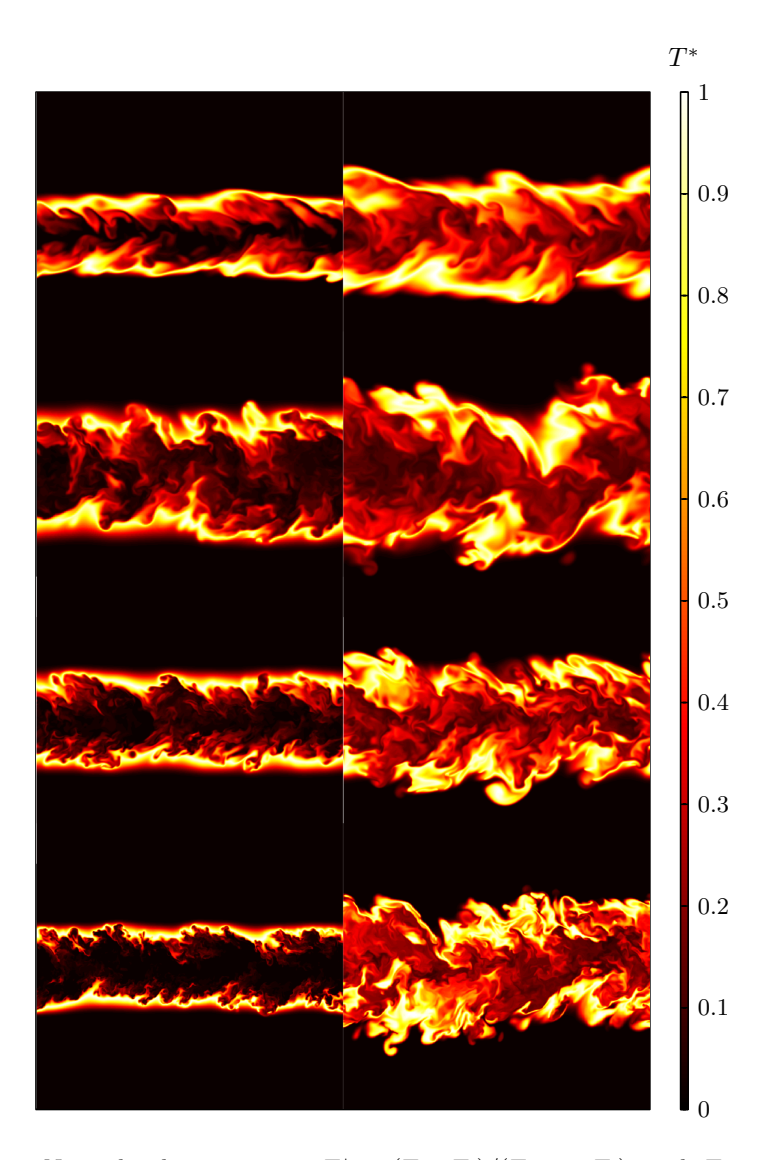


Figure 4.4: Normalized temperature $T^* = (T - T_1)/(T_{\text{max}} - T_1)$, with $T_{\text{max}} = 2100\,\text{K}$ for the low dilution case and $T_{\text{max}} = 1850\,\text{K}$ for the high dilution cases, in the x-y center plane at time steps $t^* = 10$ (left) and $t^* = 20$ (right). Top to bottom: low Re low dilution case, low Re high dilution case, intermediate Re case, and high Re case.

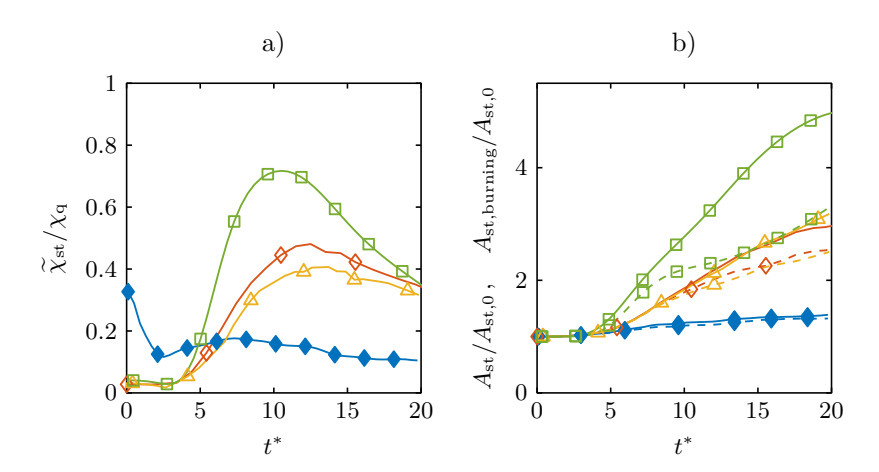


Figure 4.5: (a): Temporal evolution of the normalized Favre averaged scalar dissipation rate conditioned on the stoichiometric mixture fraction. (b): temporal evolution of the normalized area of the iso surface of the stoichiometric mixture fraction (solid) and burning area (dashed). (): low Re low dilution case, (): low Re high dilution case, (): intermediate Re case and (): high Re case. Normalization is achieved with the initial stoichiometric iso surface $A_{\rm st,0} = 2L_xL_z$. Burning regions of the stoichiometric iso surface are identified by thresholding the local OH mass fraction $Y_{\rm OH,burning} = Y_{\rm OH}(Z=Z_{\rm st}) \geq 0.1Y_{\rm OH,flamelet}(Z_{\rm st},\chi_{\rm q})$.

5 Dissipation Element Based Flame Analysis of Non-Premixed Flames

There are several regimes of interest in turbulent combustion. One that is very frequently encountered is the flamelet regime, where chemistry is relatively fast and reactions take place in thin layers. Many technical applications fall into this regime; therefore, prediction methods based on the flamelet concept are often used to model combustion in engines and gas turbines. In this framework, a turbulent flame is viewed as an ensemble of thin flamelet structures. The flamelet structure is laminar in nature and attached to an instantaneous flame surface, which is corrugated by turbulence. The concept applies to premixed as well as non-premixed combustion. In the case of non-premixed combustion, the assumption of infinitely fast reactions leads to the flame sheet model having an infinitely thin flame structure. As the turbulent mixing is the sole rate-determining process in this regime, the description of non-premixed combustion can be fully described by the transport of the mixture fraction

$$Z = \frac{m_1}{m_1 + m_2} \tag{5.1}$$

with m_1 and m_2 denoting the local mass originating of the fuel and the oxidizer, respectively. The departure from this limit requires the consideration of finite rate chemistry and can be described by the laminar diffusion flamelet concept [92]. Flamelet equations can be derived by transforming the transport equations for temperature and species mass fractions into equations with the mixture fraction Z as the independent variable, yielding equations for the species fractions and temperature as

$$\rho \frac{\partial Y_{\alpha}}{\partial t} - \rho \frac{\chi}{2} \frac{\partial^{2} Y_{\alpha}}{\partial Z^{2}} = \dot{\omega}_{\alpha}, \qquad \alpha = 1, 2, \dots, k.$$
 (5.2)

$$\rho \frac{\partial T}{\partial t} - \rho \frac{\chi}{2} \frac{\partial^2 T}{\partial Z^2} = \dot{\omega}_T, \qquad (5.3)$$

where χ is the scalar dissipation rate

$$\chi = 2D \left(\frac{\partial Z}{\partial x_i} \right)^2 \,. \tag{5.4}$$

In the equation for the chemical species, ρ is the density, Y_{α} is the mass fraction of species α , t is the time, Z is the mixture fraction, and ω_{α} is the chemical source term for species α . In the temperature equation, T is the temperature, ω_T is the heat release term due to chemical reactions, and D is the diffusion coefficient of the mixture fraction. Since transport in the outer, chemically inert structure of the flame is mostly governed by turbulence, which leads to similar transport for all scalars $[\mathfrak{P}]$, all Lewis numbers are assumed be unity $Le_{\alpha} = \lambda/(c_{\mathbf{p}}\rho D_{\alpha}) = 1$, with the thermal conductivity λ , the heat capacity $c_{\mathbf{p}}$, and the diffusion coefficient of the species D_{α} . Additional terms containing spatial derivatives orthogonal to Z, can be neglected to the leading order. The scalar dissipation rate χ serves as the quantity which connects the reacting scalar field to the turbulent flow field.

For intense turbulence, when turbulent scales are small compared to the scales of the flame, the implied separation of turbulent and chemical scales in the laminar diffusion flamelet concept is expected to fail $\boxed{16}$ $\boxed{103}$. The flame structure and the rate of mixing then start to be affected by interactions between reaction, diffusion, and turbulent straining. Another shortcoming is that even in the case of thin structures for the combustion reactions not all reactions are sufficiently fast. This is the case for the chemical processes governing pollutants like NO_x and soot, because their chemistry may be comparably slow. Furthermore, close to extinction or during ignition, when combustion becomes slow or when chemistry competes with diffusive losses in more than one direction, which is known as the edge flame effect $\boxed{48}$, the flamelet assumption of a thin one-dimensional layer will cease to be valid.

To identify and analyse spatial regions of the turbulent reacting flow, which either correspond to flamelet-"friendly" conditions or are dominated by small-scale turbulence and extinction-inducing turbulence intensities, a systematic method for compartmentalization of the turbulent fields is required. A method for a physically motivated decomposition of turbulent scalar fields is the dissipation element (DE) analysis.

The DE analysis is applied here to the series of reacting DNS of non-premixed combustion outlined in the previous Chapter [4.3] In addition, selected non-reactive cases are also considered for comparison. In particular, statistics of the DE parameters are compared among the reacting and non-reacting cases to evaluate the effect of heat release on the scalar fields. The correlation of DE parameters and reacting scalars is investigated to demonstrate the importance of considering non-local effects in the investigated combustion conditions. A comparison of the flame scales with the local turbulent scales provided by the DEs is used to define a new regime

diagram for turbulent non-premixed combustion based on the DE parameters. Contrary to conventional approaches to regime classifications which employ global statistical quantities, the regimes are based on the instantaneous scalar topology and therefore allow for the coexistence and assessment of multiple regimes in a single flame. Finally, the regime diagram is used in a local classification of the combustion of the individual cases.

5.1 Dissipation Element Analysis

In the context of non-premixed flames, the mixture fraction Z is the scalar field of choice for a DE analysis, as it provides the most practical and meaningful scales for the investigation of turbulence/chemistry interaction. An exemplary interaction between a DE and the stoichiometric iso surface, which is wrinkled by the turbulent velocity field, in the low Re low dilution case is shown in Fig. 5.1. This helps to illustrate the non-trivial shape of DEs in three-dimensional space and, consequently, the complicated local structure of non-premixed combustion in the highly turbulent cases.

An entire field of DEs extracted from the intermediate Re case is shown in the top part of Fig. 5.2. The background field in this figure is that of the mixture fraction Z in the x-z center-plane of the turbulent jet, which is shown mirrored on the bottom part of the figure. The figure shows that dissipation elements are space-filling objects which subdivide the entire turbulent scalar field into smaller sub-units. As we follow the flame front indicated by the iso-line of the stoichiometric mixture fraction, we observe that DEs of various sizes and shapes are intersected by the flame. In addition, it can be seen that the size of the DEs increases as the core region of the jet is departed and the flame front is approached. This observed increase in size has two reasons. Firstly, the increased diffusivity caused by the heat release as well as a mean relative velocity in the cross-stream direction cause the DE to increase in size. Secondly, the intersection area depicted here depends on the DE orientation with regard to the shown cut plane. DEs tend to be elongated tube-like structures, as seen in fig. 5.1. Therefore, DEs oriented parallel to the x-y plane will appear significantly larger than DEs aligned with the span-wise direction. In the core of the jet, there is little to no preferential orientation of the DEs as the mixture fraction field is close to an isotropic state. However, crossing the reacting regions there are two reasons for a preferential orientation of the DEs. Due to the initialisation and configuration of the cases with Z=1 in the core and Z=0 in the outer cross-stream position, it is more probable that the maxima are located closer to the core than the

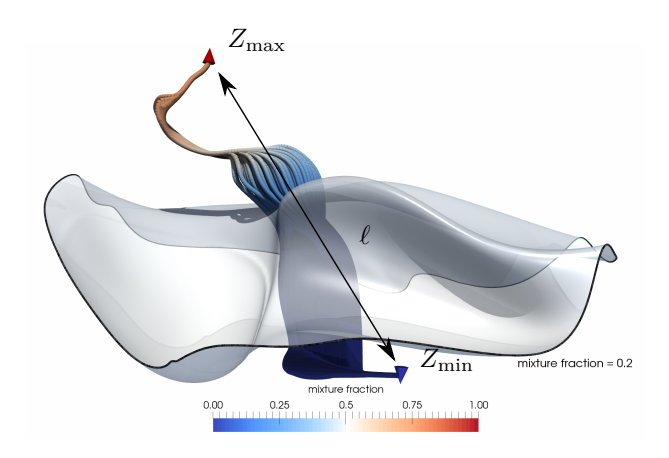


Figure 5.1: A DE in interaction with the flame front in the low Re low dilution case. The blue and red cone indicate the maximum and minimum, respectively. The DE is represented by the gradient trajectories used in its detection. Local values of the mixture fraction are indicated by the color of the gradient trajectories. The grey contour is the iso surface of the stoichiometric mixture fraction $Z_{\rm st} = 0.2$.

minima, which results in a natural alignment with the cross-stream direction. Additionally, the density differences cause a positive relative velocity between the extremal points spanning $Z_{\rm st}$. On average, this relative velocity is the cross-stream component which further induces an orientation on the DEs in that direction.

In order to estimate the influence of small scale turbulence in combustion, the local reaction layer thickness is typically compared to a turbulent length-scale like the Kolmogorov scale η . However, in non-premixed combustion, a comparison of the reaction layer thickness with turbulent length scales in physical space does not make much sense, because the width of the layer changes locally with the mixture fraction gradient. Since the transformation in mixture fraction space makes the flame structure more general, a meaningful comparison of scales, between the scalar difference ΔZ , provided locally by the individual DEs, with the reaction layer thickness $\delta Z_{\rm r}$ is proposed. In this context, the DE parameter ΔZ can be interpreted as the length in Z-space in which a flamelet-like solution can exist before terminating at its respective extremal points due to the influence of turbulence. Since the gradient trajectories used to identify individual DEs are identical to the physical coordinates of flamelets, DEs can also be viewed as groupings of

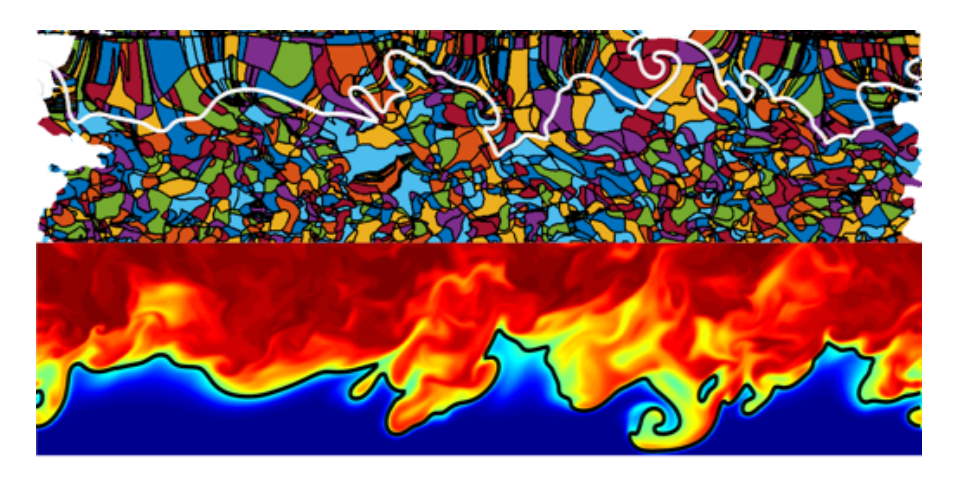


Figure 5.2: Top part: DE analysis of the mixture fraction field of the intermediate Re case. Individual DEs are encompassed in a black contour. Bottom part: mirrored mixture fraction Z field on which the DE analysis was performed. Blue color indicates the oxidizer with Z=0 and blue the fuel Z=1.

flamelet solutions. As the flame thickness in non-premixed flames varies greatly with the mixture fraction gradient, a second parameter to characterize DEs is instrumental in the analysis. Characterizing the scalar gradient, the parameter $g = \Delta Z/\ell$ will be used. Its square is expected to be related to the scalar dissipation rate χ as $\chi \sim Dg^2$, as was observed in isotropic turbulence by Wang and Peters [128].

5.1.1 Marginal Dissipation Element Parameter Statistics

One of the characteristic properties of DE parameters in non-reacting flows is the invariance of the PDFs of the DE length ℓ towards changes in Reynolds numbers and underlying scalar [128] [53]. When normalized by the mean DE separation length $\ell_{\rm m}$, the PDFs of $\ell^* = \ell/\ell_{\rm m}$ show a characteristic shape and almost perfect agreement for the entire range of investigated Reynolds numbers. Fig. [5.3] shows the PDFs of the normalized DE parameters for the four reacting cases and the two non-reacting jets. The PDFs were obtained from the final time-steps in the respective simulations and weighted with the individual DE volumes. DEs whose minima are situated outside the turbulent/non-turbulent interface (TNTI), as obtained by the method of

Bisset, Hunt, and Rogers. $\boxed{17}$, were omitted from the statistics to rule out the inclusion of false extremal points in the laminar regions of the flows. In this fashion, 69.5%, 85.5%, 87.7%, and 92.1% of the iso-surface of the stoichiometric mixture fraction is retained in the following statistics for the low Re low dilution case, low Re high dilution case, intermediate Re case, and high Re case, respectively. The decreasing number of excluded DE with increasing Reynolds number is a strong indicator of the additional applicability of the method to flames with higher turbulence intensities.

In Figs. 5.3a) and b), the normalized DE length for all investigated cases is shown. The characteristic shape of the PDFs observed in the non-reactive cases is retained in the reacting simulations [125, 55]. After an initial steep linear increase for the shortest elements, a maximum of the PDFs is reached at approximately 1.6 ℓ^* . This linear increase was attributed to the diffusive drift of extremal points by Wang & Peters. After the maximum, a exponential decrease of the PDF for the longer elements follows, which stems from the random cutting and reconnection process of turbulent eddies [127]. A perfect agreement is observed among all cases for the short elements. The wider separation of scales due to increasing Reynolds numbers is apparent in the tails of the PDFs which reach larger values for increasing Reynolds numbers. In Fig. 5.3c), the PDF of the normalized DE length is conditioned on DEs which cross the iso-surface of the stoichiometric mixture fraction. Again, the PDFs display the characteristic course observed in the PDFs of the entire flow field. The mean DE length $\ell_{\rm m}$ is only slightly larger (about 15 %) compared to the one obtained for all DEs within the TNTI. These observations are a strong indication that the geometry of the flow and its reactive nature do not fundamentally change the characteristic length scale of turbulent structures identified by the DEs.

In Fig. 5.3 d), the ratio of the mean DE length and the Kolmogorov micro scale is shown for all DEs within the TNTI. The scaling of $\ell_{\rm m}$ with η , which was already observed for other flow configurations, is also present in the reactive flows. $\ell_{\rm m}/\eta$ is approximately constant for the wide range of Reynolds numbers and configurations investigated in this work and close to the ratio observed in the isotropic configurations. In particular, the average DEs length is approximately 25-35 Kolmogorov scales. The difference in ratio with regards to the isotropic turbulence might be attributed to the presence of shear in the jet configuration.

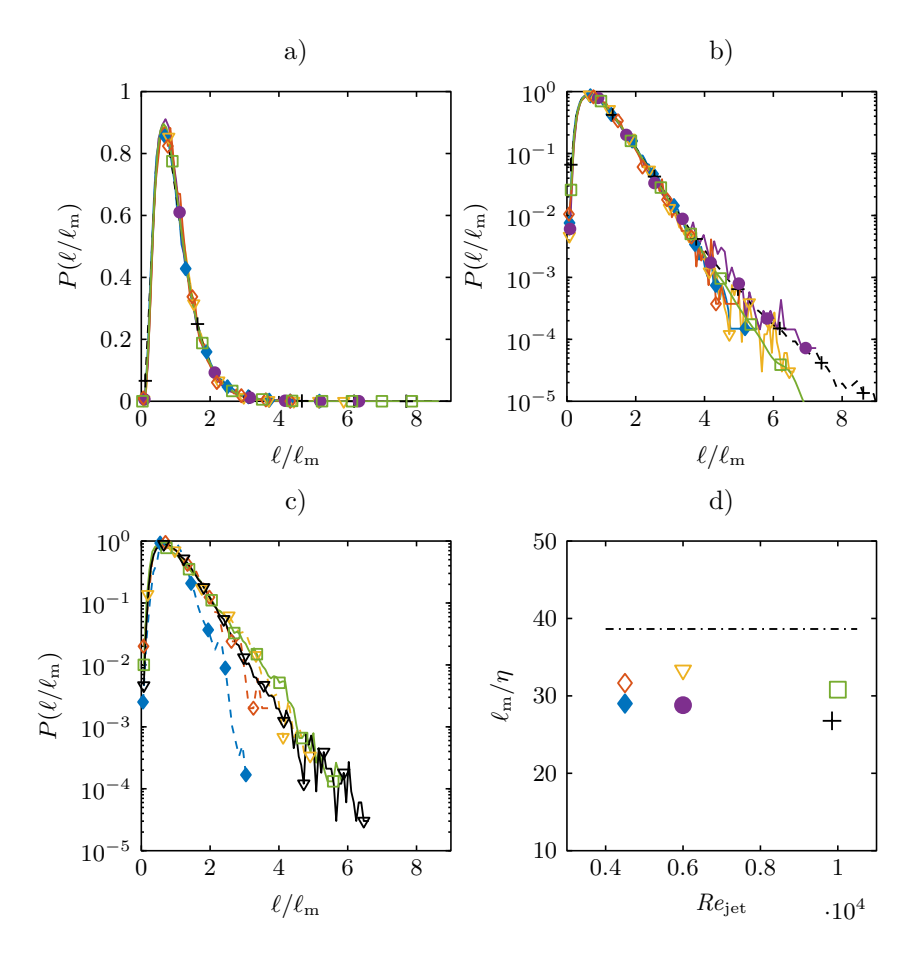


Figure 5.3: Comparison of PDFs of the normalized DE length ℓ/ℓ_m a): plotted in a linear scale and b): logarithmic scale . c): PDF of the normalized DE length conditioned on DEs crossing the stoichiometric iso surface (with the black line obtained from b), as a reference). d): ratio of the Kolmogorov micro scale η to the mean DE length ℓ_m for the investigated cases. \bullet : low Re low dilution case, \bullet : low Re high dilution case, \bullet : intermediate Re case, \bullet : high Re case, \bullet : non-reacting case I and \bullet : non-reacting case II. The dash dotted line indicates the average ratio obtained from isotropic turbulence in Wang and Peters [127]. The line is placed arbitrarily as no jet Reynolds numbers exist.

5.1.2 Joint Dissipation Element Parameter Statistics

Fig. 7.7 shows the joint probability density functions (JPDF) of the normalized DE length ℓ^* and the normalized scalar difference $\Delta Z^* = \Delta Z/\Delta Z_{\rm m}$, with the volume averaged scalar difference $\Delta Z_{\rm m}$, of the three jet cases in the final time step of the simulations. For the non-reacting cases in Figs. 7.7a) and b), one observes a global maximum of the probability density in the lower left corner for short elements and small scalar differences. This region of the JPDF is dominated by the diffusive drift of the extremal points leading to an annihilation of small DEs. On the top left hand side, for small ℓ and big ΔZ , the probability of cliff structures, ubiquitously present in scalar turbulence, can be observed [2], [65]. These structures are linked to external and internal intermittency and manifest themselves in very steep gradients of the scalar followed by a very gradual decent. Likewise, the scalar dissipation rate χ displays extreme spatial fluctuations. The lower right part of the JPDF, for long elements and small scalar differences, shows the regime of the physical mechanism of splitting and reconnection of DEs [127]. Qualitatively, the JPDFs of the two non-reactive cases agree while a noticeably larger separation of scales in the non-reacting case II is present, which is apparent from the different ranges of the axes.

The JPDFs of the reacting cases at low Reynolds number are shown in Figs. [7.7] c) and d). Clear qualitative differences are observable compared to the non-reacting case. While the diffusive drift region of the lower part of the JPDF, for values of $\Delta Z^* < 0.8$ resembles its counterpart of the non-reacting flows, the top part looks vastly different. In addition to the local maximum probability in the diffusive drift region, the global maximum for intermediate ℓ and large ΔZ is observed for the low Re low dilution case. This indicates the high probability of DEs which span large mixture fraction differences almost all the way from the fuel to the oxidizer side. While the DE length distributions are unaffected by the chemical reactions, the statistics of ΔZ are heavily influenced by chemical reactions and a distinct influence of the flame structure on the DE statistics can be observed. For the JPDF of the low Re high dilution case, the global maximum shifts again into the diffusive drift region while the cliff structures imprinted by the flame remain more pronounced than in the non-reacting cases. These cliff structures become even less pronounced as the Reynolds number is increased in the intermediate Recase in Fig. 7.7e), where the second local maximum for large ΔZ^* disappears. Finally, the JPDF of the high Re case Fig. (7.7f) completely resembles the JPDFs obtained from the non-reacting cases.

The (local) maximum probability density in Figs. 7.7 c) and d) stems

from insufficient turbulent mixing of the mixture fraction fields in these two cases. In the very beginning of the simulations, the mixture fraction fields have no turbulent fluctuations, and because of the lack of extremal points, all DEs would be infinitely long with $\ell \to \infty$. Simultaneously, all gradient trajectories would reach from Z=0 to Z=1. Then, the DE difference would be uniformly $\Delta Z = \Delta Z_{\rm m} = 1$. As turbulent mixing is applied to the mixture fraction fields, the turbulent eddies induce extremal points which reduce both ℓ and ΔZ as time progresses. Diffusive drift will remove extremal points once elements are small enough. Therefore, the high probability of large ΔZ (in other words, close to its initial value) is a result of either not enough time for the statistics ΔZ to have fully converged at the end of the simulations, or the lack of sufficient turbulence to reach the asymptotic state observed in the non-reacting cases or in the High Re case. The explanation for this is twofold. The locally high diffusivity in the reacting regions smoothes the scalar field and removes more extremal points in these regions. In addition, the locally low effective Reynolds number causes lower eddy turnover times. Therefore, fewer extremal points are introduced in the reacting regions.

The difference in the JPDFs between the low Reynolds number reacting and non-reacting cases could therefore be attributed to low Reynolds number effects in the reacting cases, which is amplified by heat release. Similar results with regards to trends of the effects of heat release on small scale statistics of the velocity and mixture fraction in non-premixed flames were reported in Attili and Bisetti 6. Additionally, this is consistent with the findings of Gauding et al. [58], where a similar effect on the joint DE statistics conditioned on the flame front was observed. Likewise, the differences were linked to poor mixing in the reactive regions of the flow. This is another strong indicator that not only the marginal DE length statistics $P(\ell)$, but also the DE scalar difference statistics of passive scalars in turbulent flows share a universal form if the Reynolds number is sufficiently high, regardless of the presence of combustion and heat release. Therefore, the differences between the JPDF of the DE parameters of a passive scalar field obtained from the reacting configurations and the universal form of the JPDF might be used to judge the extent of low Reynolds number effects.

For a more quantitive way to compare the DE statistics and to relate DE parameter statistics to a more commonly used method of analysis of turbulence, the mean of the normalized DE scalar difference is conditioned on the normalized DE length $\langle \Delta Z^* | \ell^* \rangle$ and $\langle \Delta \phi^* | \ell^* \rangle$, with $\langle \rangle$ indicating the average of all grid points within the TNTI. The *n*th conditional moment $\langle \Delta \phi^n | \ell^* \rangle$ can be interpreted as an analogue of the conventional structure

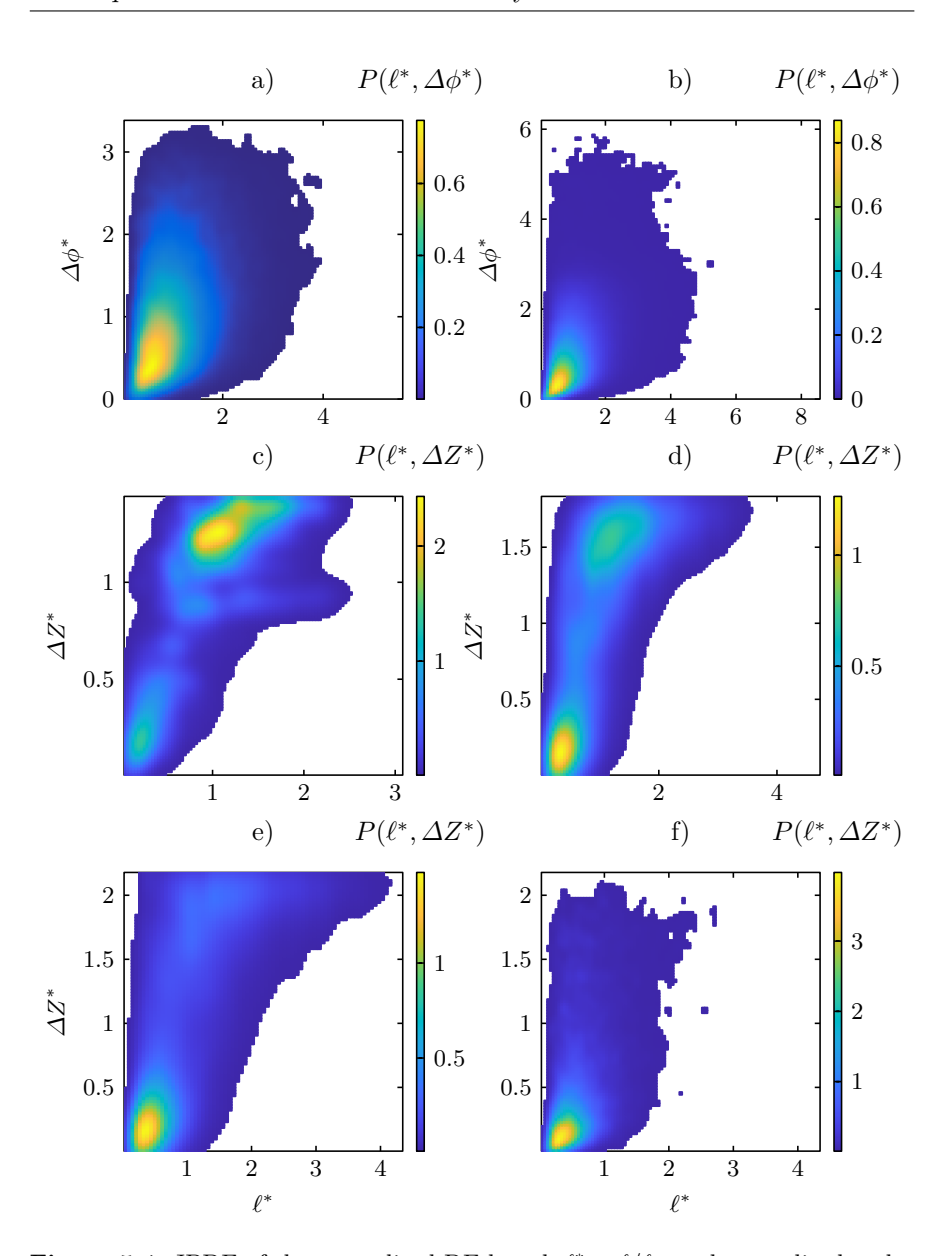


Figure 5.4: JPDF of the normalized DE length $\ell^* = \ell/\ell_m$ and normalized scalar difference $\Delta Z^* = \Delta Z/\Delta Z_m$ in the final time step of the respective cases. a): non-reacting case I, b): non-reacting case II, c): low Re low dilution case, d): low Re high dilution case and e): intermediate Re case and f): JPDF of the high Re case.

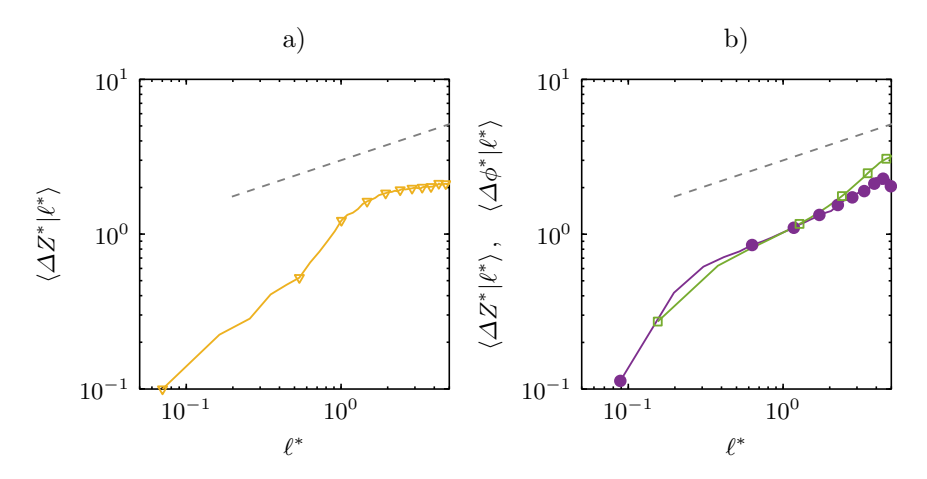


Figure 5.5: Normalized DE scalar difference conditioned on the normalized DE length $\langle \Delta Z^* | \ell^* \rangle$ and $\langle \Delta \phi^* | \ell^* \rangle$. () intermediate Re case, () high Re case and () non-reacting case. The dashed line indicates the theoretical derived scaling.

function [127]: The mean of ΔZ^* conditioned on ℓ^* for the intermediate Refor all DEs within the TNTI is shown in Fig. 5.5a). One observes a clear correlation between the two DE parameters for short elements with $\ell^* < 1$. The scaling exponent is significantly larger than the theoretically derived value. For larger elements, the two parameters appear to be less correlated. However, for the non-reactive case I as well as for the high Re in Fig. 5.5b), a good collapse of the conditional means and a clear scaling of $\langle \Delta \phi^* | \ell^* \rangle$ for a wide range of ℓ^* is observed. Thus, differences in the conditioned statistics of the intermediate Re case can be attributed to low Reynolds number effects. The slightly larger scaling exponent displayed by the conditional means in Fig. 5.5b), compared to the value usually observed in homogeneous isotropic turbulence, can be attributed to the presence of mean shear, as already observed in other non-reactive shear flow by Celani et al. [29] and Attili and In the flamelet regime, the scalar dissipation rate χ serves as the parameter connecting the fields of the reactive species with the turbulent field, cf. eqs. 5.2 and 5.3. The correlation between the DE parameter and χ is therefore of high interest. Conveniently, the DE gradient $g = \Delta Z/\ell$ can be used to relate the DE parameters to the scalar dissipation rate χ . From

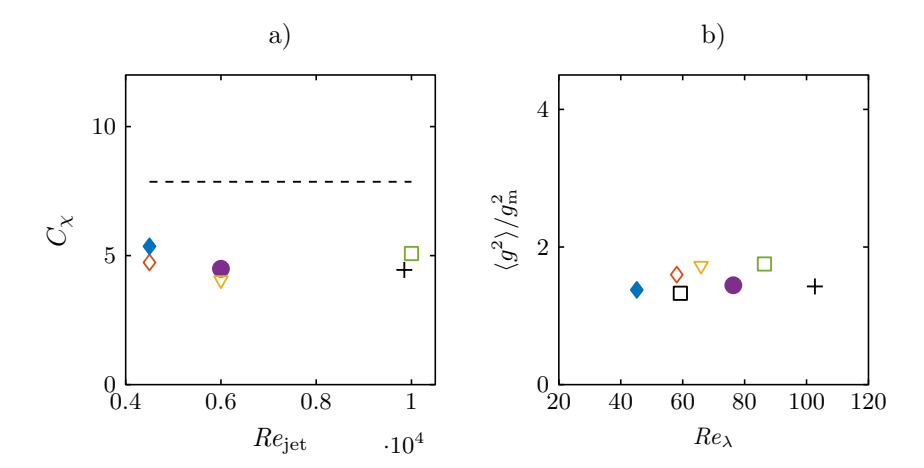


Figure 5.6: a): Average ratio $C_{\chi} = \langle \chi / \left(2D \langle g^2 \right) \rangle$ in the final time step of the respective simulations. b): ratio of the first to the second moment of the DE scalar gradient $\langle g^2 \rangle / g_{\rm m}^2$. \longrightarrow : low Re low dilution case, \longrightarrow : low Re high dilution case, \longrightarrow : intermediate Re case, \longrightarrow : high Re case, \longrightarrow : non-reacting case I and \longrightarrow : non-reacting case II. The dashed black line and black square indicate the isotropic turbulence.

dimensional considerations it follows

$$\chi = 2D \left(\frac{\partial Z}{\partial x_i}\right)^2 \sim Dg^2.$$
(5.5)

The average ratio $C_{\chi} = \langle \chi / (2Dg^2) \rangle$ is shown for the last time step for all investigated cases in Fig. 5.6a). Regardless of configuration and Reynolds number, the average ratio displays a constant value of $C_{\chi} \approx 5$. This indicates for the investigated configurations that the local mixture fraction gradient, and thus, the scalar dissipation rate, can indeed be related to the gradient of the larger local flow topology, as indicated by g. Further, the ratio of the second moment to the mean DE gradient squared $\langle g^2 \rangle / g_{\rm m}^2$ is shown in Fig. 5.6b). No clear influence of Reynolds number is discernible and all cases display similar values for $\langle g^2 \rangle / g_{\rm m}^2 \approx 1.6$. The constant value for the ratio can be explained by the universality of the normalized JPDF $P(\ell^*, \Delta Z^*)$ and the consequently universal ratio of the various moments of $g = f(\ell, \Delta Z)$. Therefore, the mean scalar dissipation rate can be related to the mean DE gradient $\langle \chi \rangle \sim \langle D \rangle g_{\rm m}^2$. Consequently, this signifies that the joint DE statistics can be reconstructed, if the the unconditional mean scalar dissipation rate and Kolmogorov micro scale are known.

5.2 Regimes in Turbulent Non-Premixed Combustion

One of the desirable features of DEs is their space-filling nature, enabling a unique decomposition of the entire scalar field, and therefore, the ability to locally categorize the flame using the DE parameters. A categorization of combustion regimes based on DE parameters is outlined in this section. Similar to the Borghi-Peters regime diagram for turbulent premixed combustion, the turbulent scales are compared to the characteristic combustion scales. In the context of non-premixed combustion, the characteristic combustion scales are provided by the steady state flamelet solution. The DE parameter-based regime diagram and the expected flame structure or lack thereof is depicted in Fig. 5.7

The first DE parameter of choice is the gradient g, as it is closely related to χ , cf. Fig. 5.6a). In the regime diagram, it represents the well-known and investigated influence of the scalar dissipation rate on the reacting scalars and is placed on the abscissa in Fig. 5.7 The first regime boundary is marked by the quenching gradient g_q , at which the heat release within the flame is insufficient to balance the energy transport caused by diffusion. In the flamelet sense, g or χ should be sufficient to characterize the reacting scalars

in flows with high but finite Damköhler numbers as outlined in Peters [91]. However, to account for the interaction of chemical and turbulent scales with Damköhler numbers approaching unity, a second parameter, represented by a second coordinate in the regime diagram, is required.

Representing the effect of the different turbulent scales in the mixture fraction field, the scalar difference ΔZ fills this spot and is therefore shown on the ordinate of the regime diagram in Fig. 5.7. The scalar difference ΔZ is especially fitting, as the gradient trajectories used for the detection of DEs in the mixture fraction fields are linked to the local flamelet coordinates [94]. The turbulence-induced extremal points in the mixture fraction field represent a forced interruption of any diffusive transport, as $\nabla Z = 0$, or in the context of the flamelet eqs. [5.2] and [5.3] $\chi = 0$. The ΔZ of a DE including the stoichiometric iso-surface is therefore the maximum distance in Z-space in which a diffusive transport-dominated structure, such as a flamelet, can exist. Therefore, the second boundary in the regime diagram is marked by the threshold value Z-space (ΔZ)_t below which the diffusive structure of the flame is disrupted too close to the stoichiometric mixture fraction ,and thus the reaction zone, to form a coherent 1D flame structure.

The result is the definition of four regimes. In the top left, for large ΔZ and small g, the "Burning Flamelet" regime is situated. Regions of the flame identified by these DE parameters should adhere to the classical steady flamelet model. The scales in the turbulent Z-field are locally large compared to those imposed by the chemistry, and the individual flamelet solutions in the DE can advance unencumbered for long distances in Z-space, from the fuel side to the oxidizer. The DE gradient stays below quenching values ensuring a burning solution.

The regime in the top right corner, called the "Large Scale Extinction" regime, corresponds to large scale extinction events, such as large rollers stemming from Kelvin-Helmholtz instabilities and the like. Here, the specified "large scale" is the characteristic scale of the extinction inducing event, which is large compared to the scale indicated by the local DE. Within these regions, large cliff-ramp structures with significant strain are generated. Large scale extinct regions such as flame holes [81] [90] correspond to this regime. The extinction in this regime corresponds to the low-Damköhler type extinction caused by eddies of integral scale size. The scale of the extinction events in this regime is expected to be far larger than the individual DE volumes, and the quenching process should occur fairly instantaneously and therefore homogeneously in a single DE.

The regime in the bottom left corner is the "Fine Scale Mixing" regime,

for $g < g_{\rm q}$ and $\Delta Z < (\Delta Z)_{\rm t}$, is characterized by low gradients and small turbulent structures in the Z-field. This is indicative of very short flamelet solutions, and it is questionable if the chemical field in these regions resembles a one-dimensional solution or whether chemical reactions can be sustained. Low gradients and small scalar differences put these regions in the DE regime of "rapid splitting and reconnection" [128], meaning that diffusive fluxes would rapidly change direction depending on the latest pairing of the extremal points in the DE. A flame structure in the traditional sense should not exist in the regions of "Fine Scale Mixing" if ΔZ is small enough and intense turbulent advection becomes the dominating transport mechanism. If the scalar difference is further decreased $\Delta Z < \delta Z_{\rm r}$, with the thickness of the reaction zone in Z-space $\delta Z_{\rm r}$, DEs may penetrate the reaction zone and exist entirely in the reaction zone. The local topology of the flame would be more akin to homogeneous reactors than flamelets.

The last remaining regime is the "Broken Reaction Zone" regime in the bottom right corner. Here one finds small scalar differences in combination with large gradients leading to small scale extinction zones due to locally high turbulence activity. This type of extinction would correspond to a high-Karlovitz type effect, where eddies of the size of the Kolmogorov scale transport radicals out of the inner reaction zone. Contrary to the "Large Scale Extinction" regime, the scales of the "Broken Reaction Zone" quenching events are far smaller. Consequently, quenching would not occur homogeneously within an entire DE resulting in partially burning DEs. The resulting local topology would be characterized by small intermittent pockets of reacting and non-reacting fluid.

In a first step, to ensure that DEs represent a sensible way of decomposing the physical space into sub-units for the purpose of analyzing the interaction between chemistry and turbulence, the PDF of temperature conditioned on the mixture fraction P(T|Z) is compared to the conditional PDF of the DE-averaged temperature $\widetilde{T}_{\rm DE}$. This average is calculated in the following way. The intersecting area of the individual DEs and the Z iso-surface is determined and the temperature in this intersecting area is then averaged. For $P(\widetilde{T}_{\rm DE}|Z)$, this intersecting area additionally serves as a weight in the statistics to account for the various sizes of the DEs. The PDFs of the instantaneous temperature and the DE averaged temperature are shown in Fig. 5.8 for the low Re low dilution case and intermediate Re case for three exemplary values of the mixture fraction. One observes a characteristic bimodal shape of the PDFs for most of the Z values, with the maximum at low temperatures corresponding to the extinct regions of the iso-surface and the maximum at

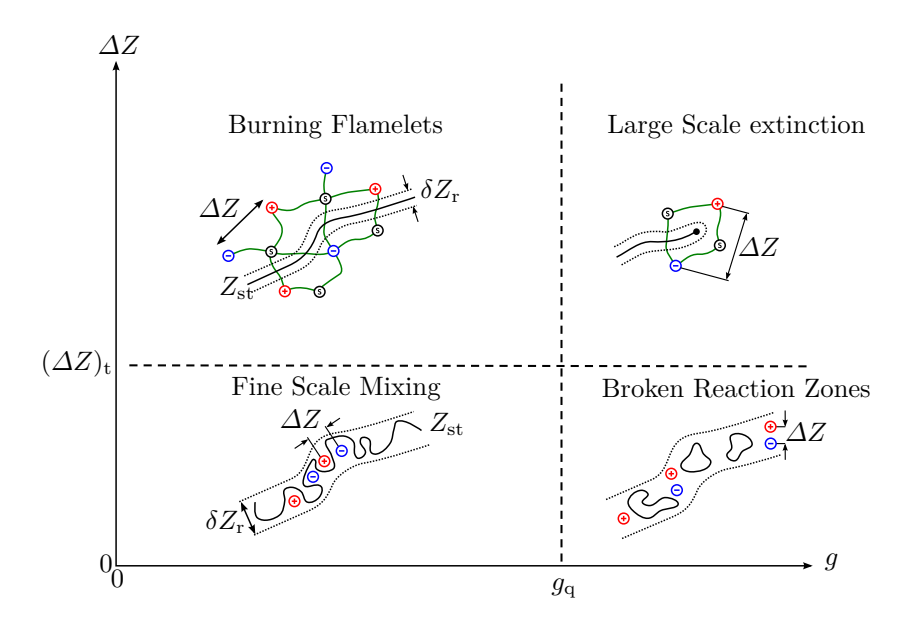


Figure 5.7: DE parameter based regime diagram for turbulent non-premixed combustion. The solid lines indicate a burning solution at $Z_{\rm st}$ and the dotted lines represent the thickness of the reaction zone.

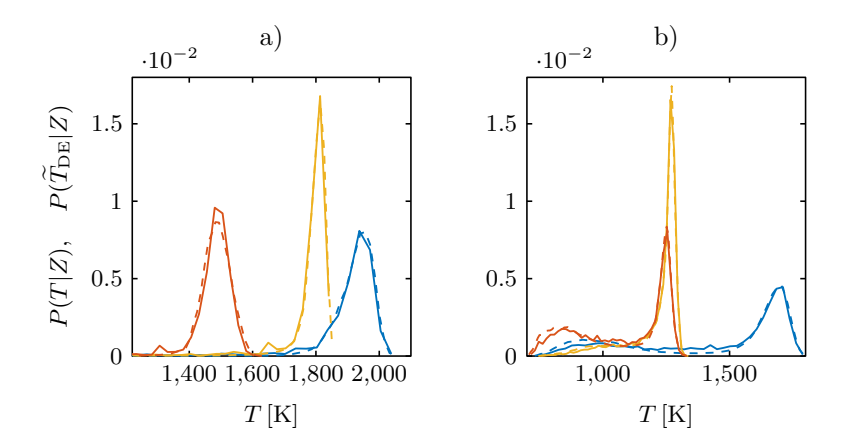


Figure 5.8: (solid lines): PDFs of the temperature P(T|Z) conditioned on three different values of the mixture fraction and (dashed lines): PDF of the temperature averaged within individual DEs $P(\widetilde{T}_{\rm DE}|Z)$. Red: $Z=0.5Z_{\rm st}$, blue: $Z=Z_{\rm st}$ and yellow: $Z=1.5Z_{\rm st}$, a): low Re low dilution case, b): intermediate Re case.

high T corresponding to the burning solution. No differences between the PDFs of the temperature and the DE-averaged temperature can be observed. These results are indicative of the fact that the flow compartmentalization by means of DEs is indeed sensible, as the full PDF can be reconstructed from the DE-averaged temperature with negligible errors. The categorization based on the proposed regime diagram in Fig. 5.7 is applied to the surface of the stoichiometric mixture fraction of the four reacting cases. The quenching gradient is estimated by using the conditional average of the DE gradient at the scalar dissipation corresponding to quenching conditions for the laminar 1D flamelet $g_q = \langle g | \chi = \chi_q \rangle$. This results in a quenching gradient for the low Re low dilution case of $g_{\rm q}=110\,{\rm s}^{-1},$ while it is $g_{\rm q}=92\,{\rm m}^{-1},$ $g_{\rm q}=89\,{\rm m}^{-1}$ and $g_q = 90 \,\mathrm{m}^{-1}$ for the low Re high dilution case, intermediate Re case, and high Re case, respectively. The reaction thickness δZ_r in Z-space is estimated locally by fitting the inner reaction zone of the heat-release profile $\omega_T(Z)$ of the steady state flamelet solution with a Gaussian profile. The reaction zone thickness is then defined as the half width of the Gaussian. This procedure is shown for conditions close to quenching for the two investigated dilutions in Fig. 5.9a). For local dissipation rates greater than the quenching dissipation rate, the reaction zone thickness at quenching conditions is chosen.

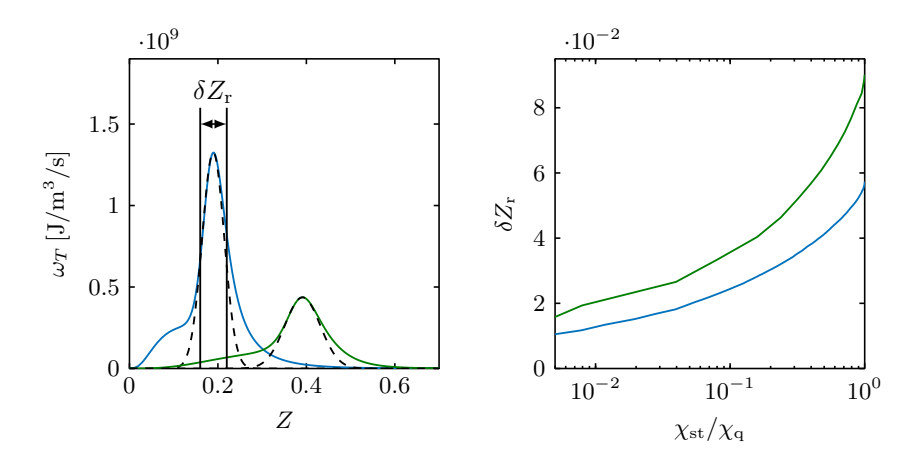


Figure 5.9: Left: heat release rate ω_T for steady state flamelet solutions at quenching scalar dissipation rates (solid lines) and the inner reaction zone approximation by means of a Gaussian profile (dashed lines). Blue: low dilution corresponding to the boundary conditions in the low Re low dilution case, green: boundary conditions corresponding to the low Re high dilution case, the intermediate Re case and the high Re case. Right: variation of the inner reaction zone thickness $\delta Z_{\rm r}$ with $\chi_{\rm st}$.

The impact of the scalar dissipation rate at stoichiometric conditions on the reaction zone thickness is shown in Fig. 5.9b), where an approximately 60% wider δZ_r for the high dilution cases is observed.

The reacting scalars on the iso-surface of the stoichiometric mixture fraction are averaged conditioned on the normalized DE parameters $\Delta Z' = \Delta Z/\delta Z_{\rm r}$ and $g' = g/g_{\rm q}$ to achieve a comparison between the chemical and turbulent scales and check the validity of the proposed regime diagram. This is shown for the temperature field for all reacting cases in Fig. 5.10 and for the OH mass fraction in Fig. 5.11. The conditional means of the reacting scalars display a good consistency with the assumptions of the previously outlined DE-based regime diagram. For all four cases, high values of the conditional means $\langle T \rangle$ and $\langle Y_{\rm OH} \rangle$ are observed for high values of $\Delta Z'$ and low values of g', which is consistent with the idea of classifying the flame as burning flamelets for these values of DE parameters. Here, the reacting scalars display the same trends with regards to rising g' as one would expect with an increase in χ . The second regime boundary is set as $(\Delta Z)_{\rm t} = 15\Delta Z'$, as the conditioned reacting scalar values decrease significantly. This value for $\Delta Z'$ is consistent

across all Reynolds numbers and across the different dilutions. The reacting scalars are more susceptible to quenching caused by gradients in the mixture fraction field for $\Delta Z < (\Delta Z)_{\rm t}$, as similar values of g yield significantly lower values of the mean reacting scalars.

The regime boundary at q'=1 proves to be sensible as well with low values of the mean reacting scalars indicating extinction for g' > 1. The locally high values for $\langle T \rangle$ and $\langle Y_{\text{OH}} \rangle$ in the "Large Scale Extinction" regime, present only in the low Re case and and intermediate Re case, are not present in the high Re case and can be attributed to the aforementioned low Reynolds number effects which cause q and χ to be locally less correlated. The range of values of the normalized DE parameters $\Delta Z'$ and g' observed in the individual cases and the implied regime contributions to the overall combustion is consistent with the probability of observing small scale structures in the flame and extinct regions in Figs. 4.3 and 4.4 and the overall levels of extinction in The fine scale regimes "Fine Scale Mixing" and "Broken Reaction Zones" are characterized by small structures in mixture fraction space and display highly turbulent behavior. To gain a deeper understanding of the fine scale mixing regimes, the mean temperature in the extremal points, i.e. at the minimum mixture fraction, $\langle T_{\rm DE,min} \rangle$, and at the maximum mixture fraction, $\langle T_{\rm DE,max} \rangle$, of the DEs crossing the iso-surface is conditioned on the normalized DE parameters as shown in Fig. 5.12. High values for the mean temperature in the extremal points can be observed in a triangular region for $\Delta Z' < 10$ and q' < 1. The values of the mean reacting scalars are comparable to those obtained at the stoichiometric iso-surface, as observed for the small $\Delta Z'$ and q' in Figs. 5.10 and 5.11. The presence of extremal points of the mixture fraction field within the reaction zone further validates the idea of a "Fine Scale Mixing" regime. The DEs in this regime resemble fully reacting sub-regions of the flame from the minimum to maximum. Due to the small g' in this triangular region, the ℓ of the DE occupying this part of the flame ranges from $5\eta < \ell < 50\eta$. This indicates the presence of large and fully reacting structures, which are significantly wider than the reaction zones in the flamelet solution. The values of $10 < \Delta Z' < 15$ might be viewed as a transition range between two burning regimes.

For a final analysis of the sensibility of the DE-based regime diagram and to estimate the level of extinction in the individual regimes, the marginal PDF of the temperature at stoichiometric conditions $P(T_{\rm st})$ is additionally conditioned on the individual combustion regimes. This is shown for two time steps for the high Re case in Fig. 5.13 As observed in Fig. 5.8b), two peaks in the PDFs are present, one for low temperatures and one for high

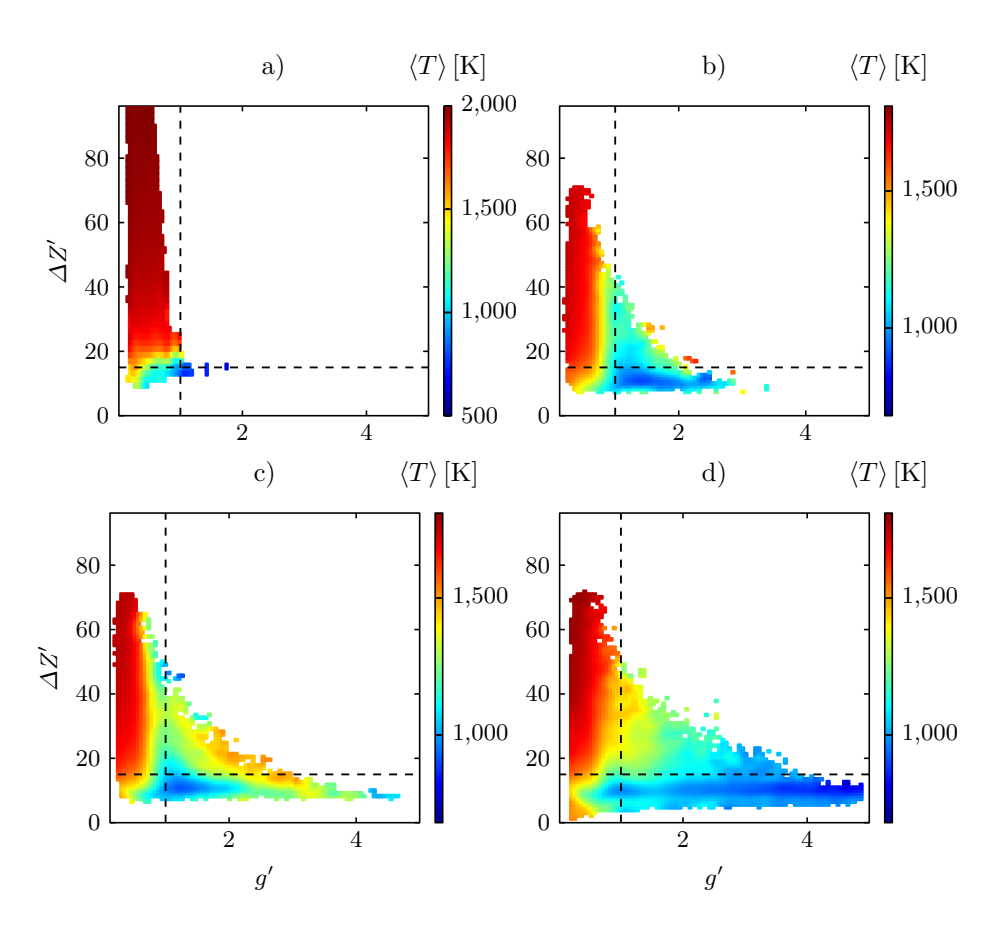


Figure 5.10: Mean temperature $\langle T \rangle$ conditioned on normalized DE parameters $\Delta Z' = \Delta Z/\delta Z_{\rm r}$ and $g' = g/g_{\rm q}$. Dashed lines indicate regime boundaries. a): low Re low dilution case, b): low Re high dilution case c): intermediate Re case and d): high Re case.

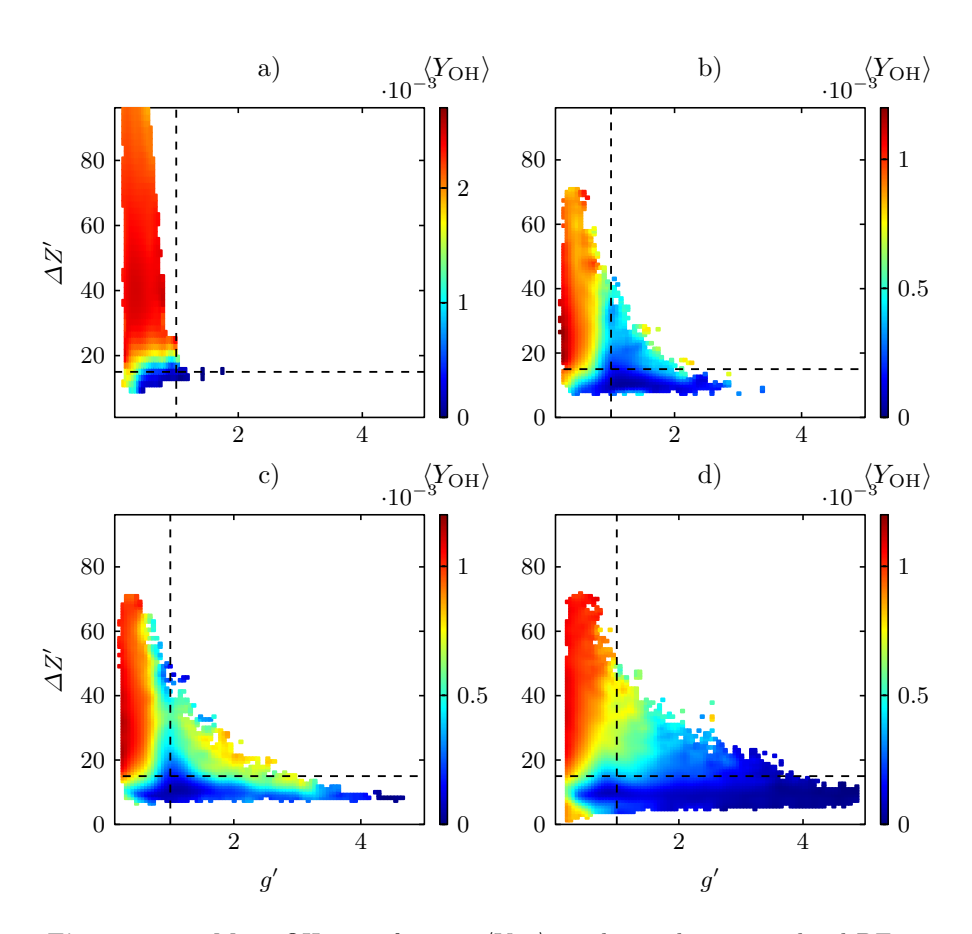


Figure 5.11: Mean OH-mass fraction $\langle Y_{\text{OH}} \rangle$ conditioned on normalized DE parameters $\Delta Z'$ and g'. Dashed lines indicate regime boundaries. a): low Re low dilution case, b): low Re high dilution case c): intermediate Re case and d): high Re case.

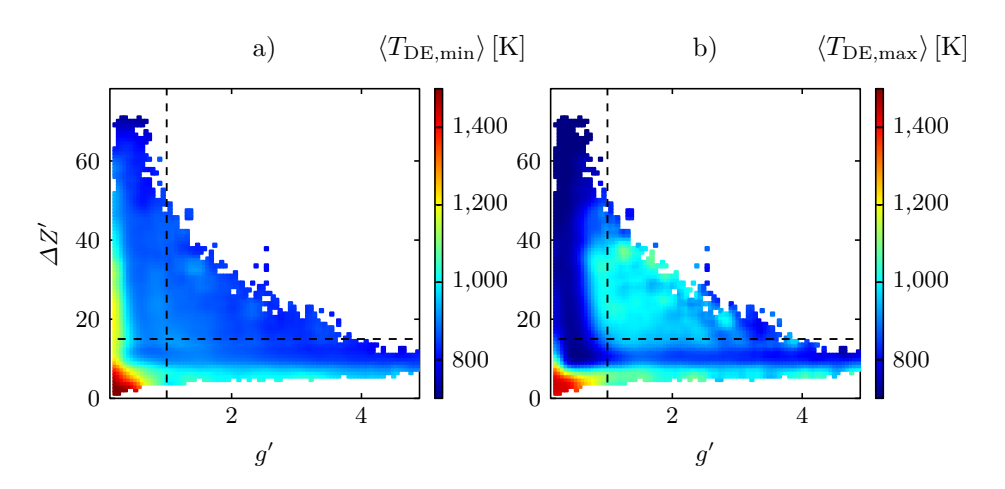


Figure 5.12: Mean temperature a): in the minima $\langle T_{\rm DE,min} \rangle$ and b): in the maxima $\langle T_{\rm DE,max} \rangle$ of DEs crossing the stoichiometric iso-surface conditioned on the normalized DE parameter g' and $\Delta Z'$ for the high Re case. The dashed lines indicate the regime boundaries.

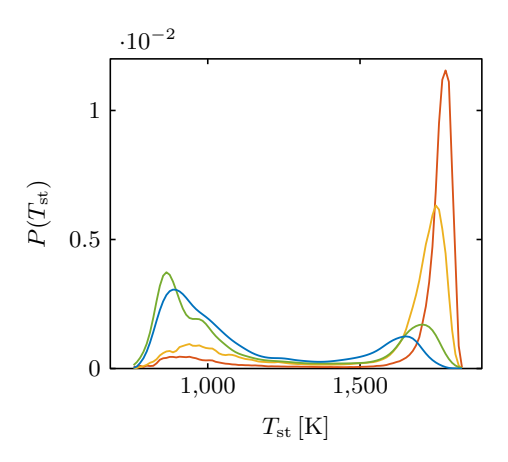


Figure 5.13: PDF of the temperature conditioned on the stoichiometric mixture fraction, and on the individual regimes in the final time step of the high Re case. (): "Burning Flamelet" regime, (): "Fine Scale Mixing" regime, (): "Large Scale Extinction" regime and (): "Broken Reaction Zone" regime.

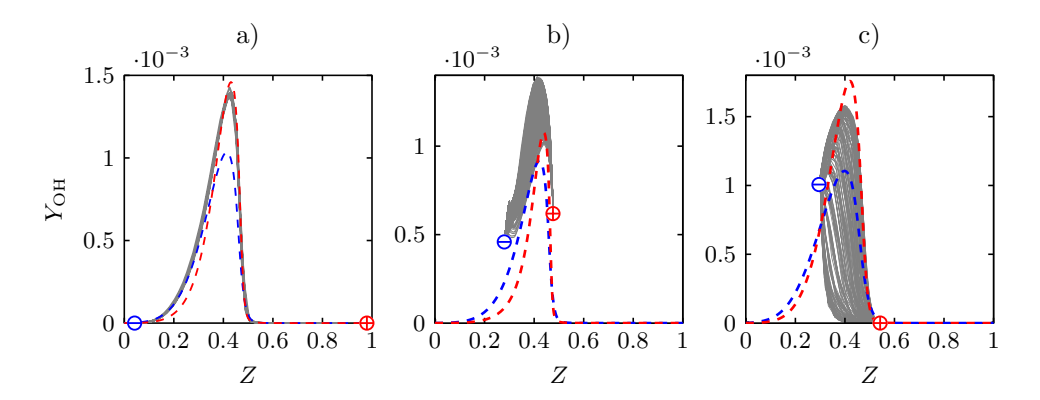


Figure 5.14: (Gray lines): Mass fraction of OH radicals obtained along all gradient trajectories of a single DE. The steady state flamelet solution for the DE averaged scalar dissipation rate at stoichiometric conditions $\widetilde{\chi_{\rm st}}_{\rm DE}$ is indicated by the blue dashed line and red dashed line for the non-unity Lewis number and unity Lewis number solution, respectively. a): DE obtained from the "Burning Flamelet" regime, b): DE from the "Fine Scale Mixing" regime and c): DE obtained from the "Broken Reaction Zones" regime.

temperatures corresponding to burning and extinct parts of the stoichiometric iso surface, respectively. For the extinction regimes, the global maximum of the probability density is located at low temperatures with only minor amounts in temperature-ranges that can sustain combustion. The remaining low amounts of probability density of low temperature in the "Burning Flamelets" regime can be explained by parts of the flow undergoing re-ignition or by locally too high values of χ for re-ignition of previously extinguished parts of the flow.

5.2.1 Local Flame Analysis

As the gradient trajectories in mixture fraction space are equivalent to the physical coordinates of the flamelet solution in physical space, a non-local comparison with the steady state flamelet solution in a physically meaningful framework is straightforward. For a more detailed investigation, the instantaneous mass fraction of OH obtained along all gradient trajectories used in the detection of exemplary DEs are plotted in the mixture fraction space in Fig. 5.14. This is done for three representative DEs obtained from the "Burning Flamelet" regime, the "Fine Scale Mixing" regime, and the

"Broken Reaction Zone" regime in the last time step of the high Re case. The representative DEs are obtained from burning regions of the stoichiometric iso-surface, as shown in Fig. [4.5]. The DEs are of comparable volume and possess a similar intersecting area with the iso surface of the stoichiometric mixture. $Y_{\rm OH}$ along the gradient trajectories is compared to the steady state flamelet solutions obtained from the steady state flamelet solution using the averaged scalar dissipation rate at the intersecting area of the DE and the stoichiometric mixture fraction iso surface $\chi_{\rm StDE}$.

For the DE obtained from the "Burning Flamelet" regime, shown in Fig. 5.14a), the mass fractions along the individual trajectories collapse perfectly with the unity Le flamelet solution for a wide range of Z values. The indiscernibility of Y_{OH} between the individual trajectories is very consistent with the flamelet assumption of a change of any reactive scalar exclusively in the Z-direction. However, for the DE obtained from the "Fine Scale Mixing" regime in fig. 5.14b), Y_{OH} displays a wide range of values for a given value of Z, especially for mixture fractions close to stoichiometry. Large departures from both flamelet solutions can be observed with $Y_{\rm OH}$ obtained in the DE having consistently higher values, even in the extremal points. The rather large inhomogeneity of the reacting scalar on an iso-surface of Z within a small spatial sub-unit, such as a DE, clashes with the 1D flamelet assumption, as additional transport of the reacting scalars is expected to take place tangentially to the mixture fraction coordinate. The mass fraction of OH obtained from the "Broken Reaction Zones" regime, shown in fig. 5.14c) shares this characteristic. While the range of values is significantly larger than in the DEs of the other regimes, some trajectories display values corresponding to an extinct solution while others are fully burning, which is consistent with the assumption of a broken reaction zones regime.

The effect of the inhomogeneity of reactive scalars for a specific iso-value of Z, which is observed for the exemplary DEs in the "Fine Scale Mixing" regime and "Broken Reaction Zones" regime, can be statistically measured by the coefficient of variation of a reactive scalar in a DE:

$$c_{\text{v,ff}}(Z) = \frac{\sqrt{\widetilde{\psi''^2}_{\alpha,\text{DE}}(Z)}}{\widetilde{\psi}_{\alpha,\text{DE}}(Z)}.$$
 (5.6)

The mean coefficient of variation of OH at stoichiometry, conditioned on the normalized DE parameters $\langle c_{\rm v,OH}(Z_{\rm st})|g',\Delta Z'\rangle$, is shown for the low Re high dilution case and the intermediate Re case in Figs. 5.15a) and b). The coefficient of variation is low in the "Burning Flamelet" regime for both cases and is also relatively low for the "Large Scale Extinction" regime. As partly

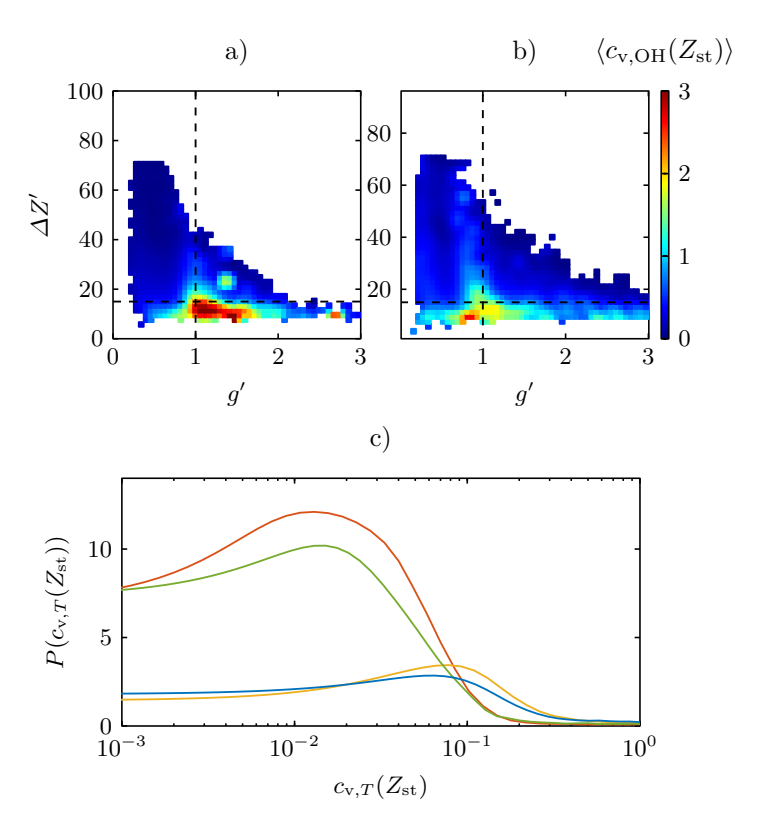


Figure 5.15: Mean DE coefficient of variation of the OH mass fraction $\langle c_{\rm v,OH}(Z_{\rm st})\rangle$ conditioned on the normalized DE parameters g' and $\Delta Z'$ at the final time step. a) low Re high dilution case; b) intermediate Re case; c) PDF of the DE coefficient of variation $P(c_{\rm v,OH}(Z_{\rm st}))$ conditioned on the individual regimes in the burning regions of the stoichiometric iso-surface for the high Re case. (\square): "Burning Flamelet" regime, (\square): "Fine Scale Mixing" regime, (\square): "Large Scale Extinction" regime and (\square): "Broken Reaction Zone" regime.

quenched DEs would display high values of the coefficient of variation, the low values support the notion of larger extinction events where regions spanning the entire cross section of the DE are quenched simultaneously. High values for the coefficient of variation are observed in both the "Fine Scale Mixing" regime and the "Broken Reaction Zones" regime. This indicates that the previously observed characteristics for the three exemplary DEs in fig. [5.14a)-c) are representative of the entire flame.

The PDF of the coefficient of variation of the temperature $P(c_{v,T}(Z_{st}))$ conditioned on the individual regimes and the burning regions of the high Re case is shown in fig. 5.15c). It shows that previously observed behavior of the coefficient of variation with regard to the regimes extends to the temperature field. The difference in $c_{v,T}$ between the large-scale and the fine-scale regimes is roughly one order of magnitude. While comparable to the "Large Scale Extinction" regime, the "Burning Flamelet" regime displays the lowest $c_{v,T}$. In summary, independent of the value of g, the reacting scalar fields display high local homogeneity in the "Burning Flamelet" regime and "Large Scale Extinction" regime, while the "Fine Scale Mixing" regime and the "Broken Reaction Zones" regime are characterized by turbulence induced inhomogeneity.

5.2.2 Temporal Evolution of the Combustion Regimes

Finally, the temporal evolution of the individual regime's contribution to the overall combustion process is investigated. Besides offering ΔZ as a value to quantify "large scale" or "fine scale" interaction, the approach of using DE parameters for a classification of the combustion regimes offers a signifiant additional advantage over traditional statistical methods. Instead of comparing one single characteristic turbulence scale, which is defined for the entire domain (like the Kolmogorov micro scale η in the Karlovitz number or the eddy turnover time τ in the Damköhler number) to the characteristic flame scale, a local comparison using DE parameters is possible. Every material point on the stoichiometric iso-surface can be characterized by the two DE parameters. Therefore, all of these material points can be classified individually by the DE-based regime diagram. The large range of turbulent structures simultaneously present in the various cases consequently leads to a certain degree of coexistence of combustion regimes in the conditions investigated in this work. The substantial advantage of using a local estimate for the turbulence scales allows for the quantification of the local conditions. For the coexistence of burning and extinct regimes, this was always implicitly assumed by the simultaneous presence of flame holes and edge flames in flows

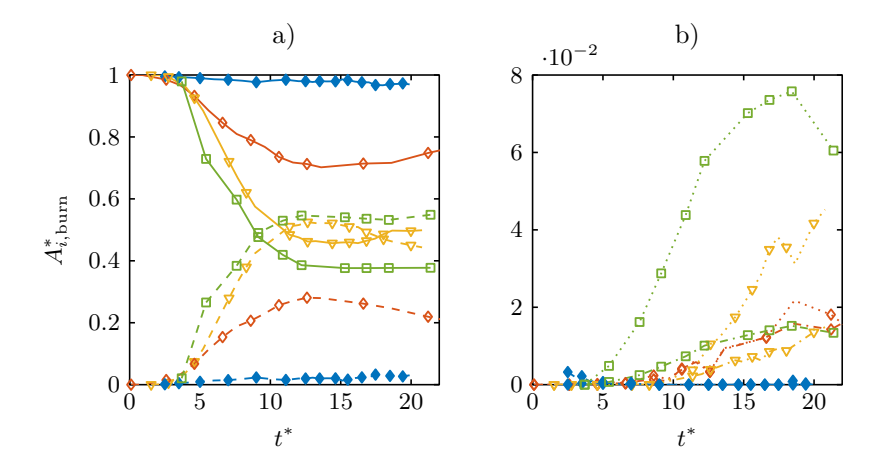


Figure 5.16: Temporal evolution of the normalized area of the stoichiometric iso surface attributed to the individual regimes $A_{i,\text{burn}}^* = A_{i,\text{st,burn}}/A_{\text{st,burn}}$, conditioned on the burning regions. a): solid lines indicate the "Burning Flamelet" regime and dashed lines the "Fine Scale Mixing" regime. b): dash dotted lines indicate the "Large Scale Extinction" regime and dotted lines the "Broken Reaction Zones" regime. \(\brace{\phi} \): low Re low dilution case, $(\brace{\phi} \)$: low Re high dilution case, $(\brace{\phi} \)$: intermediate Re case and $(\brace{\phi} \)$: high Re case.

for which the average scalar dissipation rate remained well below quenching values [80], [8].

To achieve the local quantification of the combustion regimes, the burning area of the stoichiometric iso-surface attributed to the individual regimes in the burning regions of the flow $A_{i,\text{st,burn}}(t^*)$ is shown for all four reacting cases in fig. 5.16a). As the overall burning area increases significantly over time, normalization is achieved with the overall burning area $A_{\text{st,burn}}(t^*)$, which is identical to the one shown in fig. 4.5b).

As expected, the combustion is classified as the "Burning Flamelet" regime in the early time steps of all four cases. Later, the burning regions are almost completely classified as either "Burning Flamelet" regime or "Fine Scale Mixing" regime. The relative contribution of the "Fine Scale Mixing" regime increases with the higher dilution and the higher Reynolds number. While the "Burning Flamelet" regime and the "Fine Scale Mixing" regime possess roughly the same area in the last time step of the intermediate Re case, the "Fine Scale Mixing" regime is the dominant regime in the final time step of the high Re case.

The temporal evolution of the normalized area of the stoichiometric isosurface in the burning regions attributed to the "Large Scale Extinction" regime and the "Broken Reaction Zones" regime is shown in fig. 5.16 b). Consistent with the assumption of the regimes, the areas of both the "Large Scale Extinction" regime and the "Broken Reaction Zones" regime are very low in the burning regions, which is emphasised by the significantly lower range of values on the ordinate. Consequently, the overall contributions of the two regimes to the stoichiometric iso-surface in the burning regions in the final time step ranges from 0% for the low dilution low Re case to only 7% in the high Re case.

The burning area in the two regimes might be attributed to ongoing extinction events in these time steps and is well correlated with the point in time, as well as with the ratio of burning regions of the stoichiometric iso surface to the overall stoichiometric iso surface, c.f. fig. [4.5]b). The area of the "Large Scale Extinction" regime is approximately the same for all three high dilution cases, which can be attributed to the comparable value of the Damköhler numbers. However, the temporal evolution of the area of the "Broken Reaction Zones" shows a clear dependence on the Reynolds numbers.

6 Dissipation Element Analysis of Turbulent Premixed Combustion

In turbulent flames, various combustion regimes exist which pose different implications to the accompanying modeling procedure. For premixed combustion, the so-called "Borghi-Peters-diagram" can be constructed [95]. Turbulent scales, such as the Kolmogorov length, are compared to different scales of the flame. To test the underlying theory of the combustion diagram by means of DNS, a set of simulations of spatially evolving jet flames situated in the thin reaction zone regime was employed by Luca et al. [83]. To achieve a meaningful comparison between the local turbulent and chemical scales, a procedure employing a space-filling decomposition to assure that all interactions are being considered is required. In the following section, the DE analysis is applied to the temperature fields of three premixed flame DNS whose details will be outlined in the section below. Since the temperature can be interpreted as a progress variable C in the context of premixed combustion, the gradient trajectories used in forming a DE can be interpreted as the three-dimensional physical coordinates a flamelet solution occupies in physical space. Then, DEs can be regarded as groups of flamelets, which share the same start and end points in space and the same temperature at the extremal points. In addition to using the DE length ℓ To investigate the difference of the turbulent scales obtained from scalar fields of reacting and non-reacting flows, the DE analysis is additionally applied to passive scalar fields of a spatially evolving jet and isotropic homogeneous turbulence.

6.0.1 Configurations

The DE analysis was applied to three DNS of spatially evolving methane jet flames in the Bunsen burner configuration. Only a brief description is included here since additional details are available in previous works where the same dataset has been employed [83] $\boxed{3}$. The cases are statistically homogeneous in the span-wise z direction and inhomogeneous in the stream-wise x and cross-stream y direction. The jet Reynolds number is set to 5,600, 11,200 and 22,400 for the Low Re case, the Intermediate Re case and the High Re case, respectively. The jet Reynolds number is varied by changing the slot width H while keeping the jet bulk velocity U constant. In this fashion, the small scales

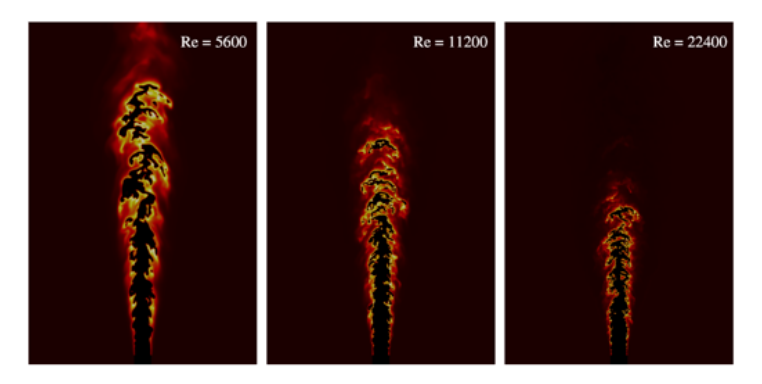


Figure 6.1: Atomic oxygen mass fraction in the x-y center plane of the three DNS of the Bunsen burner configuration. The yellow colored regions correspond to high values of the mass fraction, and brown colored regions to low values.

of turbulence and the Karlovitz number are kept approximately constant while the integral scales increases with the Reynolds number. The DNS feature lean premixed methane/air flames with an equivalence ratio of $\phi=0.7$ and a temperature of the unburned mixture of $T_{\rm u}=800{\rm K}$, which is common to stationary gas turbines. The temperature and species concentrations in the co-flow correspond to the equilibrium state of the burned mixture. The laminar burning velocity is $s_{\rm L}=1.01{\rm ms}^{-1}$ and the temperature-gradient based laminar flame thickness is $\delta_{\rm L}=110\mu{\rm m}$. To illiustrate the configuration, the atomic oxygen mass fraction in the x-y center plane of the three DNS is shown in Fig. [6.1]

The reactive, unsteady Navier-Stokes equations are solved in the low Mach number limit $\boxed{117}$, all transport properties are computed with a mixture-average approach $\boxed{10}$, and a skeletal methane mechanism with 16 species and 72 reactions $\boxed{82}$ is employed. The resolution $\Delta=20$ micron is such that $\delta_L/\Delta\sim 6$ and $\Delta/\eta<2$ at all times, where η is the Kolmogorov scale. A discussion of the resolution requirements and an assessment of the quality of the solution is discussed by Luca et al. $\boxed{83}$. Additional details regarding the spatially evolving DNS are summarized in Tab. $\boxed{6.1}$.

The Bunsen burner configuration possesses several fundamental differences to the isotropic turbulence, on which the DE analysis was most extensively applied and for which the underlying theory was developed. To isolate effects on the DE parameter statistics, three additional non-reactive DNS cases are

	Low Re	Intermediate	${\bf High}\ Re$
	Flame	Re Flame	Flame
Jet Reynolds number Re_0	5600	11200	22400
Karlovitz number Ka	23	21	21
Jet width H [mm]	1.2	2.4	4.8
Jet bulk velocity U [m/s]	100	100	100
Turbulence intensity u' [m/s]	10.0	9.8	11.7
Integral length scale $\ell_{\rm t}$ [mm]	0.54	0.67	1.1
Kolmogorov scale η [μ m]	23	25	25
$\overline{N_x}$	1440	2880	5760
N_y	960	1920	3840
N_z	256	512	1024

Table 6.1: Simulation parameters of the reacting configurations investigated in this chapter. The turbulence statistics are evaluated at the stream-wise position of $x/l_{\rm F} = 0.6$.

included in this study. To investigate the difference between the turbulent scalar fields in a reacting and a non-reacting flow, a DNS using the exact configuration and inflow velocity field of the Low Re Flame was conducted omitting the combustion and using the homogeneous material properties of the unburned lean premixed air/methane mixture. A passive scalar was added with boundary conditions of $\phi = 1$ in the slot and $\phi = 0$ in the coflow. The Schmidt number of the passive scalar is set to Sc = 1. This DNS is henceforth called the Inert Spatially Evolving case and additional information is given in Tab. [6.1]. To identify the effects of the spatially evolving nature of the previously outlined cases on the scalar fields, DNS data of a temporally evolving non-reacting jet, referred to as the Inert Temporally Evolving case, are included in this investigation. The non-dimensional DNS features a comparable Jet Reynolds number to the intermediate Re Flame of $Re_0 = 9,850$. Further details regarding the setup and numerical methods of the Inert Temporally Evolving case can be found in in Sec. [4.2.1]

As a final point of reference for the analysis, a passive scalar field of a DNS of forced isotropic turbulence with a Taylor-based Reynolds number of $Re_{\lambda} = 88$ is used, which is similar to those of the High Re Flame and the Inert Temporally evolving case. The computational domain is a box with periodic boundary conditions and a non-dimensional length of 2π . The domain is discretized with 512^3 grid points. Statistical steadiness is ensured via the

stochastic forcing scheme. Again, the subsequent investigation is based on a passive scalar with a unity Schmidt number. Additional information can be found in Gauding [57]. This case will be referred to as the Inert Isotropic case in the following sections.

6.1 DE Analysis of the Temperature Fields in Premixed Jet Flames

6.1.1 Marginal Statistics

The DE analysis is applied to the temperature fields of the reacting DNS in two different stream-wise regions. This is necessary as statistics are bound to change as the flow is traversed in the stream-wise direction. The upstreamregion corresponds to a stream-wise region of $x \approx 0.27 L_{\rm F}$ to $x \approx 0.54 L_{\rm F}$, where $L_{\rm F}$ is the mean flame length. In this region, the turbulence is already sufficiently evolved for a DE analysis. Here, the two flame fronts are approximately parallel. The second region, henceforth called the downstream region, is situated at $x \approx 0.54 L_{\rm F}$ - $0.8 L_{\rm F}$, where the flame fronts show the first signs of closing in on themselves. These two stream-wise regions are also chosen for the DE analysis of the passive scalar in the Inert Spatially Evolving case to achieve a meaningful comparison of the statistics in the spatially evolving cases. In both the Inert Temporally evolving case and the Inert Isotropic case, the entire passive scalar fields were subjected to DE analyses. In the free shear flow cases, DEs whose extremal points are located in the irrotational regions of the flows were omitted from the statistics. These regions were identified using the turbulent/non-turbulent interface criterion of Bisset, Hunt, and Rogers. 17.

The DE analysis for the reacting cases is shown in Fig. $\boxed{6.2}$ for the x-y center plane of the temperature fields in the upstream region. On the top part of the figure, the temperature fields are shown as well as a black contour indicating the iso line of the temperature where the heat release peaks to mark the region of the flame front. On the bottom part of Fig. $\boxed{6.2}$ the DE analysis is shown in a mirrored fashion. One observes that, compared to the jet thickness in the cross-stream direction, the DEs of the Intermediate Re Flame are a lot smaller in scale than in the Low Re Flame. In addition, the various shapes and sizes of the DEs intersecting the flame front indicate a wide range of local turbulent scales interacting with the flame. The anisotropic nature of the scales becomes apparent when the spatial change in DE sizes is considered. In both cases, the DE sizes grow moving away from the jet core



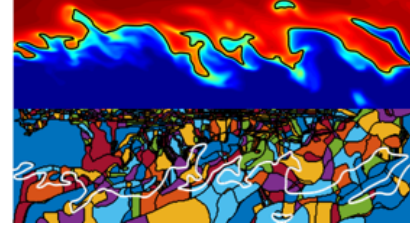


Figure 6.2: Top part: upstream x-y center plane of the temperature fields. The red colored regions correspond to high temperatures, blue color to low temperature regions. The black contour indicates the iso-surface of the maximum heat release. Bottom part: The mirrored corresponding DE analysis of the temperature. The DEs are colored individually and encompassed in a black contour. Left: Low Re Flame, right: Intermediate Re Flame.

and approaching the flame front.

As a reference, the cross-section of the DE analysis of the passive scalar field in the Inert Isotropic case is shown in Fig. [6.3]. One observes a wide range of sizes and shapes of the DEs similar to the ones previously beheld in the analysis of the jet flames in Figure 2. As expected, the isotropic nature of the scalar field carries over to the distribution of the DEs with no apparent preferential orientation of the DEs.

These qualitative observations will be quantified in the following section via statistics of the DE parameters. First, the volume averaged values of the DE parameters, the mean separation DE length $\ell_{\rm m}$, the mean DE scalar difference $\Delta\phi_{\rm m}$, or mean DE temperature difference $\Delta T_{\rm m}$ for the reacting cases, will be investigated as they provide the means of normalization in the subsequent analysis. The mean separation length $\ell_{\rm m}$ normalized with the Kolmogorov micro-scale η is shown in Fig. 6.4. The previously reportet scaling of $\ell_{\rm m}$ with η holds true for the Inert Spatially Evolving case analyzed here. Spanning a wide range of Reynolds numbers and three different flow configurations, the ratio of the two length scales comes to $\ell_{\rm m} \approx 30\eta$, which is consistent with previous DE investigations of non-reacting flows. For the Inert Spatially Evolving case, $\ell_{\rm m}/\eta$ collapses in both upstream and downstream regions. However, for the reacting cases, $\ell_{\rm m}/\eta$ is approximately twice as large, indicating larger turbulent length scales in the temperature field as compared to the passive scalar field. The scaling with the Kolmogorov micro-scale is not as evident as in the inert cases with $\ell_{\rm m} \approx 86\eta$ for the Low Re Flame and $\ell_{\rm m} \approx 62\eta$ the Intermediate Re Flame. However, this could be attributed to



Figure 6.3: DE analysis of the passive scalar field in the Inert Isotropic case. The DE are colored individually and encompassed in a black contour.

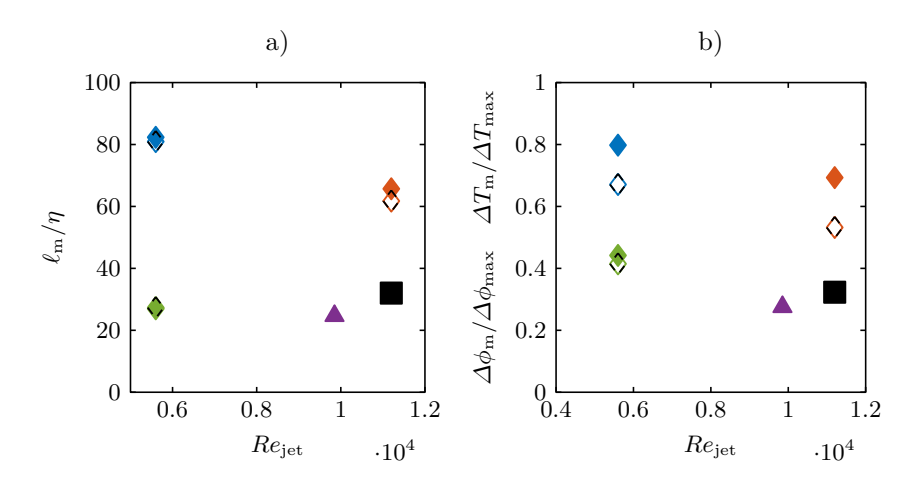


Figure 6.4: Normalized mean DE length $\ell_{\rm m}/\eta$. b): Normalized mean DE differences $\Delta\phi_{\rm m}/\Delta\phi_{\rm max}$ and $\Delta T_{\rm m}/\Delta T_{\rm max}$. The blue, red and green diamonds correspond to the Low Re Flame, Intermediate Re Flame and Inert Spatially Evolving case, respectively. The solid symbols indicate the upstream region; the hollow, black dashed symbols indicate the downstream region. The Inert Temporally Evolving case and the Inert Isotropic case are indicated by the solid purple triangle and black square, respectively. The abscissa position of the Inert Isotropic case was chosen arbitrarily, as no jet Reynolds number exists.

the low Reynolds number in the Low Re Flame.

The higher values for, $\ell_{\rm m}/\eta$ can be attributed largely to two effects. The first effect is the dilatation resulting from the inherent different densities in the extremal points, not present in the passive scalar extremal points. The different densities cause a relative velocity between the extremal points, which counteracts the drift velocity of the extremal points. Assuming the lifetime of the DE in the Diffusive drift region to be of the order of the Kolmogorov time τ_{η} , the dilatation causes $\ell_{\rm m}$ to be enlarged significantly for the premixed reacting cases, which display high values of $\Delta T_{\rm m}$ and, therefore, a large difference in density. A second effect not present in the non-reactive cases is the non-unity Schmidt number $Sc = \nu/D \approx 0.7$ of the temperature fields in the reacting cases. To account for larger turbulent scales due to a higher diffusion coefficient, the Batchelor scale $\lambda_{\rm B} = \eta S c^{-0.5}$ might be a more suitable scaling length accounting for the larger normalized DE length, which would lead to an approximately 20% smaller ratio. Overall, with the inherent uncertainty left in estimating Kolmogorov scale and considering the vastly different configurations and range of Reynolds numbers the DE analysis is applied to, these results indicates that the Kolmogorov scaling of $\ell_{\rm m}$ applies to non-premixed reacting flows as well. While there is only a slight difference of $\ell_{\rm m}/\eta$ from the upstream to the downstream region for the Low Re Flame, the ratio decreases for the Low Re Flame. The assumption of the "thin reaction zones" is reflected in the value of the mean length in temperature fields of $\ell_{\rm m} \approx 10.1 \delta_{\rm L}$ and $\ell_{\rm m} \approx 9.8 \delta_{\rm L}$ for the Low Re Flame and the intermediate Re Flame, respectively.

The mean scalar difference $\Delta\phi_{\rm m}$ and $\Delta T_{\rm m}$ are shown in Figure 4b). Normalization was achieved with the maximal possible scalar difference in the respective domains $\Delta\phi_{\rm max}$ and $\Delta T_{\rm max}$. For the reacting cases, this is the temperature difference between the burned and the unburned $\Delta T_{\rm max} = T_{\rm b} - T_{\rm u} = 1400~{\rm K}$. The smallest ratio is seen in the Inert Temporally Evolving case followed closely by the Inert Isotropic case. In comparison, the Inert Spatially Evolving case displays larger scalar differences, which become slightly smaller as the flow is traversed in the stream-wise direction. The scalar differences are by far the largest in the temperature fields of the reacting cases in the upstream regions. $\Delta T_{\rm m}/\Delta T_{\rm max}$ decreases for both reacting cases significantly from the upstream to the downstream region. Thereby, $\Delta T_{\rm m}/\Delta T_{\rm max}$ of the downstream region Low Re Flame almost equals that of the upstream region High Re case.

An important characteristic of the statistics of the separation length, is its invariance toward changes in Reynolds numbers when normalized with the mean length $\ell^* = \ell/\ell_m$ [127] [108] [53]. The probability density functions (PDF)

of the normalized separation length $P(\ell^*)$ are shown in Fig. [6.5] in linear and linear logarithmic scale. Figure. [6.5] shows the PDF of the normalized DE length for the three Inert cases. For the short elements, a linear increase of the PDFs is observed. This linear increase is due to the diffusive drift of the extremal points, which causes the annihilation of DEs due to the merging of extremal points which are in close proximity of each other Wang and Peters [127]. For these short elements, the PDFs show a perfect collapse.

After a maximum, an exponential decrease of the PDF for longer DEs is observed, which is attributed to the cutting and connecting of the DEs by turbulent eddies [127]. The exponential decrease of $P(\ell^*)$ is highlighted in Fig. 6.5b) by the linear logarithmic scale. The motion of turbulent eddies introduces new extremal points into the scalar fields altering the DE structure, effectively cutting a DE. If the probability of the occurrence of the turbulenceinduced extremal point in the DE structure is independent of the location within the DE, $P(\ell^*)$ will decrease exponentially for large ℓ^* . The slope of the PDF in this representation indicates the cutting frequency, an inverse of an eddy turnover time [124]. As previously observed, the Inert Isotropic case displays the exponential decrease. This is expected, as the isotropic nature of the case implies an eddy turnover time independent of the location and, consequently, a constant cutting frequency. However, the exponential decrease is also present in the PDFs of the Inert Temporally Evolving case and Inert Spatially Evolving case, with one and two statistically inhomogeneous directions, respectively. The slope of the exponential decrease of $P(\ell^*)$ is approximately the same for all Inert cases, resulting in a collapse of the PDFs in the range of scales dominated by random cutting and connecting range. Only in the tails of the PDFs, small differences can be observed. The Inert Isotropic case displays a range of normalized length scales comparable to that of the Spatially Evolving case. The greatest separation of scales is seen in the Inert Temporally Evolving case.

The PDFs for all spatially evolving cases for the upstream regions and downstream regions are shown in Figs. 6.5c) and d). Again, the characteristic linear increase in the PDFs for the diffusive drift range is observed for the reacting and inert cases alike. The only difference in the characteristic shape of the PDFs is found in the upstream region of the spatially evolving cases. Here, the PDF of the Low Re Flame differs. While the PDFs of the Intermediate Re Flame and the Non-Reactive collapse, an additional local maximum in the Low Re Flame PDF is situated at $\ell^* \approx 1.6$. This second maximum is a signature of a length scale induced at the nozzle that has not been sufficiently mixed out at this streamwise location due to the limited level of turbulence

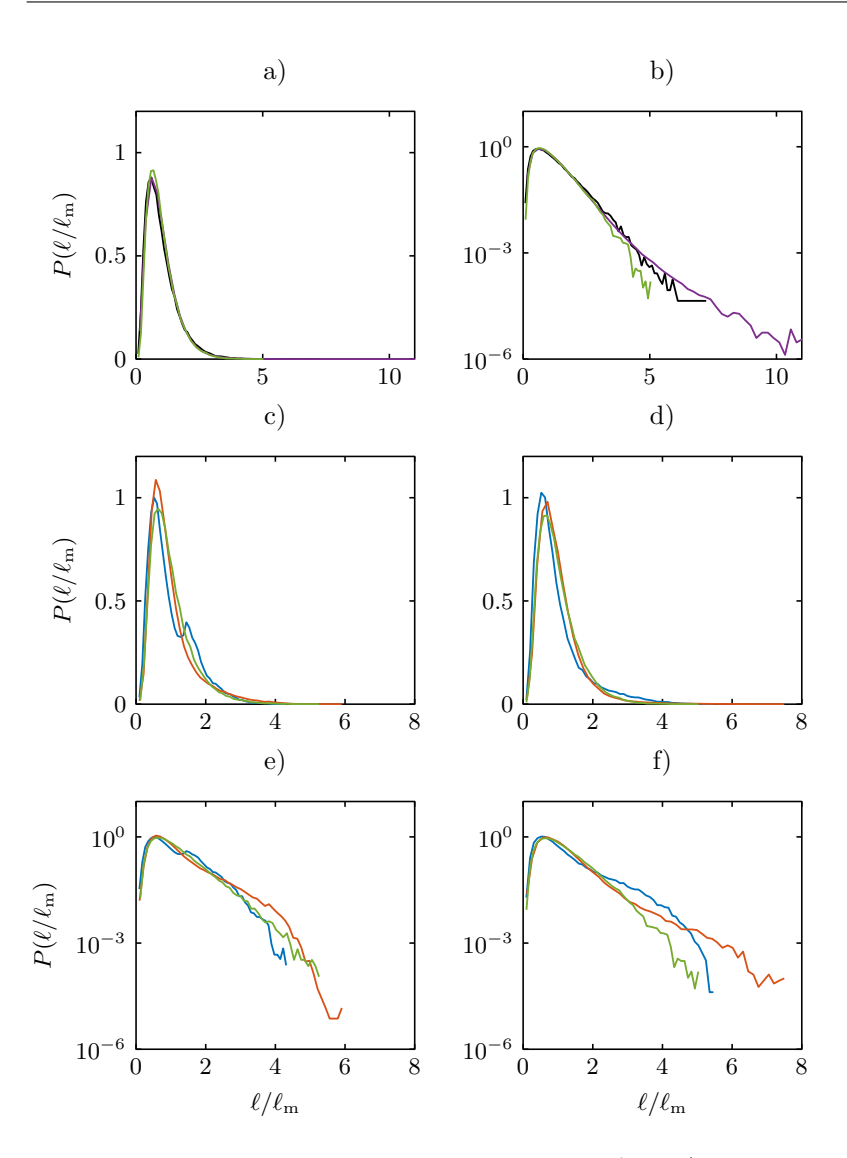


Figure 6.5: PDFs of normalized separation length $\ell^* = \ell/\ell_{\rm m}$. Low Re Flame (blue), Intermediate Re Flame (Red), Inert Spatially Evolving case (green). The black line corresponds to the Inert Isotropic case and the purple to the Inert Temporally Evolving case. a) and b): Inert Spatially Evolving case in the downstream region, Inert Temporally Evolving case and Inert Isotropic case in linear and linear logarithmic scales. c) and d): Upstream region and downstream region of the spatially evolving jet cases in linear scales. e) and f): Upstream region and downstream region of the spatially evolving jet cases plotted with semilogarithmic scales.

87

in this case. In the PDFs at the downstream region in Fig. [6.5] this initial length scale in the PDF was mixed out and the PDF took the expected form. Even though the Low Re and the Inert Spatially Evolving case share the same initial Reynolds number, the absence of the local maximum in the upstream region of the Spatially Evolving case is indicative of the fact that the passive scalar reaches an equilibrium in the length scale distribution further upstream of the nozzle, or in a temporal sense, faster than a reacting scalar, such as the temperature.

Figs. 6.5e) and f) show the same PDFs in a linear logarithmic scale for the upstream and downstream regions, respectively. This representation highlights two distinctive characteristics. First, it shows the increasing scale separation due to increasing Reynolds number. While the PDFs agree well for the short DEs, the differences in the tails of the PDFs (long elements) are apparent. The intermediate Re Flame displays the longest normalized DEs in both regions, while the Low Re Flame displays the smallest separation of length scales in the upstream position and the Inert Spatially Evolving case in the downstream regions. While the PDF of the Non-Reactive case shows hardly any difference in the two investigated region, the reacting cases show a significantly wider separation of scales in the downstream region. The non-reactive case displays an almost perfectly constant slope in both regions. The reactive cases show a constant slope for intermediate length comparable to the one observed in the Spatially Evolving case. For large ℓ^* , the discrepancy from the constant slope in the PDF can be explained by DEs that reach less turbulent regions where the cutting frequency is reduced due to heat release and higher viscosity and can, therefore, be attributed to low Revnolds number effects.

The invariance of the normalized DE length statistics toward changes in Reynolds numbers previously first observed by Wang and Peters [127] holds for the premixed flames. However, the same characteristic shape of the PDFs of normalized length scales in the reacting scalars is surprising. Traditional methods of obtaining turbulent scales in reacting flows, such as spectra and structure functions, cannot be utilized to their fullest potential to generate equivocal results regarding the effect, or lack thereof, of combustion on turbulent scales due to the inherent high anisotropy and high intermittency of the investigated reacting flows.

6.1.2 Joint Statistics

The second parameter characterizing DEs is the passive scalar difference $\Delta \phi$ in the Spatial Evolving cases and ΔT in the premixed reacting cases. Its

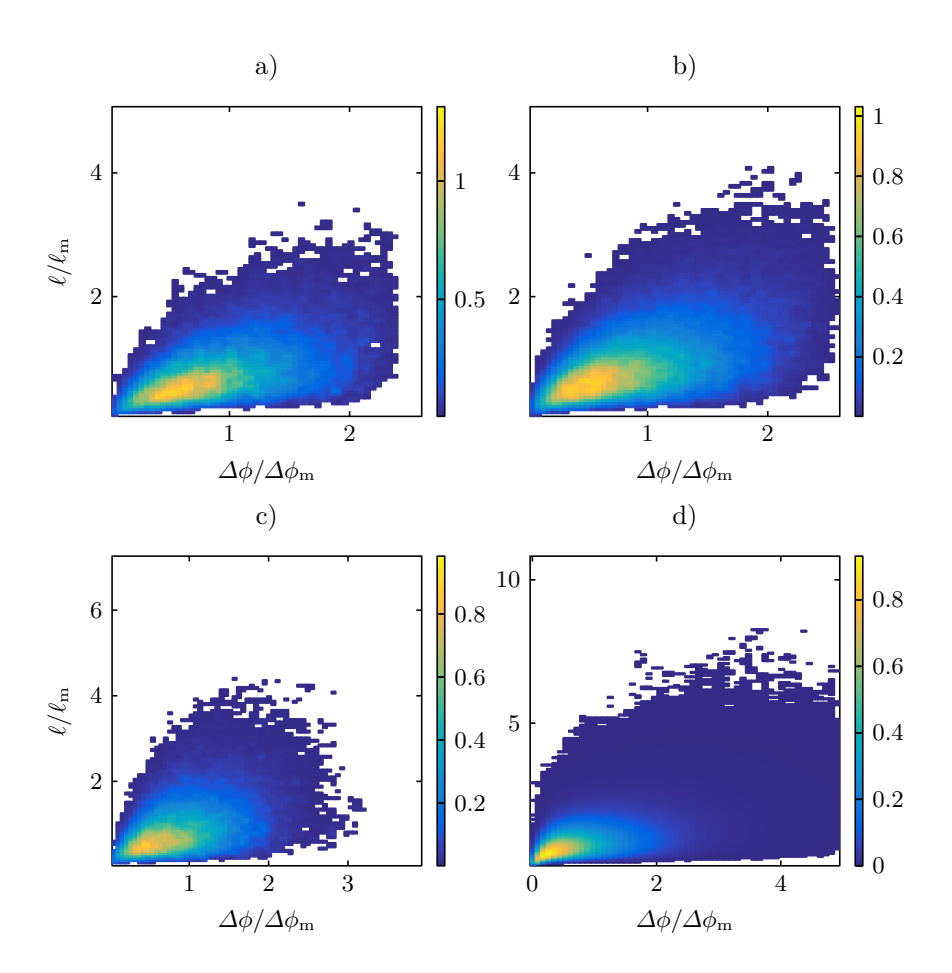


Figure 6.6: JPDFs of the normalized separation length normalized scalar difference $P(\Delta\phi^*, \ell^*)$. a): Spatially Evolving case upstream region. b): Spatially Evolving case downstream region. c): Inert Isotropic turbulence. d): Inert Temporally Evolving case.

analysis is performed by means of the JPDF of the normalized DE length ℓ^* and the normalized scalar difference $\Delta\phi^*$, $P(\Delta\phi^*, \ell^*)$. The JPDFs are shown for the Spatially Evolving case for both the upstream and downstream regions in Figs. 6.6a) and b). The maximum of the probability density is located in the bottom left corners for small values of ℓ^* and $\Delta \phi^*$. This region is characterized by the annihilation of short DEs due to the effect of the drift of extremal points. In the center of the JPDFs, the region dominated by the random cutting and reconnection of the DEs by turbulent eddies can be observed. The bottom right corner region characterized by short elements and large scalar differences corresponds to the so-called 'cliff' structures in scalar fields, cf. [2], [65]. These DEs characterize regions of high scalar gradients followed by a gradual descent. The overall shapes of the JPDF in the two stream-wise regions agree well. In addition to the increasing separation in length scales from the upstream to the downstream region, already observed in the marginal statistics in Figs. [6.5c] and d), the range of the values of the normalized scalar difference increases as the flow is traversed in the streamwise direction. The JPDF of the Inert Isotropic case in Fig. 6.6c) qualitatively shows the same shape as the one obtained from the Spatially Evolving case with a dominant maximum for small ℓ^* and $\Delta \phi^*$ in the drift region. Only a slight difference for intermediate ℓ^* and small $\Delta\phi^*$ can be observed, where the Inert Isotropic case shows a higher probability density. While the range of length scale values is similar, the Inert Isotropic case JPDF displays a larger range of values of $\Delta \phi^*$. Just as with the length scale separation in Figure 6.5f), the Inert Temporally Evolving case shows the largest range of values for $\Delta \phi^*$.

The normalization of DE parameters in the JPDF is also defined in a different fashion in order to compare DE scales with the characteristic flame thickness. In Fig. 6.7, the normalization of ℓ is performed with the laminar flame thickness $\delta_{\rm L}$ (based on the temperature gradient) to achieve the originally proposed comparison of turbulent and flame scales $\ell' = \ell/\delta_{\rm L}$. The DE temperature difference is normalized with the temperature difference of the burned and unburned mixtures $\Delta T' = \Delta T/(T_{\rm b} - T_{\rm u})$. The maximum normalized value of $\Delta T' = 1$ corresponds to a DE whose gradient trajectories cross all the way from the unburned, through the premixed flame front to the fully burned. In Figs. 6.7a) and b), the normalized JPDFs in the upstream region of the Low Re Flame and the Intermediate Re Flame are shown. For both cases, the maximum of the probability density is located in the right bottom corner for large $\Delta T'$ and small ℓ' , placing large volumes of the flow in the 'cliff' structure regime. This 'cliff' structure is imposed by the premixed

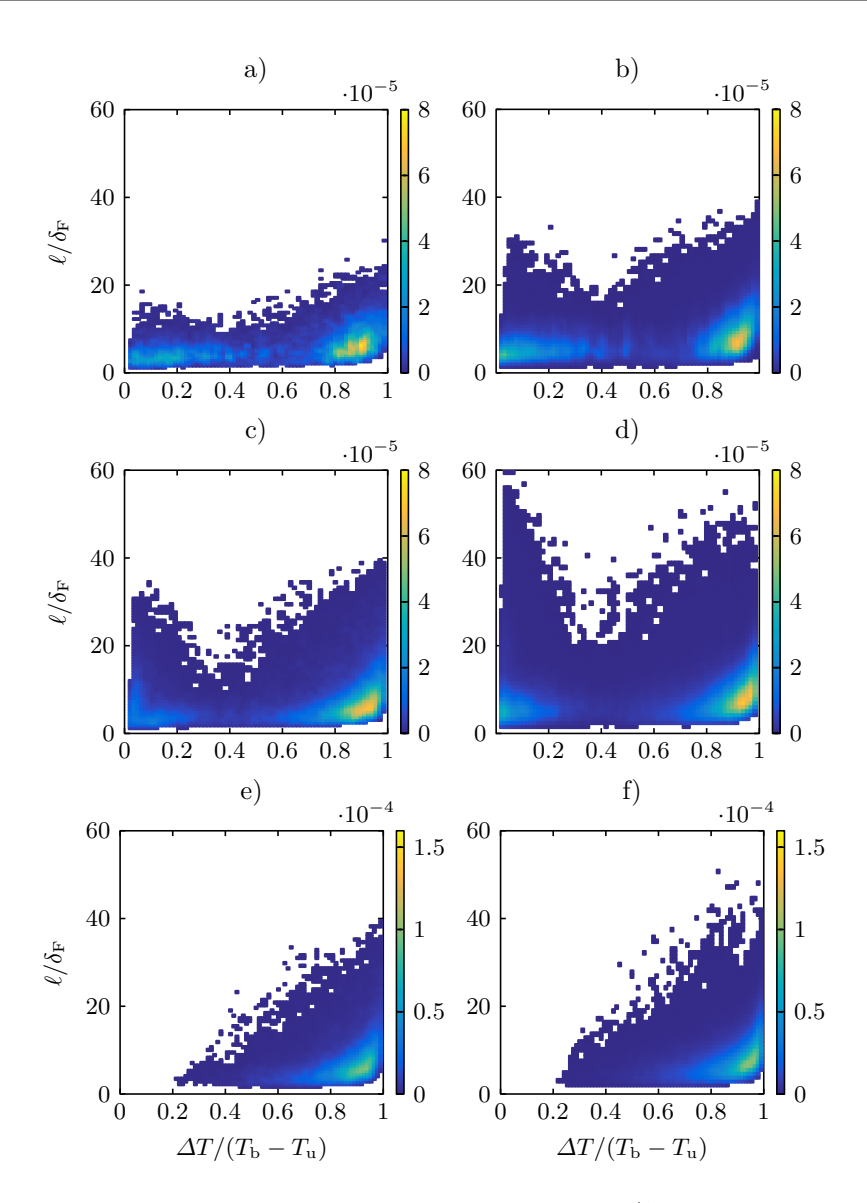


Figure 6.7: JPDFs of the normalized separation length $\ell/\delta_{\rm F}$ and the normalized scalar difference $\Delta T/(T_{\rm b}-T_{\rm u})$. a): Low Re Flame upstream region. b): Intermediate Re Flame upstream region. c): Low Re Flame downstream region. d): Intermediate Re Flame downstream region conditioned on reacting DEs. f): Intermediate Re Flame downstream region conditioned on reacting DEs.

flame structure on the temperature field, which cannot be fully mixed out by turbulent mixing and results in distinctly different shape of the JPDF as compared to the Spatially Evolving cases in Figure 6.6 Further, a local maximum is found in the diffusive drift region for small $\Delta T'$ and small ℓ' where approximately the global maximum is found for the Spatially Evolving cases. For scalar differences $\Delta T < 0.5$, the JPDFs resemble vaguely those of the non-reacting cases.

The small length scales remain constant while the integral scales increase with the Reynolds number, as intended in the configuration. The assumption of the regime of the "thin reaction zone" is reflected by the JPDFs as, while being on average larger than the flame thickness $\delta_{\rm m}$, the vast majority of the DEs are of a comparable length to the flame thickness. While not reaching all the way from the unburned to the burned, the flame structure remains largely intact with high probabilities of traversing large temperature differences before turbulence induced extremal points interrupting the laminar flame structure. This is highly consistent with the conditions of the "thin reaction zones" where turbulent mixing interferes with the preheating zone dynamics while leaving the inner reaction zone unaffected, cf. Peters [95]. The JPDFs of the downstream region of the two reacting cases are shown in Figs. [6.7c] and d). Again, a noticeable change in the stream-wise direction can be observed for both cases. While qualitatively resembling the JPDF of the upstream region, the JPDFs show a clear increase in length scales, as well as a further concentration of probability density in the global and local maximum.

In Figs. 6.7e) and f), the JPDF in the downstream region of the Low Re and Intermediate Re Flame is conditioned on DEs which cross the flame front, omitting all non-reactive DEs from the statistics. The absence of the local maximum for small $\Delta T'$ and small ℓ' further indicates that this region corresponds to the core of the jet flow, as the similarity with the shape of the Spatially Evolving cases in Fig. 6.6 already suggested. Both conditioned JPDFs look strikingly similar with regard to the range of values of the two DE parameters.

A similar conditioning of the DE statistics in reacting flows was applied to the JPDF of the mixture fraction field in a non-premixed jet in Gauding et al. $\boxed{58}$, where only DEs crossing the iso-surface of the stoichiometric mixture Z where retained in the statistics. While the scalar difference ΔZ was higher in the reacting region of the non-premixed and ramp structures more probable, it was shown that this is caused by poor mixing in these regions. A drastic change in the shape of the JPDF with a clear imprint of the flame front, as displayed in Fig. $\boxed{6.7}$, was not observed.

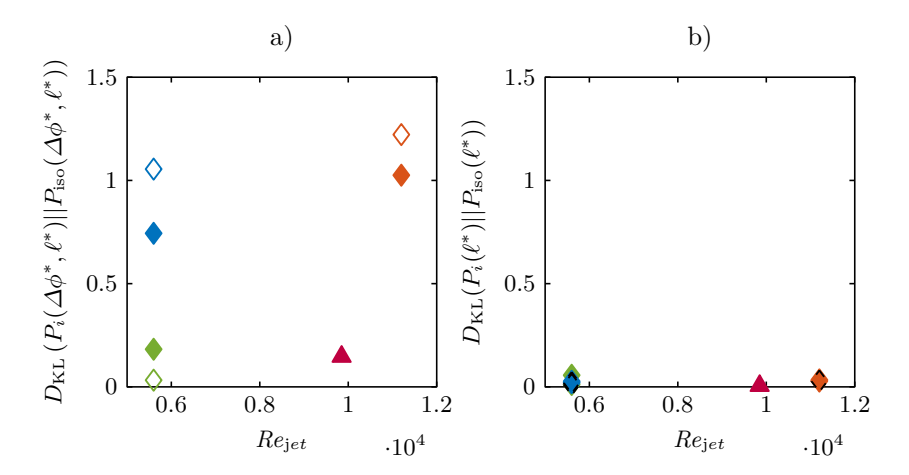


Figure 6.8: Kullback-Leibler divergence of the JPDFs of the normalized DE parameters of the various cases with reference to the JPDF obtained from the Inert Isotropic case. b): Kullback-Leibler divergence of the marginal PDFs of the normalized DE length with reference to the Inert Isotropic case. The blue, red, and green diamonds correspond to the Low Re Flame, Intermediate Re Flame, and Spatially Evolving case, respectively. The solid symbols indicate the upstream region; the hollow and black dashed symbols indicate the downstream region. The Inert Temporally Evolving case is indicated by the solid purple triangle.

To achieve a quantitative comparison of the joint statistics of the normalized DE parameter statistics, the Kullback-Leibler divergence $D_{\rm KL}$ [77] was computed. The Kullback-Leibler divergence, applied to the joint statistics in this study, measures the logarithmic difference between the two JPDF of the normalized DE parameters $P_1(\Delta\phi^*, \ell^*)$ and $P_2(\Delta\phi^*, \ell^*)$ with reference to the latter and is defined as

$$D_{\mathrm{KL}}(P_1||P_2) = \int_{0}^{\infty} \int P_1(\Delta\phi^*, \ell^*) \log \frac{P_2(\Delta\phi^*, \ell^*)}{P_1(\Delta\phi^*, \ell^*)} d\Delta\phi^* d\ell^*, \qquad (6.1)$$

where two identical JPDF $P_1 = p_2$ would yield $D_{KL}(P_1||P_2) = 0$ The Kullback?Leibler divergence between the Inert Isotropic case and the various other cases is shown in Fig. 6.8a). As expected from Fig. 6.6, the Kullback-Leibler divergence yields low values for the non-reacting cases indicating good agreement between the JPDFs and the JPDF of the Inert Isotropic case. For the Spatially Evolving case, the divergence decreases from the upstream to the downstream region, becoming almost identical to that of the isotropic turbulence. The premixed reacting cases show $D_{\rm KL}(P_1||P_{\rm iso})$ values at least an order of magnitude higher. Here, the trend with regard to the spatial change is reversed as the divergence increases from the upstream to the downstream region. As a point of reference, the Kullback-Leibler divergences of the marginal PDF of the DE length is shown in Fig. [6.8b). $D_{\rm KL}$ shows very low values for the marginal PDFs, regardless of the reactive or non-reactive nature of the case or stream-wise region. This further points to the DE scalar difference, which is almost exclusively affected by changes in configuration or the reactive nature of the scalar, while the normalized length scales remain unchanged.

The Kullback-Leibler divergence of the JPDFs of the upstream and down-stream regions of the spatially evolving cases yields values of $0.1 < D_{\rm KL}(P_{i,,{\rm downstream}}||P_{i,{\rm upstream}}) < 0.2$ regardless of the reacting or non-reacting nature of the configuration, which indicates that the change in joint statistics is significantly more influenced by the reactive nature of the flames than the stream-wise region.

Finally, the normalized mean DE scalar difference conditioned on the normalized DE length $\langle \Delta \phi^* | \ell^* \rangle$ and $\langle \Delta T^* | \ell^* \rangle$ is investigated in Fig. 6.9. This conditional mean resembles a conditioned first-order moment of the respective scalar fields. For isotropic turbulence $\langle \Delta \phi^* | \ell^* \rangle$ was found to scale with Kolmogorov's 1/3 power law, cf. Wang and Peters 127 and Wang 125. This scaling is reproduced with the Inert Isotropic case, which follows the

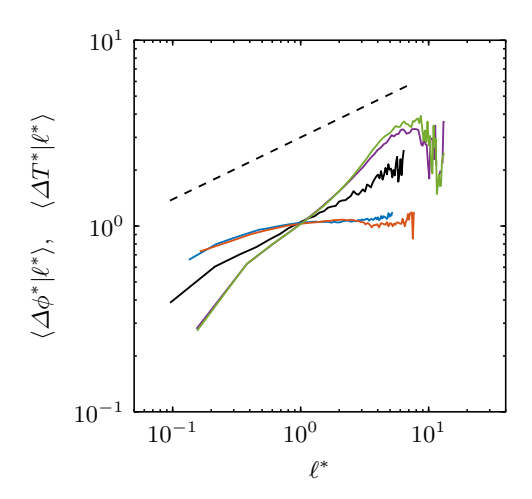


Figure 6.9: Normalized mean DE scalar difference conditioned on the normalized DE length. The blue, red, and green lines indicate the Low Re Flame, Intermediate Re Flame, and Spatially Evolving case, respectively. The black line corresponds to the Inert Isotropic turbulence and the purple line to the Inert Temporally Evolving case. The dashed black line indicates Kolmogorov's 1/3 power law scaling.

scaling indicated by the dashed black line for large and intermediate lengths. The Inert Spatially Evolving case and the Inert Temporally Evolving case both show a clear scaling of $\langle \Delta \phi^* | \ell^* \rangle$ as well. However, this scaling is with an exponent of approximately 2/3, twice as high as the one obtained from the Inert Isotropic case. The perfect collapse of the two means in combination with the similarities of the JPDFs in Fig. 6.6 seems to indicate that the differences between DE statistics of the spatial or temporal configuration is negligible. The difference in the scaling exponent can be attributed to the mean shear present in these flow configurations, which is absent in the Inert Isotropic case. The conditional means of the Low Re Flame and the Intermediate Re Flame collapse perfectly for the short and intermediate separation distances. Differences can only be observed for the large elements. However, both reacting cases display only a scaling for short elements, which ceases for DEs $\ell^* > 1$. For longer elements, the two DE parameters are uncorrelated.

6.2 Gradient Trajectory Analysis of the Burning Rate in Turbulent Premixed Jet Flames

The fundamental impact of turbulence on the flame speed in premixed flames is twofold and varies by the degree of overlap between the turbulence and the flame time and spatial scales. The overall rate of fuel consumption can increase due to the turbulently increased flame surface and the direct influence of fine scale turbulent mixing on the flame structure. The degree of interaction can be categorized by combustion regimes which are summarized in the "Borghi-Peters" diagram [95] introduced in Chapter [2.2.1] If the size of the smallest turbulent scales, characterized by the Kolmogorov scale η , significantly exceeds the flame thickness $\delta_{\rm L}$, the increase of the flame speed due to turbulence is entirely related to the increase in the flame surface area. However, for $\eta < \delta_{\rm L}$, the first mechanism is superimposed on the second and modifications to the flame speed might be related to modifications of the imbalance between diffusion and reaction in the flame layers.

This combustion regime has been investigated in a number of experimental and numerical works 45, 4, 102, 122, 61, 32, 44, 111, 31, 30. In addition, the dataset used in the present paper was used by Luca et al. 83 and Antonio et al. 3 to study the effects of an increase of the integral scale in the thin reaction zone regime. In particular, Luca et al. 83 focused on the mechanisms of flame surface production and destruction, while Antonio et al. 3 concluded that the observed enhanced turbulent flame speed could not be fully attributed

to the increase in flame surface, but a thickening of the inner reaction zone led to an additional increase in fuel consumption as well. Consequently, the flame speed depends to a significant degree on the local structure of the premixed flame which is analysed in detail in the present paper. In particular, the combustion process is investigated along gradient trajectories and the balance between the effects of turbulence on the local reaction rates and on the topology of the reactive scalar fields is assessed.

While traditional one-point statistics evaluated at the flame surface perform well in the context of very small flame thicknesses $\eta \gg \delta_{\rm L}$, difficulties might arise when the entire flame structure, characterized by a finite significant thickness compared to the turbulence scale, needs to be analyzed. To overcome this challenge faced in the thin reaction zones regime, a method of obtaining statistics in a meaningful frame of reference is required, which additionally takes the entire local flame structure into account.

DEs can be described by two parameters, namely the Euclidean distance between their extremal points ℓ and the scalar difference in these points $\Delta \phi$. This parameterization helps to significantly decrease the complexity of the complicated local scalar structure and enables an intuitive analysis. In addition, statistics of quantities of interest, such as gradients and reaction rates, can be conditioned on the dissipation element parameters, providing a link between the combustion process in the flame and the multi-scale structure of the turbulent flow field.

In this work, the DE analysis is applied to the temperature fields of three premixed flame DNS cases. Since the temperature can be interpreted as a progress variable C in the context of premixed combustion, the gradient trajectories used in forming a DE can be interpreted as the three-dimensional physical coordinates a flamelet solution occupies in physical space. Then, DEs can be regarded as groups of flamelets, which share the same start and end points in space and the same temperature at the extremal points. In addition to using the DE length ℓ to achieve the traditional comparison of turbulent length scales and flame scales not only globally but also locally, the DE scalar difference ΔT provides additional insight as well. As premixed flames are structures which are dominated by the imbalance of diffusive transport and reactions, a turbulence induced extremal point in the progress variable field represents a forceful end to this structure as any diffusive flux in an extremal point is by definition $J = -D_C \nabla C = 0$. Therefore, ΔT represents the maximum distance in temperature space over which a diffusively dominated flame structure can exist before being terminated by turbulent advection.

First, the gradient trajectories of the temperature field are investigated in

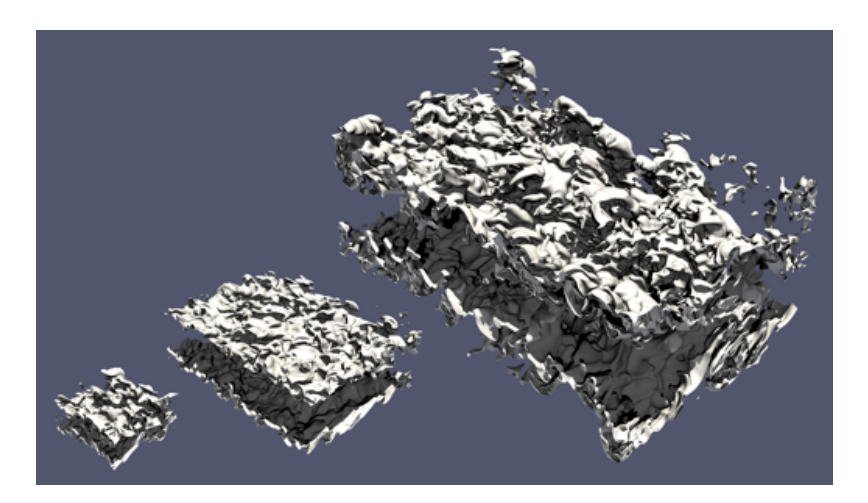


Figure 6.10: The $T=1800\mathrm{K}$ iso-surface in the stream-wise regions investigated. The stream-wise direction of the flow is from bottom-left to top-right. The Low Re case, Intermediate case Re, and High Re case are shown from left to right.

detail and the impact of the DE parameters on the structure of the temperature field surrounding the flame front is investigated. Second, the correlation of meaningful reacting scalars and source terms with the DE parameters are investigated. A detailed examination of the reacting scalar structure in the preheating and inner reacting zone is conducted and directly compared to a laminar flamelet and a flamelet model utilizing the temperature as the progress variable. Finally, the implications of the alterations to the flame structure due to turbulence are quantified and related to the flame speed of the entire local flame topology.

6.2.1 Flame Structure Analysis

To evaluate the impact of the various turbulent scales on the flame structure, the focus lies on gradient trajectories and DEs crossing the flame front. The flame front is defined here as the temperature iso-surface of $T_{\rm ff}=1800{\rm K}$, which constitutes the temperature of the maximum heat release in the laminar flamelet solution matching the boundary conditions of the DNS cases. The following analysis is performed for all three cases at the stream-wise position $x/l_{\rm F}=0.6$, where $l_{\rm F}$ is the mean flame length. At this stream-wise location,

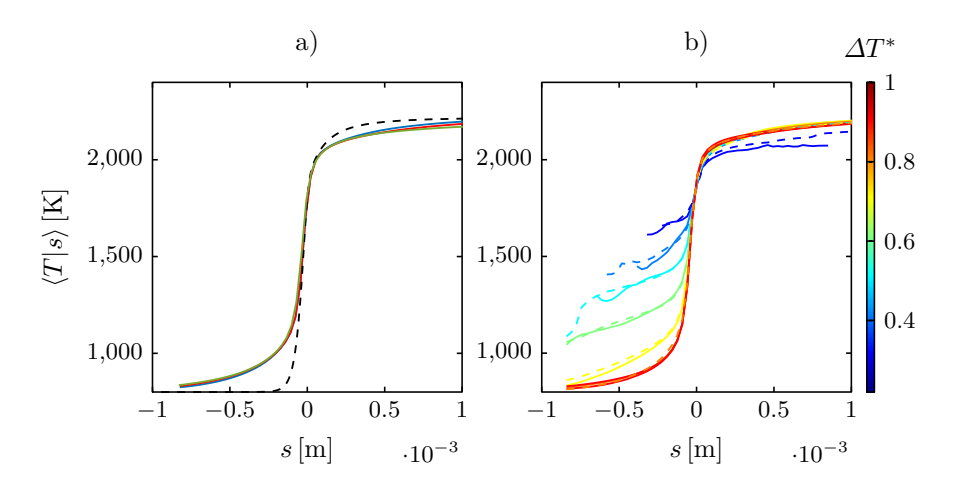


Figure 6.11: a): Mean temperature conditioned on the arc-length distance to the flame surface for (—): the Low Re case, (—): the Intermediate Re case and (—): the High Re case. The black dashed line indicates the laminar flamelet solution. b) Mean temperature additionally conditioned on the normalized scalar difference. The solid and the dashed lines correspond to the Low Re case and the intermediate Re case, respectively.

the flame and turbulence are fully developed. The steam-wise extend of the investigated section for all three cases is 2H. The highly turbulent nature of the combustion is illustrated by the iso-surface of $T=1800\mathrm{K}$, corresponding to the peak heat release and fuel consumption rate in the one dimensional planar flame, shown in Fig. $\boxed{6.10}$ for the investigated stream-wise position in the three cases.

As the tracing of gradient trajectories can be interpreted as moving in the normal direction from each scalar iso-surface to the next, gradient trajectories represent the shortest possible path through the flame structure. This can be exploited to compare an otherwise highly complex and convoluted three-dimensional flame structure to a one-dimensional object such as the flamelet. To this end, the mean temperature $\langle T \rangle$, conditioned on the arc-length distance s of the gradient trajectories starting at the flame surface, is shown for the three cases in Fig. [6.11] a). Negative values s < 0 correspond to the preheating zone of the flame, while positive values s > 0 indicate the arc-length distance traveled from the flame front into the oxidation zone. Compared to the

laminar flamelet, all three DNS cases display the temperature structure expected in the thin reaction zones regime. In the preheating zone, $\langle T \rangle$ is clearly elevated above the flamelet values indicating a thickening due to the turbulent transport of heat characteristic for this regime. On the contrary, the conditional mean $\langle T \rangle$ is close to the laminar flamelet solution, for $s \approx 0$. Finally, the mean temperature in the oxidation layer stays below that of the flamelet solution but converges to it for large s. With this global statistics, only a slight influence of the Reynolds number can be observed. In Fig. [6.11] b), the mean temperature is additionally conditioned on the normalized DE scalar difference $\Delta T^* = \Delta T/(T_b - T_u)$. Values of $\Delta T^* \approx 1$ represent DEs spanning from the burned to the unburned regions while $\Delta T^* \approx 0$ indicates DEs that terminate in extremal points at temperatures close to T = 1800K. It can be observed that ΔT^* is clearly linked to an increased temperature in the preheating zone for a given arc-length distance from the flame, which correspond to a local thickening of the flame structure. For small ΔT^* , the oxidation zone is notably affected as well. Another important effect observed is the decrease of the gradients of the mean temperature close to the flame front.

The effect is not limited to the mean temperature. The joint probability density function (JPDF) of the normalized temperature gradient $\nabla T^* =$ $\nabla T/\nabla T_{\rm fl}(1800{\rm K})$, with $\nabla T_{\rm fl}(1800{\rm K})$ being the temperature gradient of the unperturbed laminar flame, and the normalized arc-length distance $s^* = s/\delta_{\rm F}$ is shown in Fig. 6.12. Additionally, the JPDF $P(s^*, \nabla T^*)$ is conditioned on being part of dissipation elements with large scalar differences ($\Delta T^* > 0.8$), intermediate scalar differences (0.8 > ΔT^* > 0.3) and small scalar differences $(0.3 > \Delta T^*)$. For the large scalar differences, the regions of high probability density are situated around the laminar flamelet solution. Small differences can only be observed in the preheating regions. However, for the intermediate and the small scalar differences, the probability of reaching the values of $\nabla T_{\rm fl}$ in the inner reaction is close to zero. This indicates that, for all but the largest scalar differences, the entire temperature gradient structure in the inner reaction zone is altered and significantly lower gradients are present locally. In addition, the analysis show that the lower gradients in the inner reaction layer are linked to the presence of extremal points, i.e., a temperature minimum in the preheat zone side and/or a temperature maximum in the oxidation side of the flame, relatively close to the flame surface, therefore to the interruption of the flamelet structure by turbulence and not by the thickening of the entire flamelet itself.

The implications of the findings of Figs. 6.11 and 6.12 for the local structure

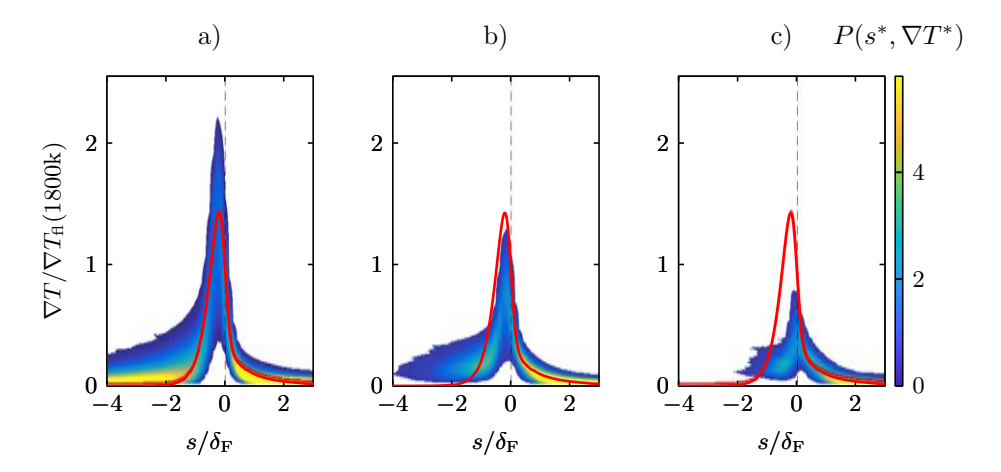


Figure 6.12: JPDF of the normalized temperature gradient $\nabla T/\nabla T_{\rm fl}(1800{\rm K})$ and the normalized arc-length distance $s/\delta_{\rm F}$ in the High Re case conditioned on the normalized scalar difference ΔT^* . a): large scalar difference DEs ($\Delta T^* > 0.8$), b): intermediate scalar difference DEs ($0.8 > \Delta T^* > 0.3$) and c) small scalar difference DEs ($0.3 > \Delta T^*$). The red line indicates the laminar flamelet solution.

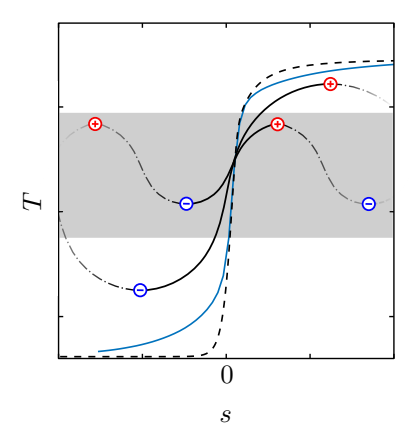


Figure 6.13: Schematic illustration of the impact of the scalar structure as indicated by DEs. The solid black lines indicate exemplary gradient trajectories of DEs. The black dash-dotted lines represent possible adjacent gradient trajectories. The grey region indicates temperature regions of high heat release. The encircled red plus and blue minus signs indicate the maxima and minima, respectively. The solid blue line and the dashed black line are the conditional mean temperature and the flamelet, already shown Fig. [6.11]

of the flame front and potential consequences for the flame speed are illustrated in Fig. [6.13]. The introduction of extremal points close to the flame front leads to a decrease in the temperature gradients. Consequently, the gradient trajectories traverse regions of high heat release for a longer distance. If ΔT^* is low enough, not only the preheat zone is significantly thickened but the inner reaction zone as well. As shown by Antonio et al. [3] for the same DNS dataset, the thickened reaction zone contributes to an increased consumption of fuel and therefore an increase in flame speed. The present analysis links the thickening to the penetration of turbulent eddies, and to the introduction of extremal points, near and inside the inner reaction layer.

A second observation is linked to the nature of extremal points. By definition, the temperature in the immediate vicinity of these points will only rise, for a minimum, or fall for a maximum. Therefore, for a gradient trajectory that crosses the flame surface and is fully contained in the reaction zone, like the shortest black solid line in Fig. [6.13] the adjacent trajectories will also fall inside the reaction zone (dash-dotted lines in the figure), contributing again to the thickening of the reaction layer. For the case of very small ΔT^* , when the extremal points are exclusively situated in the inner reaction zone, the local topology actually resembles that of the broken reaction-zone regime.

6.2.2 Correlation between Reacting Scalars and DE Parameters

While the DE scalar difference of ΔT is linked to the thickening of the temperature profile across the flame front, the second DE parameter, the length ℓ , can be employed to gain additional insight in the local flame structure. To compare the turbulent length scales and the flame scales, the local value of ℓ is compared to an adequate length scale provided by a laminar one-dimensional laminar flame (flamelet) at the same condition of the DNS. The local flamelet length scale is defined as

$$\ell_{\rm fl} = |s_{\rm fl}(T_{\rm max}) - s_{\rm fl}(T_{\rm min})|,$$
(6.2)

with $s_{\rm fl}(T_{\rm max})$ and $s_{\rm fl}(T_{\rm min})$ being the physical coordinates of the laminar flamelet where the temperatures match those in the minimum and the maximum of the DE, respectively. Consequently, $\ell > \ell_{\rm fl}$ indicates a thickened section of the flame and $\ell < \ell_{\rm fl}$ a compressed section steeper than a laminar flamelet solution. The JPDF of the normalized DE parameter $\ell^* = \ell/\ell_{\rm fl}$ and ΔT^* is shown in Fig. 6.14 The JPDF is weighted with the intersection area of the individual DEs and the flame front. As expected from the universality of the normalized DE length statistics 41, the ℓ^* distribution is very similar.

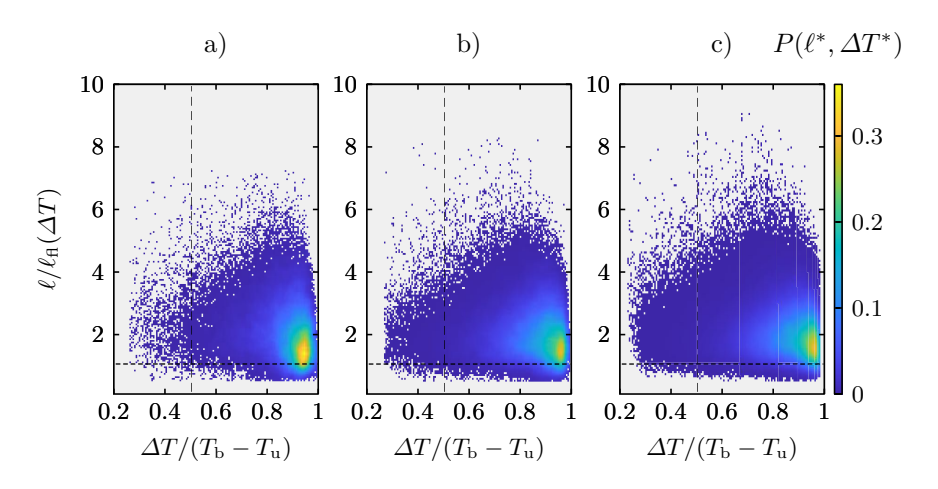


Figure 6.14: JPDF of the normalized DE parameters ΔT^* and $\ell^* = \ell/\ell_{\rm fl}(\Delta T)$ weighted with the intersection area of the individual DE and the flame surface. a): The Low Re case, b): the Intermediate Re case and c): the High Re case.

It can be observed that the probability of encountering thickened regions is higher than that of turbulently compressed regions. The most substantial difference of $P(\ell^*, \Delta T^*)$ between the cases lies in the increasing probability density of small ΔT^* with increasing Reynolds number.

To evaluate the influence of the DE parameters on other important reacting scalars besides the temperature close to the flame front, the mean mass fractions $\langle Y_{\alpha} \rangle$ of selected species are conditioned on the temperature of their respective maximum value in the laminar flamelet max $Y_{\alpha,\mathrm{fl}}$ and the previously introduced normalized DE parameters ℓ^* and ΔT^* . The conditional mean is shown for O and OH, two species which exist on very short time scales due to their high reactivity, in Figs. [6.15a) and b). A clear correlation with ℓ^* can be observed with values lower than the laminar flamelet for $\ell^* < 1$. However, the maximum joint probability of ℓ^* and ΔT^* are situated in regions of $\langle Y_{\alpha}^* \rangle \approx 1$, which explains the good agreement of the DNS data with the flamelet model reported by Antonio et al. [3]. The influence of ΔT^* is small for O and OH. However, for species which are formed in the inner reaction zone and exist on longer time scales, such as CO, the scalar difference has a distinct influence in the conditional mean mass fraction, as seen in Fig. [6.15c). These observations are indicative of a limited impact of the thickened flame structure on the

combustion chemistry.

Analogous to the conditioned normalized mass fraction, the methane source term $\langle \dot{\omega}_{\text{CH}_4}^* \rangle = \langle \dot{\omega}_{\text{CH}_4} \rangle / \min \dot{\omega}_{\text{CH}_4,\text{fl}}$ is conditioned on the normalized DE parameters in Fig. [6.15d). This quantity is important because its volume integral is proportional to the turbulent flame speed [95]. While being slightly lower than the laminar flamelet value, $\dot{\omega}_{\text{CH}_4}$ is significantly affected for very low values of ΔT^* and very large values of ℓ^* .

While the mean temperature conditioned on the arc-length distance to the flame front in Fig. [6.11] revealed that the temperature profile is thickened with decreasing ΔT^* , it remains unclear if the profiles of other reacting scalars are thickened to the same degree. To not limit the investigation to a single iso-surface and take full advantage of the gradient trajectories, selected mean quantities are conditioned on the arc-length distance to the flame front s and the scalar difference ΔT^* . This is analogous to the procedure for mean temperature $\langle T|s, \Delta T^*\rangle$.

In experiments, formaldehyde $\mathrm{CH_2O}$ is often used to identify the preheat zone [13] [111] [44]. $\langle Y_{\mathrm{CH_2O}}|s,\Delta T^*\rangle$ is shown in Fig. [6.16a). The conditional mean shows the clear increase in the preheat zone with decreasing ΔT^* , highlighting the significant thickening of the preheat zone. In Fig. [6.16b), $\langle Y_O|s,\Delta T^*\rangle$ is shown, as this species usually does not exist in the preheat zone. For $\Delta T^*<0.4$, significant values of the $\langle Y_O\rangle$ are observed several δ_F ahead of the flame. From this, it can be concluded that even species which are not observed in the preheat zone of the laminar flame are transported from the inner reactive layer to the preheat zone by turbulence. In addition, it is observed that in the oxidation layer, the oxygen radical requires a long distance to converge to the flamelet value, regardless of the conditioning with respect to ΔT^* .

The mean mass fraction of O is conditioned on s and ℓ^* in Fig. 6.16c). This figure demonstrates that ℓ^* is not linked to the flame thickening in the preheat zone. However, it can be observed that for $\ell > 9\ell_{\rm fl}$, i.e., the local turbulent scales being almost an order of magnitude larger than the flame scale, the $\langle O \rangle$ perfectly matches the laminar flamelet solution. This suggests that the presence of a local minimum in the oxidation layer, even spatially located very far from the flame surface, can significantly modify the final stages of combustion toward the fully burned products. Finally, the conditional means of the fuel reaction rate $\langle \dot{\omega}_{\rm CH_4} \rangle$ are shown in Fig. 6.17 a). The significant thickening observed for the temperature layer and the species is also reflected in the reaction rate and the same correlation with the conditioning variable ΔT^* is observed.

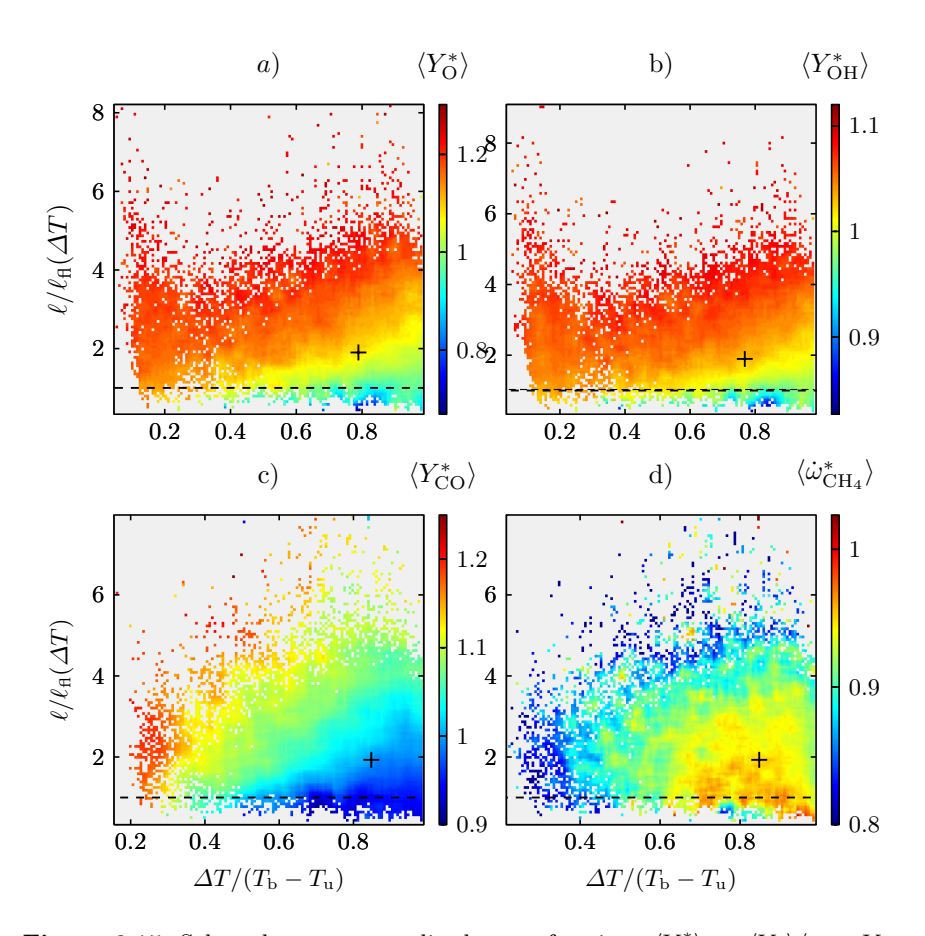


Figure 6.15: Selected mean normalized mass fractions $\langle Y_{\alpha}^{*} \rangle = \langle Y_{\alpha} \rangle / \max Y_{\alpha,\mathrm{fl}}$ and normalized CH₄ source term $\langle \dot{\omega}_{\mathrm{CH_4}}^{*} \rangle = \langle \dot{\omega}_{\mathrm{CH_4}} \rangle / \min \dot{\omega}_{\mathrm{CH_4},\mathrm{fl}}$ conditioned on the normalized DE parameters and the temperature of their respective maximum value in the laminar flamelet solution in the High Re case. The black crosses indicate the values of the mean DE parameters.

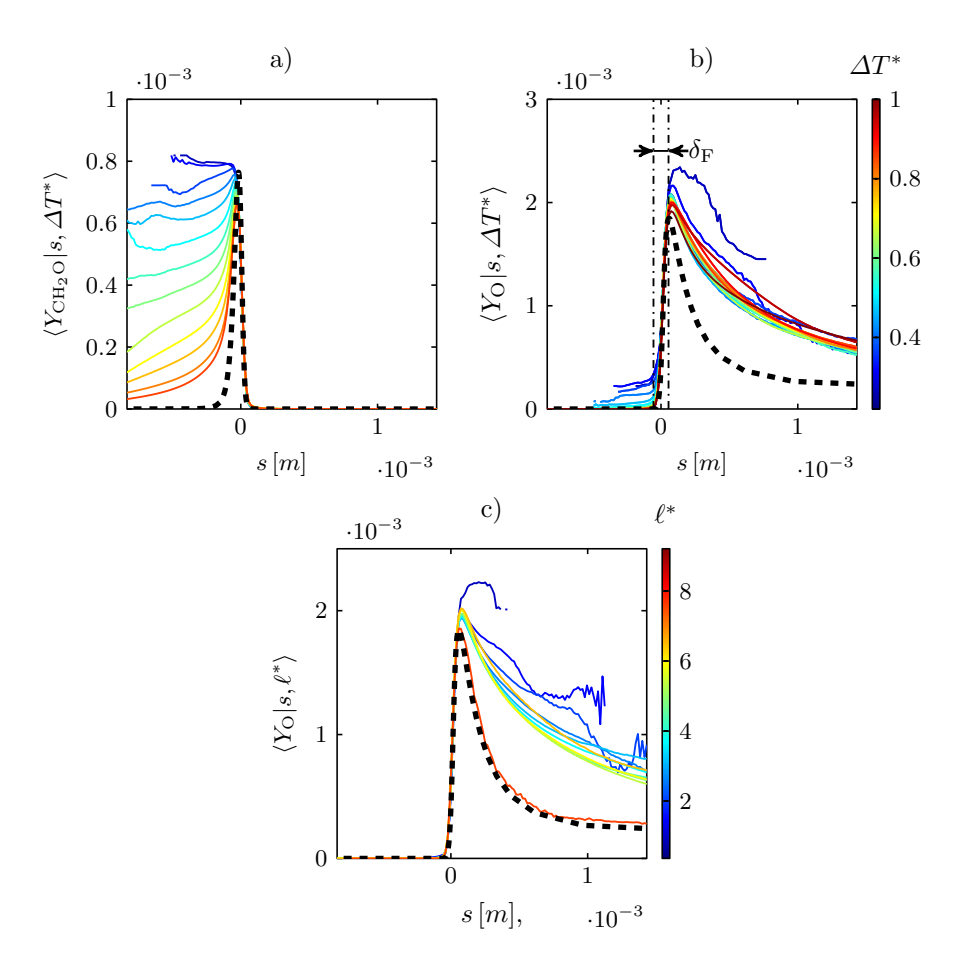


Figure 6.16: Mean mass fractions $\langle Y_{\alpha} \rangle$ in the High Re case conditioned on arclength distance s to the flame surface and conditioned on: the normalized scalar difference ΔT^* (a) and (b); the normalized DE length ℓ^* (b). The black dashed line indicates the laminar flamelet solution. The vertical dash-dotted lines indicate a single flame thickness $\delta_{\rm F}$ around the flame front.

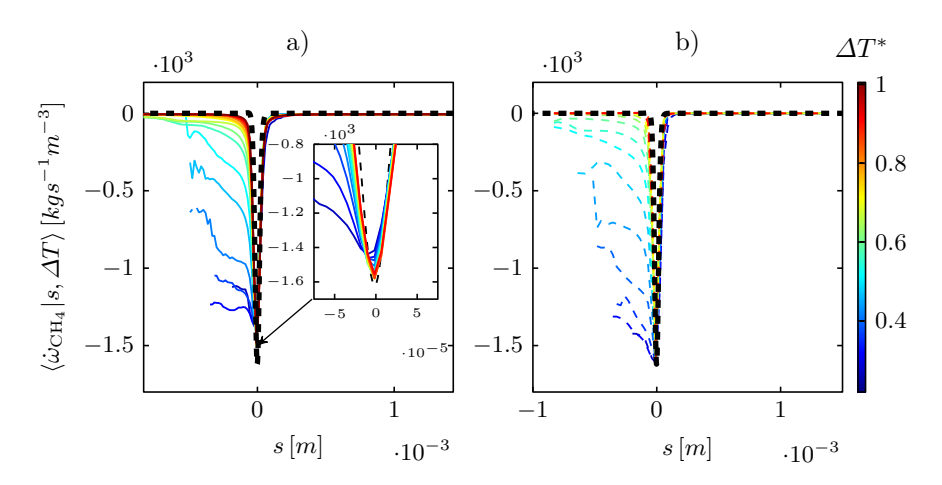


Figure 6.17: Mean CH₄ source term $\langle \dot{\omega}_{\text{CH}_4} \rangle$ in the High Re case conditioned on arc-length distance s to the flame surface and scalar difference ΔT^* . The black dashed line indicates the laminar flamelet solution. The solid lines indicate the DNS values and the colored dashed lines show the result of the flamelet progress variable model $\langle \dot{\omega}'_{\text{CH}_4} \rangle$. The black dashed line indicates the laminar flamelet solution.

The potential implications for modeling are investigated by computing the fuel reaction rate using only the temperature T(s) along the gradient trajectories and a flamelet model:

$$\dot{\omega}'_{\mathrm{CH}_4}(s) = \dot{\omega}_{\mathrm{CH}_4,\mathrm{fl}}(T(s)), \qquad (6.3)$$

with $\dot{\omega}_{\mathrm{CH_4,fl}}(T(s))$ being the value in the laminar flamelet solution for a given temperature.

A comparison between the DNS values of the reaction rate and that computed with the flamelet is also shown in Figs. 6.17 a) and b). The extent of the thickening is reproduced by the flamelet progress variable model $\langle \dot{\omega}'_{\text{CH}_4} \rangle$ as well. However, close to the flame front $s=0, \langle \dot{\omega}'_{\text{CH}_4} \rangle$ is larger than the source term obtained from the DNS cases.

6.2.3 Integral Statistics

In the previous sections, it was established that the DE parameters, foremost the decrease of the scalar difference ΔT of DEs crossing the flame front, have

a profound effect on the local flame structure in the form of a thickening of both preheat and inner reaction zones. To quantify the increase in the overall fuel consumption by the thickening effect, the integrated reaction rate $\dot{\Omega}$ along gradient trajectories is calculated as

$$\dot{\Omega} = \int_{s_{\text{total}}}^{s_{\text{end}}} -\dot{\omega}_{\text{CH}_4}(s) ds \tag{6.4}$$

with $s_{\rm start}$ being the arc-length distance to the minimum and maximum. The integrated fuel consumption $\dot{\Omega}_{\rm L}$ in a laminar flame unaffected by the influence of turbulence can be calculated by integrating the laminar flamelet solution in space across the same interval:

$$\dot{\Omega}_{\rm L} = \int_{s_{\rm that}}^{s_{\rm end}} -\dot{\omega}_{\rm CH_4, 1D}(s) \mathrm{d}s \tag{6.5}$$

where $-\dot{\omega}_{\mathrm{CH_4,1D}}(s)$ is the fuel consumption rate in the laminar flamelet in physical space. Therefore, the consumption coefficient $I_s = \dot{\varOmega}/\dot{\varOmega}_{\mathrm{L}}$ can be defined to indicate increased fuel consumption of the local flame structure $(I_s > 1)$ or decreased fuel consumption $(I_s < 1)$ compared to an unthickened fully laminar flame front.

The mean consumption coefficient $\langle I_s \rangle$, conditioned on the DE parameters is shown in Fig. 6.18 a). Small values of ΔT^* result in large integrated consumption of fuel in the corresponding flame structure, with the exception of very small values of the difference ($\Delta T^* < 0.3$) for which $\langle I_s \rangle$ decreases due to a lower value. For almost all values of the DE parameters, $\langle I_s \rangle$ is larger than one, while it converges to unity for large ΔT^* and very short ℓ . Combined with the influence of the Reynolds number on the DE parameters observed in Fig. 6.14 i.e., an increasing probability of small ΔT^* , this analysis of $\langle I_s \rangle$ is consistent with the increased total fuel consumption and increased turbulent flame speed with the Reynolds number observed by Antonio et al. 3.

To quantify the prediction for the consumption of the flamelet model using the temperature along the gradient trajectories T(s), cf. Fig. [6.17] b), the modeled integrated fuel consumption $\dot{\Omega}_T$ is calculated analogously to $\dot{\Omega}_s$

$$\dot{\Omega}_{\rm T} = \int_{s_{\rm end}}^{s_{\rm end}} -\dot{\omega}_{\rm CH_4,fl}(T(s)) \mathrm{d}s, \tag{6.6}$$

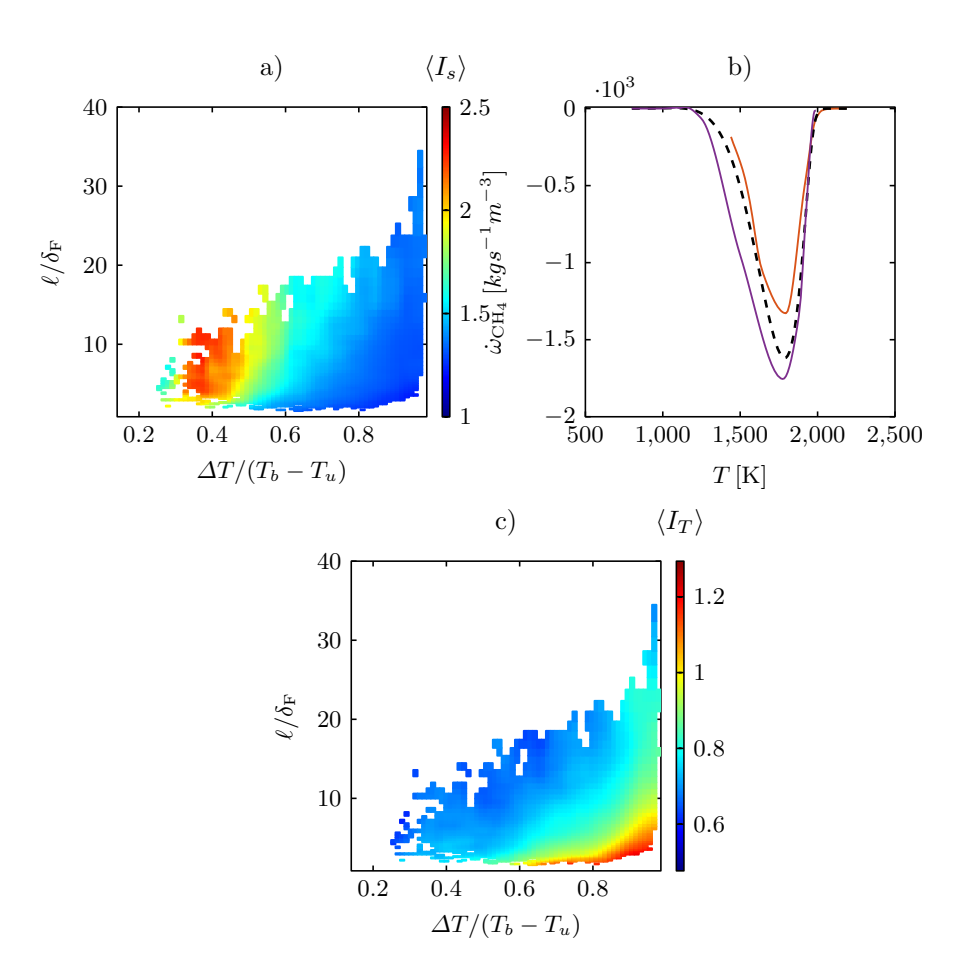


Figure 6.18: a): $\langle I_s \rangle$ conditioned on the normalized DE parameters $\ell/\delta_{\rm F}$ and $\Delta T/(T_{\rm b}-T_{\rm b})$ in the High Re case. b): Instantaneous CH₄ source term $\dot{\omega}_{\rm CH_4}(T)$ for two exemplary DEs (solid lines) and the laminar flamelet solution (black dashed line). c): $\langle I_T \rangle$ conditioned on $\ell/\delta_{\rm F}$ and $\Delta T/(T_{\rm b}-T_{\rm b})$ in the High Re case.

, but using the flamelet mapping $\dot{\omega}_{\text{CH}_4,\text{fl}}(T(s))$ to compute the local rate. A model consumption coefficient can be formed utilizing the modeled integrated fuel consumption $I_T = \dot{\Omega}/\dot{\Omega}_T$. The implications of different values for I_T are illustrated in Fig. 6.18 b), where two exemplary gradient trajectories are shown. The purple line corresponds to a DE with $I_T > 1$, as the $\dot{\omega}_{\text{CH}_4,\text{fl}}$ stays below the laminar flamelet value for the entire range of temperatures. The red line corresponds to a DE with $I_T < 1$. Therefore, $\langle I_T \rangle$ can be interpreted as an integrated efficiency factor, relating the actual fuel consumption to the theoretically achievable fuel consumption in the flamelet.

Finally, the mean of the model consumption coefficient $\langle I_T \rangle$, conditioned on the DE parameters, is shown in Fig. 6.18 c). It is observed that largely $\langle I_T \rangle < 1$, and equivalently the integrated fuel consumption remain below that of the flamelet progress variable model. In particular, for small values of ΔT^* it is significantly smaller than one.

The following overall picture emerges from this analysis. For small values of ΔT^* , which correspond to thickened flame regions, $\langle I_T \rangle$ drops to values significantly smaller than one, or equivalently the local fuel consumption rate in the DNS is smaller than the corresponding flamelet value. However, the large values of $\langle I_s \rangle$ in the same regions indicate that the decrease of the local reaction rate with respect to the laminar flame is more than compensated by the thickening of the reaction layer, with the final result of an increase of the turbulent consumption speed.

7 Gradient Trajectory Statistics Based Modelling Applications

In this chapter, the insights gained through the gradient trajectory analysis of turbulent combustion in the previous chapters will be applied to two different aspects of combustion modelling. First, a systematic approach to regime prediction in simulations of engineering applications using DE parameter statistics is presented and applied. Second, a new approach to modelling the mixture fraction probability density function is developed. Here, gradient trajectories provide the means for considering additional important effects in non-premixed combustion such as fully laminar regions and external intermittency in turbulent/non-turbulent interface regions.

7.1 Prediction of Non-Premixed Combustion Regimes

In turbulent combustion, the various existing regimes exist pose implications on the accompanying modelling procedure. In essence, turbulent scales are compared to different scales of the flame to determine the turbulence-flame interaction [95]. Most conventional operation points of diesel engines fall into the flamelet regime, where an ensemble of thin laminar flame structures is attached to the flame surface, which is wrinkled by turbulence. However, in certain operation points, the separation of scales between turbulence and combustions ceases to exist due to the low temperatures and the consequently longer chemical time scales or high local turbulence intensities where a flamelet assumption is expected to be less accurate [16]. While current state of the art computational fluid dynamics (CFD) simulations are capable of producing satisfactory statistical results for passenger car internal combustion engines (ICEs) with reasonable computational costs, the inherent modelling assumptions regarding both the turbulence and the chemistry limits the predictiveness of these simulations. This is especially true for low load operation points or comparably slow chemical processes, such as the soot formation process, where scale interactions between turbulence and combustion cannot be considered. These scale interactions have to be investigated in very costly direct numerical simulations (DNS), where all turbulence and flame scales are resolved.

The correlation between DE parameters and the dynamics of reacting scalars was investigated by means of 3D-DNS of non-premixed methane jet flames featuring detailed finite rate chemistry in chapter [4,3]. The idealised configuration of the DNS of the temporally evolving planar jet flame was chosen for the ease and precision of obtaining statistics, but more importantly, to realise the highest possible Reynolds number with the available computational resources. While a DNS of a real ICE is highly desirable, the computational costs to generate any statistically significant sample size for a single operation point would be astronomical and unfeasible to conduct on any super computer of the current generation or in the foreseeable future.

To apply the insight of the scale interaction gained through the DE analysis of the DNS of the jet flames onto real world combustion applications, a modelling framework is proposed. Statistics of normalized DE parameters are modelled by employing adapted stochastic transport equations originally developed for isotropic turbulence by Wang and Peters [98] [128]. Scaling laws are exploited for the modelling of the mean DE parameters in the CFD simulations of a passenger car direct injection (DI) diesel engine. The DE statistics are then used for a spatial and temporal classification of the non-premixed combustion regimes in the CFD. The CFD simulations feature a wide range of operation points, including variations in injection timings, the intake pressure and the exhaust gas recirculation.

The modelling framework yields plausible results with regards to the overall trends in the operation parameters on non-premixed combustion regimes as well as the location and time of critical scale interactions in the DI diesel combustion process. It is found that the flamelet regime is indeed the overall dominant form of combustion in all investigated operation points, but there are periods in the early injection process where the scale interaction dominates.

7.1.1 Modelling Framework

In chapter 5, the DE analysis was applied to the mixture fraction field Z, as it provides the most meaningful scales for non-premixed combustion. In this context, a DE can be interpreted as a grouping of flamlets which share the same start and end points in space and therefore, the same boundary conditions. Using the DE parameters, four distinct regimes combustion regimes can be identified cf. sec. 5.2. The first regime boundary divides the combustion regimes into burning and extinction regimes. Here, the DE gradient $g = \Delta Z/\ell$ is used analogously to the scalar dissipation rate. In the

limit of small DEs, the following relation is true:

$$\lim_{\ell \to 0} g = \left| \frac{\partial Z}{\partial x_i} \right| . \tag{7.1}$$

From this follows the proportionality of the scalar dissipation rate χ and the DE gradient g,

$$\chi = 2D \left(\frac{\partial Z}{\partial x_i} \right)^2 \sim Dg^2,$$
(7.2)

with the molecular diffusion coefficient of the mixture fraction D. The strong correlation between g and χ was first observed in isotropic turbulence [98], but also in free shear flows [53] and in reacting flows [58] [41]. The quenching DE gradient g_q is then obtained by conditioning the mean DE gradient on the quenching scalar dissipation rate

$$g_{\mathbf{q}} = \langle g | \chi = \chi_{\mathbf{q}} \rangle.$$
 (7.3)

The second regime boundary separates the large scale combustion, which is consistent with the flamelet assumptions and the small scale combustion. To achieve this in a premixed flame, the Kolmogorov scale η would be compared to the flame thickness [91]. However, in the context of non-premixed flames, the flame thickness varies greatly with the local mixture fraction gradient. Instead, the scales in Z-space are used for an evaluation of large scale or fine scale interactions. Flamelets are defined along gradient trajectories of the mixture fraction field [97], which are identical to the gradient trajectories forming the DEs. Therefore, the DE scalar difference ΔZ limits the length in Z-space in which a flamelet solution exists before being terminated by a turbulence induced extremal point. It is easy to imagine that a DE with a small ΔZ centered around the reaction zone interferes with a flamelet assumption of a largely laminar flame structure. The combustion scale for the comparison is the reaction zone thickness in Z space from the stationary flamelet solution $\delta Z_{\rm r}$. $\delta Z_{\rm r}$ is approximated by the half width of the Gaussian of the heat release rate, cf. eq. (3.6). For all jet flames, regardless of the Reynolds number, Damköhler number or fuel composition, it was found that for a value of $\Delta Z < 15\Delta Z_{\rm r}$, the assumption of a 1D flamelet ceases to be valid, as seen if Fig. 5.15. This value was therefore chosen as the second regime boundary.

To apply the insight gained from the DE analysis of the DNS of the temporally evolving jet flames to real world engineering applications, a three pronged modelling approach is used to predict non-premixed combustion regimes with the aid of the mean quantities available in CFD simulations. A similar approach was used by Peters et al. [96] to successfully predict super-knock events in turbo-charged spark-ignition engines.

Firstly, the probability density function (PDF) for the normalized DE length $\ell^* = \ell/\ell_{\rm m}$, with the mean DE length $\ell_{\rm m}$, are modelled using the semi-empirical stochastic transport equations originally developed by Wang and Peters [98]. The PDF of the normalized DE length displays an invariance towards changes in Reynolds number and underlying scalar fields, which was observed for isotropic turbulence [98] [128]. the physical mechanisms governing the evolution of DEs can be used to describe their behavior. Wang and Peters [127] derived a semi-empirical stochastic transport equation for the PDF of the normalized DE length $P(\ell^*,t)$, taking the following mechanisms into account:

- 1. The generation of new extremal points resulting from random eddy turnover of Obukhov-Corrsin eddies. The introduction of extremal points leads to a cutting of DEs.
- 2. The elimination of extremal points by diffusion and the consecutive joining of dissipation elements.
- 3. The disappearance of small DEs when ℓ^* approaches zero.

For simplicity, the spatial dependency of the statistics is neglected:

$$\frac{\partial P(\ell^*, t)}{\partial t} + \frac{\partial}{\partial \ell^*} (v^*(\ell^*) P(\ell^*, t)) = 2\Lambda \int_0^\infty P(\ell^* + z^*, t) dz$$

$$- \Lambda \ell^* P(\ell^*, t) + 8 \left. \frac{\partial P(\ell^*, t)}{\partial t} \right|_{\ell^* = 0} \left[\int_0^{\ell^*} \frac{z^*}{\ell^*} P(\ell^* - z^*, t) P(z^*, t) dz^* - P(\ell^*, t) \right].$$
(7.4)

Here, the only external parameter is the non-dimensional cutting frequency per unit length $\Lambda = \lambda \ell_{\rm m}^2/(D_Z)$, taking the diffusivity of the mixture fraction field D_Z as well as the cutting frequency per unit length of the Obukhov-Corrsin eddies λ into account. The non-dimensional diffusive drift velocity is defined as

$$v^*(\ell^*) = -\frac{1}{\ell^*} (1 - c\ell^* \exp(-\ell^*)), \qquad (7.5)$$

with the coefficient c to be determined by satisfying the space conservation, i. e., disappearing segments need to be added to longer elements so the overall length of all DEs remains the same. The model results of $P(\ell^*)$ are compared

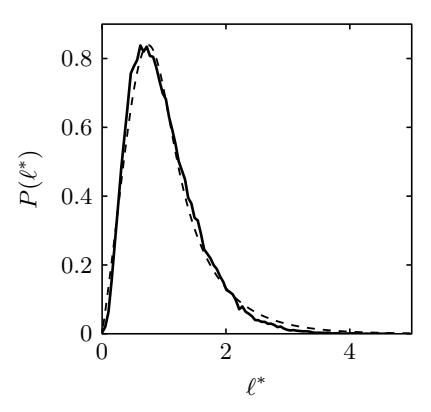


Figure 7.1: PDF of the normalized DE length $\ell^* = \ell/\ell_m$. (—): statistics directly obtained DNS and (--): modeled statistics obtained from the stochastic transport equation eq. (7.7).

to the PDF obtained from a planar temporally evolving jet flame are shown in Fig. 7.1a).

To adequately describe the mixture fraction field, the second DE parameter needs to be considered. Following the procedure of Wang and Peters [128], the JPDF is modelled using the previously obtained marginal PDF and the model equation for the conditional PDF of the scalar difference and using Bayes' theorem

$$P(\ell^*, \Delta Z^*) = P(\ell^*)P(\Delta Z^*|\ell^*). \tag{7.6}$$

The stochastic transport equation for the conditional PDF $P(\Delta Z^*|\ell^*)$ was derived analogously to eq. 7.4 by Wang and Peters 128 considering the same fundamental physical mechanisms

$$\frac{\partial}{\partial t} \left[P_{c}(\Delta Z^{*}|l^{*}, t) P(l^{*}, t) \right]
+ \frac{\partial}{\partial l^{*}} \left[(v_{l}^{*} P_{c}(\Delta Z^{*}|l^{*}, t) P(l^{*}, t)) \right] + \frac{\partial}{\partial \Delta Z^{*}} \left[(v_{\Delta Z}^{*} P_{c}(\Delta Z^{*}|l^{*}) P(l^{*}, t)) \right] = \\
\Lambda \left[2 \int_{0}^{\infty} P_{c}(\frac{\Delta Z^{*}}{k}|l^{*} + y^{*}, t) (P(l^{*} + y^{*}, t)) \frac{1}{k} dy^{*} - l^{*} P_{c}(\Delta Z^{*}|l^{*}, t) P(l^{*}, t) \right] \\
+ 2 \left. \frac{\partial P(l^{*}, t)}{\partial l^{*}} \right|_{l^{*} = 0} \left[\int_{0}^{c\Delta Z^{*}} \int_{0}^{l^{*}} \frac{z}{l^{*}} P_{c}(c\Delta Z^{*} - \psi|l^{*} - z, t) P_{c}(\Delta \psi|l^{*}, t) \\
P(l^{*} - z, t) P(z, t) dz c d\psi - P_{c}(\Delta Z^{*}|l^{*}, t) P(l^{*}, t) \right], (7.7)$$

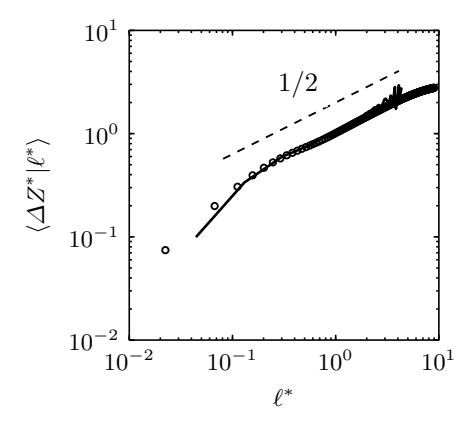


Figure 7.2: (-): The mean normalized scalar difference conditioned on the normalized DE length ℓ from the high Re case and (-): conditional mean obtained from the modified stochastic transport equation eq. (-7.7).

with the model constants k and c compensating for an increased scalar variance and after a DE cutting event and a reduced scalar variance in case of a reconnection event, respectively. k and c determine the characteristic scaling of $\langle \Delta Z^* | \ell^* \rangle$. The normalized drift velocity in scalar difference direction $v_{\Delta Z}^*$ is defined as

$$v_{\Delta Z}^*(\ell^*, \Delta Z^*) = -\left(12\frac{\Delta Z^*}{\ell^*} \exp\left(-a\ell^*\right)\right)$$
(7.8)

where a has to be determined from the conservation of the total ΔZ^* analogous to eq. (7.5). A comparison between $\langle \Delta Z^* | \ell^* \rangle$ obtained from the modelled JPDF and the conditional mean obtained from the previously shown planar temporally evolving jet flame is shown in fig. (7.2).

Secondly, the combustion scales need to be determined in every time step t of the CFD. For this, the steady state flamelet solutions are calculated for the boundary conditions of the CFD simulation. Using $\psi_{\alpha,1}$ and $\psi_{\alpha,2}$, the composition of the reacting scalars of the oxidizer and the fuel stream, the quenching gradient g_q is calculated in every time step

$$g_{\rm q}(t) \sim (\chi_{\rm q}(\psi_{\alpha,1}(t), \psi_{\alpha,2}(t))/D_{\rm st})^{0.5}$$
 (7.9)

The reaction zone thickness in Z-space $Z_{\rm r}(t)$ is calculated using eq. (3.6) with the unsteady flamelet solution used in the modelling of the reacting scalars in the current time step.

Thirdly, the mean DE parameters are modelled using temporally and spatially resolved mean quantities of the CFD simulations. The previously observed scaling of the mean DE length with the Kolmogorov micro scale η , cf. Figs. 5.3 and 6.4 is exploited for the modelling of $\ell_{\rm m}$

$$\ell_{\mathbf{m}}(t, x_i) \sim \left(\overline{\nu}(t, x_i)^3 \widetilde{\varepsilon}(t, x_i)^{-1}\right)^{1/4}, \tag{7.10}$$

with the mean kinematic viscosity $\overline{\nu}$ and the Favre averaged dissipation rate of the turbulent kinetic energy $\widetilde{\varepsilon}$.

Using the theoretical scaling of the first order scalar structure function with an exponent of 1/3 [127], the mean DE scalar differences is modelled following [96]

$$\Delta Z_{\rm m}(t,x_i) \sim \ell_{\rm m}^{1/3} \frac{\widetilde{\chi}(t,x_i)^{1/2}}{\widetilde{\varepsilon}(t,x_i)^{1/6}} \int_{0}^{\infty} \ell^{*1/3} f(\ell^*,t) d\ell^*.$$
 (7.11)

The mean DE gradient $g_{\rm m}$ is obtained using the correlation between g and χ analogous to eq. [7.2]

$$g_{\rm m}(t,x_i) \sim \widetilde{\chi}(t,x_i)^{0.5} \overline{D}^{-0.5}$$
 (7.12)

Finally, the probability of encountering a certain combustion regime P_j can be computed by denormalizing the modelled DE parameter JPDF with the mean DE parameters $f(g, \Delta Z) = \Delta Z_{\rm m} g_{\rm m} f(g^*, \Delta Z^*)$ and integrating the JPDF over the suitable intervals. The intervals are dictated by the regime boundaries. For example, the local probability of the "Burning Flamelet" regime is calculated as follows

$$P_{\text{Flamelet}} = \int_{\Delta Z_{*}}^{\infty} \int_{0}^{g_{q}} f(g, \Delta Z) dg d\Delta Z, \qquad (7.13)$$

with the small scale interaction boundary value $\Delta Z_{\rm t} = 15\delta Z_{\rm r}$.

7.1.2 Engine Simulations

3D CFD simulations of a passenger car DI diesel engine were performed with the in-house flow solver AC-FluX applying the representative interactive flamelet (RIF) model. AC-FluX is based on finite volume methods and employs unstructured, mostly hexahedral meshes. It is mainly used for spark

ignition and diesel engine simulations. The simulated engine is a four-cylinder GM Fiat diesel engine with a bore of 82 mm and a stroke of 90.4 mm, the overall displacement is 1.91. Details regarding the numerical methods and the validation of the simulations on the engine test bench can be found in Jochim, Korkmaz, and Pitsch 69.

The operation points for which the modelling of the combustion regimes was conducted were chosen to allow for a precise investigation of the impact of the most commonly varied parameters on the combustion process. To achieve this, only one parameter is changed from operation point to operation point to isolate the effects. The varied parameters include the injection pressure $p_{\rm inj}$, the intake pressure $p_{\rm intake}$, the exhaust gas recirculation (EGR), combustion phasing (CA50) and mean effective pressure (IMEP). More details regarding the simulated operating points are listed in tab [7.1] The baseline case, for which the modelling results are discussed in more detail in the following section, is situated in the center of the parameter space.

p _{inj} [bar]	p_{intake} [bar]	EGR [%]	$\begin{array}{c} {\rm CA50} \\ {\rm [^{\circ}CA~aTDC]} \end{array}$	IMEP [bar]
1300	1.5	20	8	8
1600	1.5	20	8	8
2000	1.5	20	8	8
1600	1.3	20	8	8
1600	1.7	20	8	8
1600	1.5	0	8	8
1600	1.5	10	8	8
1600	1.5	30	8	8
1600	1.5	20	6	8
1600	1.5	20	10	8
1600	1.5	20	8	4
1600	1.5	20	8	6

Table 7.1: Simulated operating points in the CFD of the DI diesel engine. Only one setting is changed in each point in order to differentiate the source of the different effects. The baseline case is indicated by the bold text.

7.1.3 Modelling Results

The results of the modelling of the mean DE parameters $g_{\rm m}$ and $\Delta Z_{\rm m}$ in the CFD simulation for the base line case are shown in fig. [7.3] The JPDF of the modelled mean DE parameter at the iso-surface of $Z_{\rm st}$ are shown for three crank angle positions after top dead center (°CA aTDC). The range of the values changes considerably over the course of the combustion process. This change seems plausible with high gradients and large scalar differences during the injection and liquid jet breakup phases, to lower gradients and smaller scalar differences during the fully developed combustion process.

The spatial distribution of the combustion regimes is illustrated in Fig. [7.4]. The local probability of the "Burning Flamelet" regime $P_{\rm Flamelet}$ is mapped onto the iso-surface of $\widetilde{Z}_{\rm st}$ of the baseline case. One observes a high spatial inhomogenity of the $P_{\rm Flamelet}$ distribution with patches of zero probability, which is still observed at the latest crank angle position. For a more quantitative comparison of the individual regime contributions, the surface area of the regimes is calculated

$$A_j = \iint_{\widetilde{S}_{st}} P_j(x_i) d\widetilde{S}_{st}, \qquad (7.14)$$

with the surface area of the mean stoichiometric mixture fraction $\widetilde{S}_{\rm st}$. The normalized temporal evolution of the surface area of the four regimes is in the baseline case is shown in Fig. [7.5]. The normalization is performed with the area of the entire stoichiometric iso-surface for the coresponding time step $A_{\rm st}$. While the most prominent combustion regime is the "Burning Flamelet" regime for the majority of the time steps, the dominant regime during the late injection and jet breakup process is the "Fine Scale Mixing" regime. The high probability of the "Fine Scale Mixing" regime $P_{\rm Fine\ Scale}$ is not limited to the baseline case but is found in all the operation points during this combustion phase. The extinction regimes remain largely irrelevant. To measure the overall contribution of the combustion regimes to the entire process, the integrated regime probability is calculated

$$\mathcal{P}_{j} = \int_{t_{0}}^{t_{\text{end}}} A_{j} A_{\text{st}}^{-1} dt.$$
 (7.15)

The integrated regime Probability for the "Burning Flamelet" regime $\mathcal{P}_{\text{Flamelet}}$ is shown for all operation points in Fig. [7.6]. Overall, most operation points

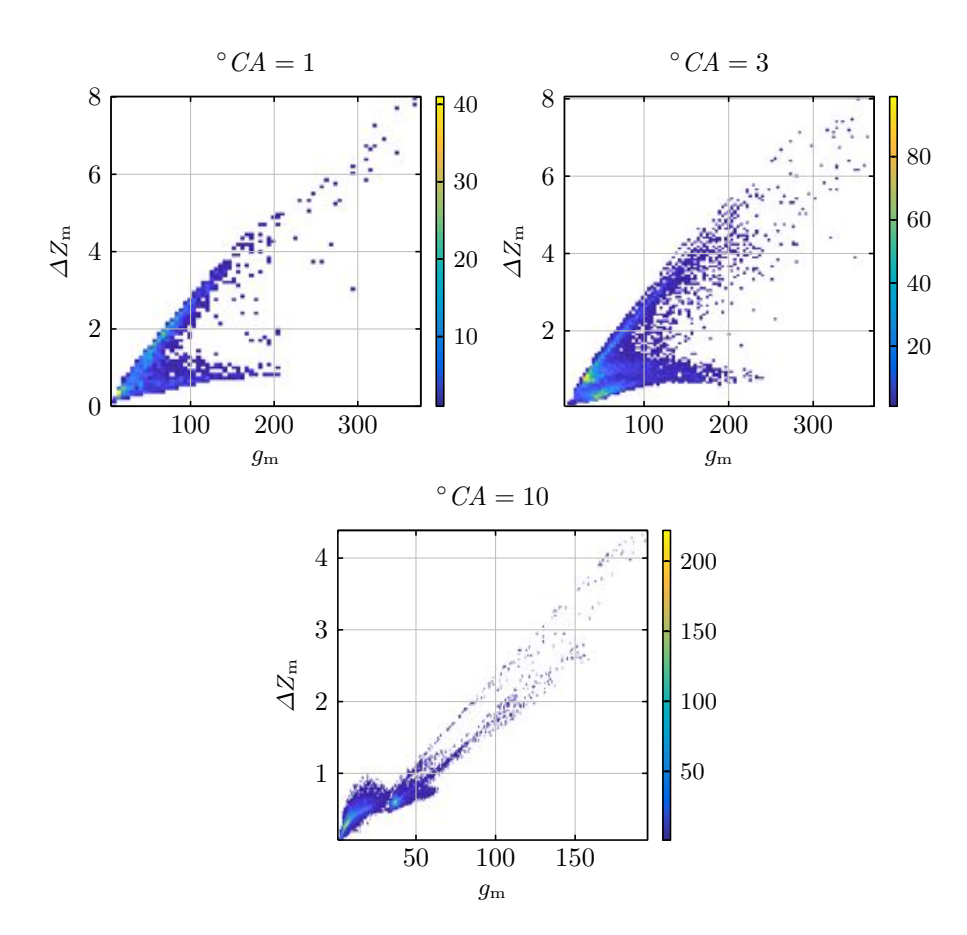


Figure 7.3: JPDF of modelled normalized DE parameters at the iso-surface of $\widetilde{Z}_{\rm st}$ for three crank angle positions for the baseline case.

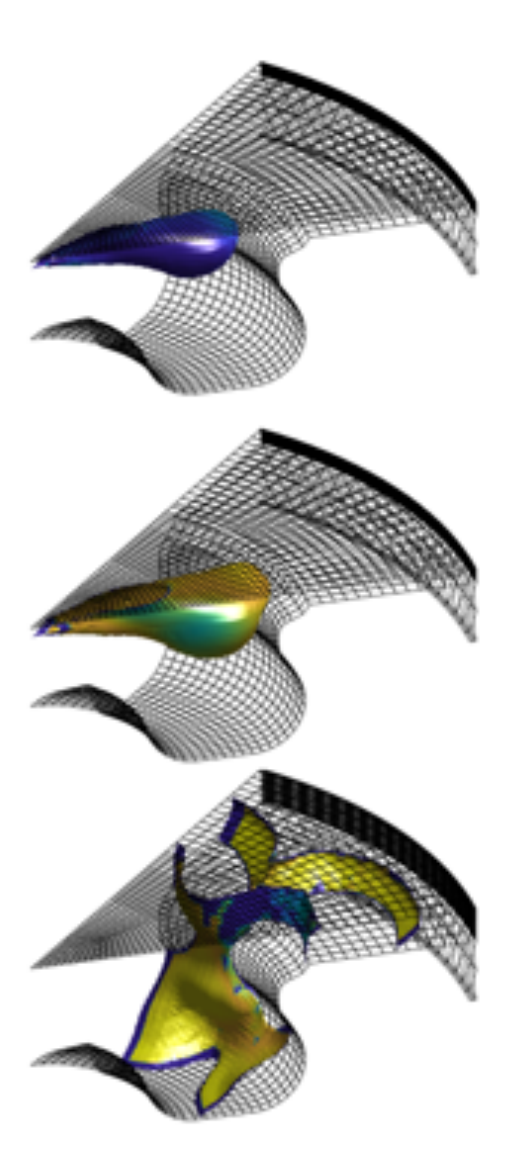


Figure 7.4: Mean stoichiometric iso-surface for three different crank angle positions in CFD simulation of the baseline case. The colour of the iso-surface indicates the local probability of the "Burning Flamelet" regime from Blue ($P_{\rm Flamelet}=0$), over green to yellow ($P_{\rm Flamelet}=1$). Top to bottom: ${}^{\circ}CA=3$, ${}^{\circ}CA=4$ and ${}^{\circ}CA=13$. The black wireframe indicates the piston bowl geometry and the liner.

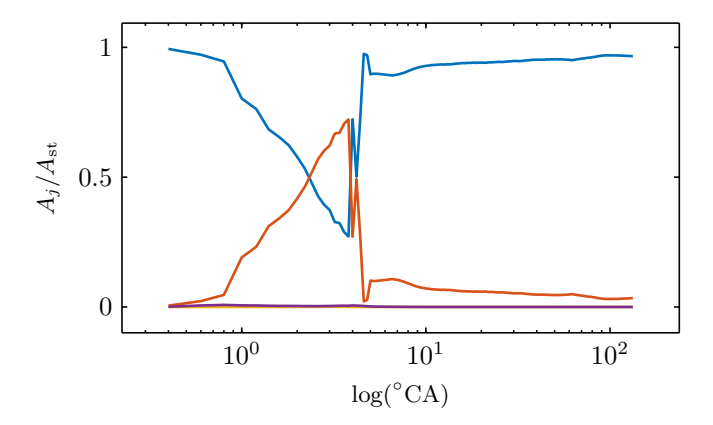


Figure 7.5: Temporal evolution of the stoichiometric iso-surface attributed to the individual regimes normalized with the overall surface area in the respective time step for the baseline case. —: "Burning Flamelet" regime, —: "Fine Scale Mixing" regime, —: "Broken Reaction Zones" regime and —: "Large Scale Extinction" regime.

show high values of $\mathcal{P}_{\text{Flamelet}}$ in the 90% range. This is consistent with the broad use of flamelet models in DI diesel CFD and the validated results achieved with such simulations. With the exception of the EGR, the impact of the operation parameters on $\mathcal{P}_{\text{Flamelet}}$ is sensible as well. The engine load has by far the highest impact on the combustion regimes with only 70% of the integrated regime Probability being attributed to a flamelet like combustion at an IMEP of 4 bar. This is especially relevant, as most recent efforts for optimising ICEs focus on the low load operation points.

7.2 A New Modeling Approach for Mixture Fraction Statistics Based on Dissipation Elements

Many modeling approaches for real world engineering combustion applications are based on the mixture fraction Z. An example is the flamelet model [92]. In this model, the assumption of fast, but not infinitely fast, chemical time scales leads to thin laminar flame structures attached to the larger flame surface which is corrugated by turbulence. In the context of non-premixed combustion in the flamelet regime, all reacting scalars are a function of the mixture fraction Z and the scalar dissipation rate $\chi_{\rm st}$ at the position of the stoichiometric mixture fraction or progress variable. As the mixture fraction

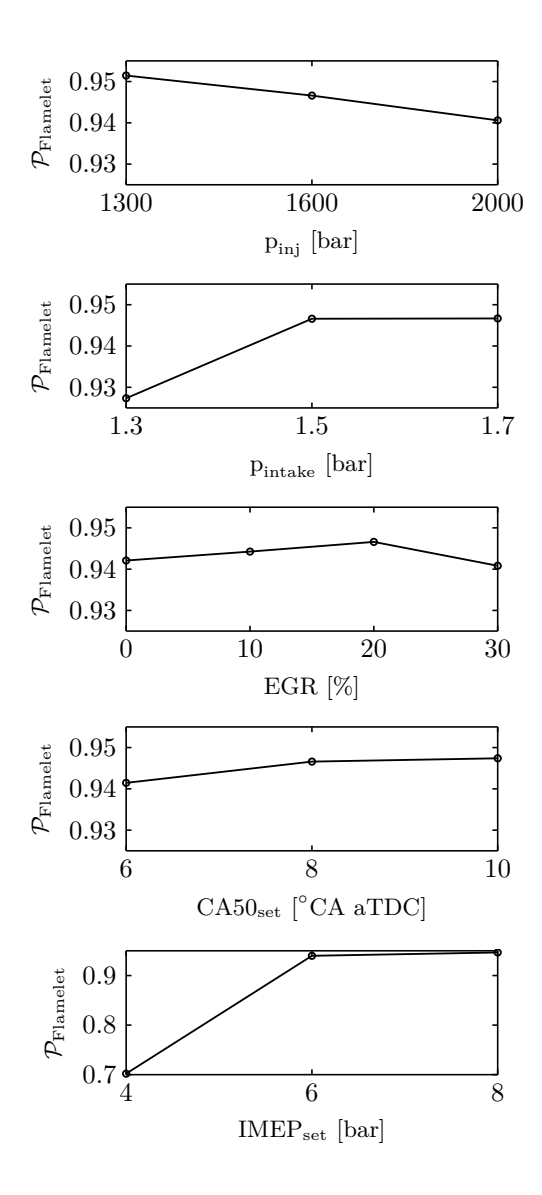


Figure 7.6: Integrated probability of the "Burning Flamelet" regime $\mathcal{P}_{\text{Flamelet}}$ in all simulated operation points.

is a randomly fluctuating quantity in a turbulent flow, the accurate prediction of the PDF of the mixture fraction P(Z) is of fundamental importance to the quality of any simulation employing flamelets or any other mixture fraction based combustion models.

Therefore, extensive efforts have been made to understand and model the properties of the mixture fraction PDF [15], [71], [25]. In a binary mixing process in a fully turbulent flow, P(Z) is most commonly modeled employing the beta function $P_{\beta}(Z)$ [51]. Conveniently, $P_{\beta}(Z)$ can be computed exclusively from the mean \overline{Z} and variance $\overline{Z'^2}$, which are readily available in most Reynolds Averaged Navier Stokes (RANS) simulations.

The usage of $P_{\beta}(Z)$ stems in large part from the ability to match experimentally measured mixture fraction PDFs. However, in highly intermittent flows, P(Z) displays shapes which cannot be adequately reproduced by $P_{\beta}(Z)$, such as more complex multimodal shapes or a singularity at either Z=0 or Z=1 and an intermediate local maximum. Due to limitations of the experimental setups and measurement techniques, fundamental turbulent combustion experiments often use diluted fuels and consequently a high stoichiometric mixture fraction. Yet, real world combustion applications of hydrocarbons rarely employ diluted fuel streams and therefore typically have very low values of $Z_{\rm st}$. This places the combustion in the highly intermittent region at the outer edge of the turbulent regions in free shear flows in the vicinity or even inside the turbulent/non-turbulent interface (TNTI) [105].

Effelsberg & Peters $\boxed{46}$ argued that the TNTI represents a third regime of finite thickness in free shear flows, which separates the laminar outer flow and fully turbulent inner flow. To account for the effects of the TNTI layer on the statistics of Z, they derived a composite PDF model taking the previously mentioned three regimes into account.

Excellent agreement with experimental data of round jets with a wide range of Reynolds numbers was reported 54. However, this model relies on the first four moments of the mixture fraction \overline{Z} - $\overline{Z^4}$. On top of the challenge of solving transport equations for up to $\overline{Z^4}$ with a multitude of further modeling assumptions required to close these transport equations, the inherent nature of the diffusively dominated TNTI layer and the ill posed eddy viscosity $\nu_{\rm t}$ in the vicinity of laminar regions poses the question whether this not only impractical but potentially impossible in a RANS sense.

A potential substitute for the lack of the higher moments of Z in RANS proposed here is the use of gradient trajectory (gradient trajectory) statistics. Peters & Troulliet [97] demonstrated the reconstruction of P(Z) and $P(\chi)$ using data from a DNS of a temporally evolving mixing layer by means of

gradient trajectories of the mixture fraction field. Furthermore, gradient trajectories were used in the precise regime classification of free shear flows into turbulent core regions, interface regions, and the outer flow by Mellado et al. [84].

The invariance of ℓ^* observed in non-reacting configurations carries over to reacting flows as seen in Figs. [6.5] and [5.3] and if the scalar field does not possess a source term, of $\Delta\phi^*$ as well, cf. Fig. [7.7] Indeed, the reconstruction of P(Z) obtained from the experimental measurements of an inert round jet using only DE parameter statistics was demonstrated [56].

In the first part of this section, after a brief description of the numerical methods, a gradient trajectory based investigation of the the Z-fields obtained from three DNS data sets is shown and the reconstruction of P(Z) by means of DE parameter statistics will be demonstrated. The first configuration is a moderately turbulent inert planar temporally evolving jet. To show the feasibility of the approach in reacting flows, a non-premixed planar temporally evolving jet flame with a comparable Reynolds number is also considered. Additionally, to rule out any particularities of a temporally evolving configuration or effects of low Reynolds numbers, the reconstruction procedure is applied to a highly turbulent inert spatially evolving mixing layer.

In the second part, a DE-parameter statistic based composite PDF approach $P_{\rm DE}$ will be explained exploiting the invariances of the normalized DE parameters and scalings with statistical quantities readily available in RANS. Additionally, the model assumptions for the DE parameter statistics are motivated and justified by means of the Z-fields of the three DNS cases.

Finally, the modelling results for $P_{\rm DE}(Z)$ are presented and compared to the DNS results. Unlike the beta PDF, $P_{\rm DE}(Z)$ captures all important characteristics of the mixture fraction in the turbulent core, as well as the TNTI layer of the respective configurations. The initial analysis and the final validation are based on three high fidelity DNS data sets. The first configuration is an inert non-dimensional planar temporally evolving jet henceforth called the Inert Jet. The configuration and numerical methods are summarized in Section 4.3 The second configuration is a non-premixed planar temporally evolving jet called the Jet Flame in the following investigation likewise described in Section 4.3

The final configuration is a non-dimensional inert planar spatially evolving mixing layer henceforth called the Mixing Layer. Along the stream-wise direction, the boundary conditions are imposed inflow at x = 0 and free outflow 86 at $x = L_x$. The boundary conditions are periodic in the span-wise

	Jet Flame	Inert Jet	Mixing Layer
$Re_{\rm jet,0}$	10,000	9,850	-
Re_{λ}	86.4	101.1	305.1
L_x	$8.5H_{0}$	$6\pi H_0$	$473\delta_{\omega,0}$
L_y	$8.2H_{0}$	$12.5H_{0}$	$290\delta_{\omega,0}$
L_z	$6.4H_{0}$	$6\pi H_0$	$158\delta_{\omega,0}$
$n_{\text{gridpoints}} [10^9]$	1.2	8.6	18.7
Δ/η	0.86	1.4	1.1

Table 7.2: Numerical and physical initial parameters of the DNS.

direction and free-slip in the crosswise direction. The inflow is a hyperbolic tangent profile for the stream-wise velocity u with prescribed initial vorticity thickness $\delta_{\omega,0}$. Low amplitude white noise is superimposed on the hyperbolic tangent profile, resulting in the faster facilitation into a fully turbulent flow downstream from the inlet. The Taylor micro scale based Reynolds number reaches up to $Re_{\lambda} = u'\lambda/\nu \approx 305.1$, with the turbulence intensity u'. The resolution in the investigated regions is $\Delta/\eta \leq 1.1$. Further details regarding the configuration can be found in [7]. The Mixing Layer DNS was performed solving the unsteady Navier-Stokes equations in the low Mach number limit employing the solver NGA developed at Stanford University [43]. Identical to the methods employed for the Jet Flame DNS, the solver implements a finite difference method on a spatially and temporally staggered grid with the semi-implicit fractional-step method [70]. Additionally all three investigated cases are summarized in tab. [7,2]

7.2.1 Gradient Trajectory Analysis

In the following section, the profoundly different characteristics of the zonal PDFs in the turbulent core $P_{\rm TC}(Z)$ and in the TNTI layer $P_{\rm TNT}(Z)$ will be investigated using gradient trajectory analysis. The crucial ability of considering non-local effects in an analysis employing gradient trajectories will be exploited.

Regime Decomposition

A challenge faced in the analysis of free shear flows is the presence of both laminar and turbulent regions. Physical properties of the flow change drastically from one region to the other. Therefore, it is apparent to see that precisely separating turbulent and laminar parts is of prime importance to obtain meaningful statistics. While different and easy-to-use methods of locating the TNTI exist [105] [17], the flow in the turbulent region just behind the TNTI would not be considered fully turbulent [33]. Simply using all material points behind the TNTI would potentially lead to the inclusion of low Reynolds number effects in the statistics. The region between the TNTI and the turbulent core needs to be considered a third region [46].

A method based on gradient trajectories for a precise regime classification was proposed by Mellado et al. [84]. The turbulent core region of a free shear flow is defined by regions of the flow which possess DEs, i.e. regions in which all material points can be linked to a pair of extremal points via gradient trajectories. The TNTI region is then defined by the material points whose gradient trajectories cross the TNTI as defined by the method of Bisset et al. [17], which uses thresholds of the enstrophy for the TNTI detection.

Statistics of the arithmetic mean $Z_{\rm m}$ between the extremal points connected by gradient trajectories of a DE

$$Z_{\rm m} = \frac{Z_{\rm max} + Z_{\rm min}}{2} \,,$$
 (7.16)

with Z_{max} and Z_{min} being the mixture fraction in the maximum and the minimum, respectively, and the scalar difference ΔZ in these points

$$\Delta Z = Z_{\text{max}} - Z_{\text{min}} \,, \tag{7.17}$$

show distinctly different characteristics in the two flow regimes. In Fig. [7.7] this is demonstrated via the joint probability density functions JPDFs of the two DE parameters in the turbulent core $P_{\rm TC}(Z_{\rm m},\Delta Z)$ and in the TNTI region $P_{\rm TNT}(Z_{\rm m},\Delta Z)$. The JPDFs display fundamentally different shapes in the two flow regimes, with $P_{\rm TNT}(Z_{\rm m},\Delta Z)$ displaying a thin line at $Z_{\rm m}=\Delta Z/2$. This signifies that the gradient trajectories indeed continue indefinitely once the TNTI is crossed. Furthermore, the fundamental differences serve to highlight the importance of the consideration of a distinct TNTI region in a model approach for P(Z) in free shear flows.

7.2.2 Modeling The Mixture Fraction Structure

For the desired gradient-trajectory-based reconstruction of mixture fraction statistics, the gradient trajectories need to be properly parametrized. For this purpose, Peters & Truoillet [97] proposed the previously investigated $Z_{\rm m}$ and ΔZ on these points. A model for the scalar structure between these extremal

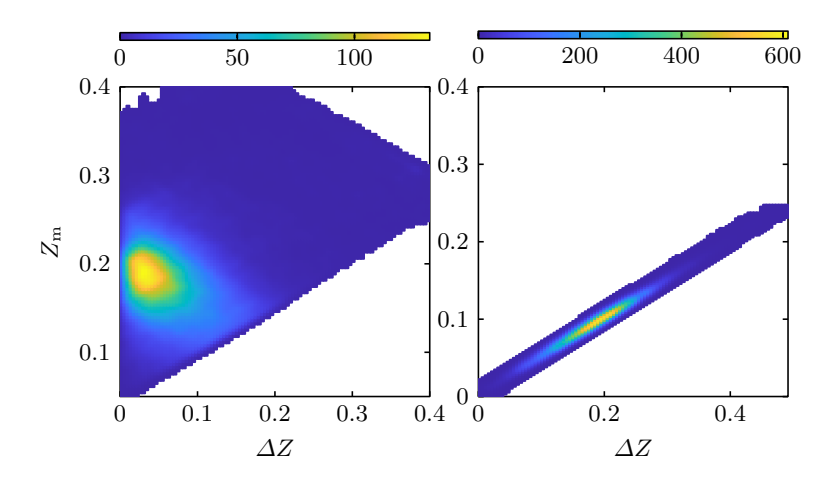


Figure 7.7: JPDF of the DE parameters conditioned on turbulent core region (left) and TNTI region (right) in the Inert Jet case.

points was then proposed as

$$Z(s) = \frac{\Delta Z}{2} \sin(\pi s - \pi/2) + Z_{\rm m},$$
 (7.18)

were s is the arc-length distance of the gradient trajectory from the minimum. The results of the model for Z(s) are compared to results from the three DNS cases. To this end, the normalized mixture fraction $Z^* = (Z - Z_{\min})/\Delta Z$ is conditioned on the normalized arc-length $s^* = s/s_{\max}$, with the total arc length s_{\max} from the minimum to the maximum. In Fig. 7.8 the conditional mean $\langle Z^* | s^* \rangle$ is shown for the turbulent core regions of the three DNS cases, and a passive scalar field obtained from DNS of isotropic turbulence 20. The normalized mixture fraction shows a perfect collapse for all cases and displays a symmetric shape. Furthermore, the presence of heat release, variable density, and viscosity does not affect the small scale structure of the mixture fraction and the proposed analytic model is a very good fit of the DNS data.

Using this model for the scalar profile Z(s), the conditional model PDF $P(Z|Z_{\rm m},\Delta Z)$ can be derived \P as

$$P(Z|Z_{\rm m}, \Delta Z) = \frac{T^{-1}}{|\partial Z/\partial s|} = \frac{\pi^{-1}}{|(Z - Z_{\rm m} + \Delta Z/2)^{1/2}(Z_{\rm m} + \Delta Z/2 - Z)^{1/2}|},$$
(7.19)

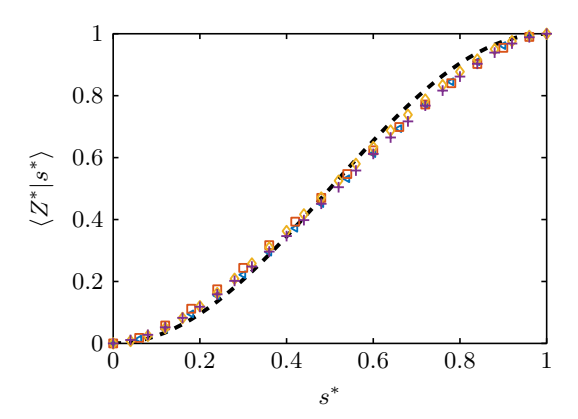


Figure 7.8: Mean normalized mixture fraction conditioned on the normalized arclength $\langle Z^*|s^*\rangle$ in the turbulent core. (a): Isotropic Turbulence, (b): Mixing Layer, (c): Jet Flame, (b): Inert Jet, (--): model.

where P(s) is uniform. Finally, the zonal PDF P_i can be reconstructed by convoluting the conditional model PDF with the JPDF of the DE parameters

$$P_i(Z) = \int_0^1 \int_0^{\Delta Z_{\text{max}}} P(Z|Z_{\text{m}}, \Delta Z) P_i(Z_{\text{m}}, \Delta Z) d\Delta Z dZ_{\text{m}}$$
 (7.20)

The results of the reconstruction procedure are shown in Fig. [7.9]. For all cases, excellent results in the turbulent core region and the overall flow are achieved. The reconstructed PDF in the TNTI region reproduces the DNS well for large to intermediate values of Z. For smaller values of Z, $P_{\rm TNT}(Z)$ qualitatively matches the DNS results. Keeping in mind that the model for Z(s) employed was obtained to match the turbulent core region, the deviations from the DNS cases are acceptable.

7.2.3 DE Based Modeling Approach

In this section, the original proposed composite PDF [46] is modified using the previously introduced PDF reconstruction and exploiting other characteristics of DE parameter statistics with the result of reducing the required input. The composite PDF $P_{\rm DE}$ is defined as

$$P_{\rm DE}(Z) = (1 - \gamma)\delta(Z) + \gamma \left[\gamma_{\rm t} P_{\rm TC}(Z) + (1 - \gamma_{\rm t}) P_{\rm TNT}(Z) \right],$$
 (7.21)

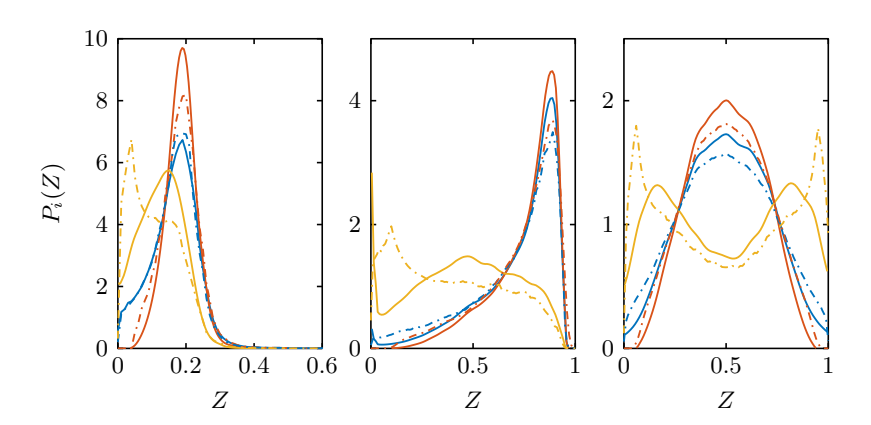


Figure 7.9: Modelling results of the zonal PDFs $P_i(Z)$ employing the joint DE statistics obtained from DNS. The turbulent core region PDF $P_{\text{TC}}(Z)$, the TNTI region PDF $P_{\text{TNT}}(Z)$, and the combined regions are indicated by the red, yellow and blue lines, respectively. The solid lines indicate P(Z) obtained directly from DNS and the dashed lines correspond to the model. Left: Inert Jet, middle: Jet Flame and right: Mixing Layer.

with the intermittency factor γ as defined by Townsend [118] and the dirac function $\delta(Z)$ representing the laminar part of the flow. The turbulent intermittency factor $\gamma_{\rm t}$ is analogous to γ and signifies the probability of encountering turbulent core in the turbulent region. $P_{\rm TC}(Z)$ and $P_{\rm TNT}(Z)$ are the previously analysed zonal PDFs.

As shown in the previously, $P_i(Z)$ can be successfully reconstructed if the zonal JPDFs $P_{\text{TC}}(Z_{\text{m}}, \Delta Z)$ and $P_{\text{TNT}}(Z_{\text{m}}, \Delta Z)$ are available. For the former, the universal shape of the PDF of the normalized scalar difference $P(\Delta Z^*)$ is exploited. This universality is demonstrated in Fig. 7.10 (left), where the PDFs show a perfect agreement across the different flows. The slight deviation in the tails for large ΔZ^* can be attributed to the boundedness of Z. The statistical independence of the two DE parameters is demonstrated on the right of Fig. 7.10 (right), where $P(\Delta Z^*)$ is additionally conditioned on Z_{m} in the Mixing Layer leading to essentially the same distributions for all values of Z_{m} . Consequently, the JPDF in the turbulent core can be modeled as

$$P_{\rm TC}(Z_{\rm m}, \Delta Z) = P(Z_{\rm m})P(\Delta Z^*)\overline{\Delta Z}$$
. (7.22)

Exploiting Kolmogorov's theoretical scaling for the first oder scalar structure

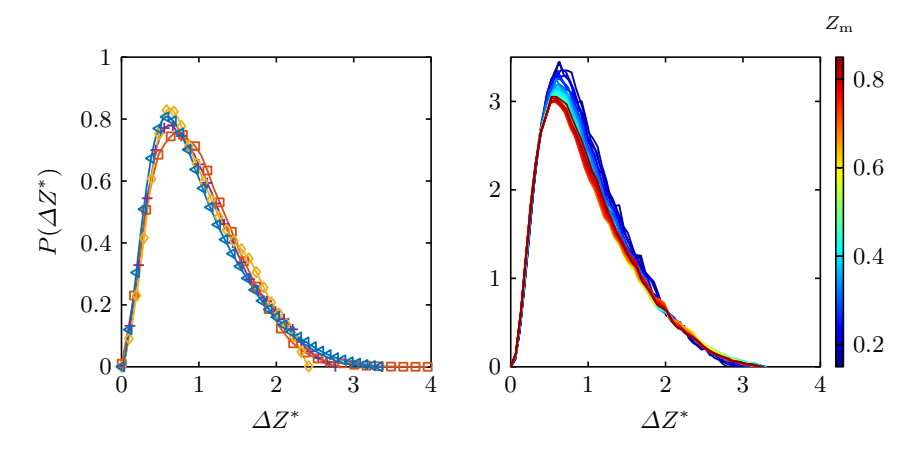


Figure 7.10: Left: PDF of the normalized scalar difference $P(\Delta Z^*)$. (\blacksquare): Mixing Layer, (\blacksquare): Jet Flame, (\blacksquare): Inert Jet, and (\blacksquare): Isotropic turbulence. Right: normalized PDF of the scalar difference conditioned on arithmetic mean $P(\Delta Z^*|Z_{\rm m})$ in the Mixing Layer.

function $\boxed{127}$, $\overline{\Delta Z}$ can be calculated as

$$\overline{\Delta Z} \approx 2.4 \frac{\overline{\chi}^{1/2}}{\overline{\varepsilon}^{1/6}} \overline{\ell}^{1/3} \,. \tag{7.23}$$

Both $P(\Delta Z^*)$ can be obtained either by solving stochastic transport eqs. (7.4) and (7.7), or exploiting the universal shape of the PDFs, obtained directly from a DE analysis of a passive scalar field. For the following results, $P(\Delta Z^*)$ was obtained from isotropic turbulence. The mean DE length $\bar{\ell}$ can be calculated exploiting its scaling with the Kolmogorov micro scale $\bar{\ell} \approx 30\eta$, c.f. Fig. 5.3 $| \cdot \rangle$.

Considering the rather deterministic nature in the TNTI region, and in good accordance with the JPDFs in Fig. 7.7, $P_{\text{TNT}}(Z_{\text{m}}, \Delta Z)$ is modeled using a dirac function for the relation between Z_{m} and ΔZ to represent the gradient trajectories proceeding indefinitely into the laminar region of the flow

$$P_{\text{TNT}}(Z_{\text{m}}, \Delta Z) = P(Z_{\text{m}})\delta(\Delta Z - Z_{\text{m}}/2). \tag{7.24}$$

Finally, the marginal PDF $P(\Delta Z_{\rm m})$ is modeled analogously for both zones to the original approach using a beta function 46 with the mean and variance of Z in the turbulent region of the flow.

$$P(Z_{\rm m}) = P_{\beta}(Z|\overline{Z}_{\rm t}, \alpha \overline{Z'^2}_{\rm t}). \tag{7.25}$$

Using the intermittency factor γ , which can be calculated following Townsend [118] or obtained exploiting its self-similar shape of the TNTI [11], \overline{Z}_t and Z'^2_t can be calculated following Pope [104] as

$$\overline{Z}_{\rm t} = \overline{Z}/\gamma \,,$$
 (7.26)

$$\overline{Z'^{2}}_{t} = \frac{\overline{Z'^{2}} - \gamma(1 - \gamma)\overline{Z}_{t}^{2}}{\gamma}.$$
(7.27)

Conveniently, due to the symmetry of Z(s), the mean arithmetic mean is equivalent to the mean mixture fraction $\overline{Z}_{\rm m} = \overline{Z}_{\rm t}$. However, α needs to be determined iteratively to assure that the variance generated by $\gamma_{\rm t} P_{\rm TC}(Z) + (1 - \gamma_{\rm t}) P_{\rm TC}(Z)$ matches $\overline{Z'^2}_{\rm t}$.

Lastly, it was found for the investigated cases that $\gamma_t = \gamma$ is a reasonable simplification which also captures the trends in the experimental investigation of the original composite PDF [54]. This is sensible, as in the fully turbulent core for $\gamma = 1$ little to no TNTI contributions to the overall statistics are expected. Vice versa, for low values of γ , high probabilities of encountering the TNTI would cause γ_t to be low as well.

7.2.4 Model Validation and Discussion

The results of the DE statistic-based model $P_{\rm DE}(Z)$ are compared to the DNS P(Z) and the conventional $P_{\beta}(Z)$ in Fig. 7.11 For both jet cases, $P_{\rm DE}(Z)$ displays superior results which capture all important trends present in P(Z). In cross-stream positions far away from the core flow, $P_{\rm DE}(Z)$ manages to reproduce the influence of the TNTI layer on the Z statistics. Additionally, in the core region of the Jet Flame, where the beta PDF is expected to perform well, P(Z) is also matched better by the DE statistics-based model. Another characteristic feature which is correctly reproduced by $P_{\rm DE}(Z)$ is the non-marching behavior of the PDF of the Inert Jet. The benefits of the increased accuracy of $P_{\rm DE}(Z)$ is demonstrated for the Jet Flame in Fig. 7.12, where the modelled mean density

$$\overline{\rho} = \int_{0}^{1} P(Z)\rho(Z, \overline{\chi_{st}}) dZ, \qquad (7.28)$$

with $\rho(Z, \overline{\chi_{\rm st}})$ obtained from the steady state flamelet solution matching the boundary conditions of the DNS, is compared for the two model approaches. $\overline{\rho}$ modelled with $P_{\rm DE}(Z)$ matches the DNS far better in almost all cross-stream

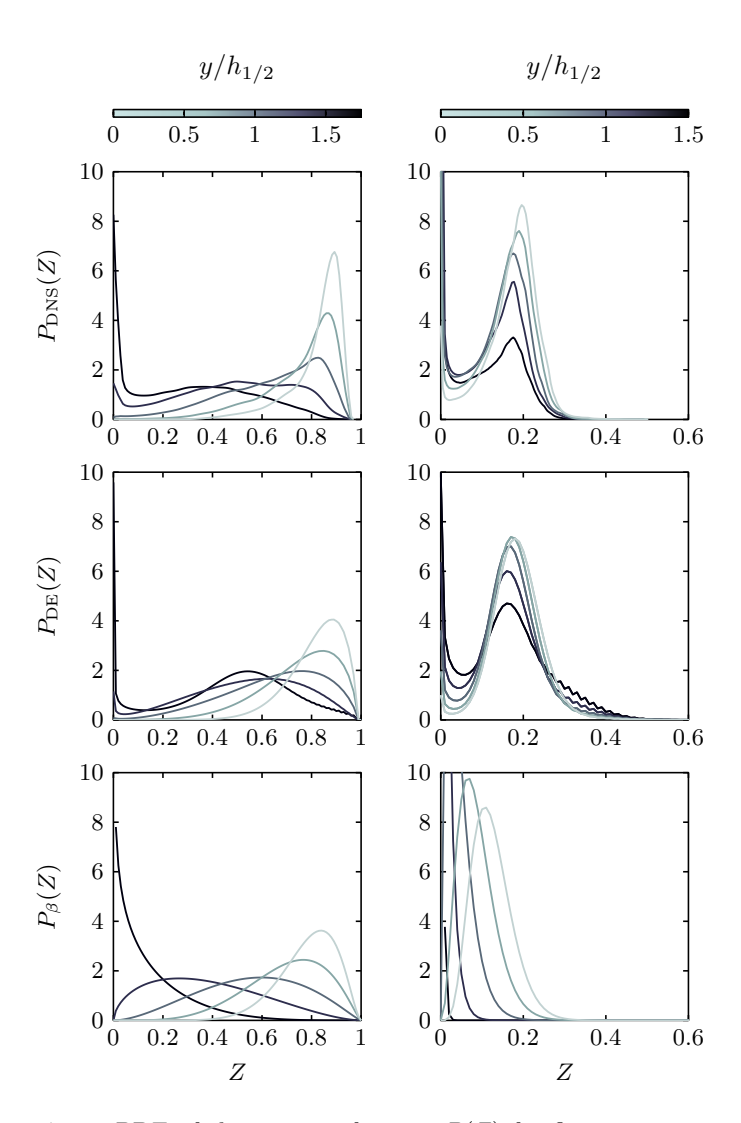


Figure 7.11: PDF of the mixture fraction P(Z) for five cross-stream positions $y/h_{1/2}$, with the jet half width $h_{1/2}$, for the Jet Flame (left) and Inert Jet (right).

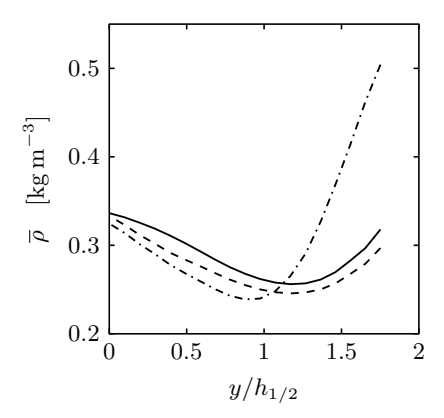


Figure 7.12: Mean density $\overline{\rho}$ obtained from the convolution of P(Z) with a steady state flamelet solution for the Jet Flame. (Solid line): $P_{\text{DNS}}(Z)$, (dashed line): $P_{\text{DE}}(Z)$, and (dash-dotted line): $P_{\text{fl}}(Z)$.

positions. Especially at the jet edges, $P_{\rm DE}(Z)$ is superior. The model might be easily improved by exchanging the sine-function model for Z(s) for empirically obtained conditional means of $\langle Z|s\rangle$ at the TNTI, which are readily available in literature. Here, we refrained from this practice to retain the general applicability to any RANS simulation which solves \overline{Z} and $\overline{Z'^2}$. Regardless, the flexibility that the model offers could be deemed another advantage.

8 Summary and Conclusion

In the first part of this thesis, dissipation element (DE) analysis was applied to the mixture fraction fields and passive scalar fields of six non-premixed reacting and inert direct numerical simulations (DNS) of the temporally evolving jet configuration. The statistics of the normalized DE parameter ℓ^* showed the characteristic invariance towards changes in Reynolds numbers and was unaffected by the heat release in the reacting cases. The mean DE length ℓ_m was found to scale with the Kolmogorov micro scale. The effect of the heat release on the DE scalar difference ΔZ was observed with an increased probability of cliff-ramp structures in the mixture fraction field. However, the effect of the heat release on the statistics decreased with an increasing dilution of the fuel stream and with an increase in the Reynolds number. The joint probability density function (JPDF) of the two normalized DE parameters obtained from the highest Reynolds number reacting case displayed the universal form observed in the non-reacting cases. DE parameter statistics were related to structure functions and the correlation between the DE gradient g and the scalar dissipation rate χ was demonstrated. This correlation allows for the reconstruction of the DE parameter statistics from the value of the unconditional scalar dissipation rate.

Additionally, a DE parameter-based regime diagram was introduced. The DE parameters g and ΔZ were compared to flame scales with the quenching gradient $g_{\rm q}$ and the reaction zone thickness $\delta Z_{\rm r}$ for a local classification of the flame front into four regimes. The regime assumptions were tested using the correlation between DE parameters and reacting scalars on a non-dimensional basis. The soundness of the regime diagram was shown for all four reacting cases. Below the regime threshold value of $\Delta Z \leq (\Delta Z)_{\rm t} = 15\delta Z_{\rm r}$ the model assumptions of a 1D flamelet cease to be valid as the reacting scalars display gradients in the tangential direction to the flamelet coordinates in physical space. Above this threshold value, the local conditional fluctuations of the reacting scalars are small, irrespective of the value of dissipation rate.

In the second part of this thesis, DE analysis was performed on the temperature fields of the DNS of three spatially evolving methane jet flames. Statistics of DE parameters were compared to those obtained from passive scalar fields of non-reacting flows including isotropic turbulence, a spatially evolving jet, and a temporally evolving jet to isolate individual effects of the reacting scalar on the DE statistics. It was found that the DE length $\ell_{\rm m},$ was doubled in the temperature field compared to the passive scalar fields when normalized with the Kolmogorov micro-scale $\eta.$ However, the invariance of the normalized statistics of $\ell_{\rm m}$ toward changes in the Reynolds number observed in scalar fields in non-reacting flows was retained in the reacting cases. Substantial differences in the statistics of the DE scalar difference ΔT and $\Delta \phi$ between the premixed reacting and the spatially evolving cases were observed, which could be attributed to the imprint of the premixed flame structure. The marginal and joint statistics showed a high consistency with the assumptions regarding the general setup of the reacting DNS and the regime of the thin reaction zones, with $\ell_{\rm m}$ at least an order of magnitude higher than the flame thickness.

In a detailed investigation of the flame structure, it was shown that the scalar difference ΔT between the extremal points of DEs consistently parameterizes both the temperature in the preheating zone and a reduction of the temperature gradients in the entire flame structure. The analysis shows that the lower gradients in the inner reaction layer are linked to the presence of extremal points in the vicinity of the flame surface; therefore, they lead to the interruption of the flamelet structure by turbulence and not by the thickening of the entire flamelet itself. The trend of decreasing ΔT with an increasing Reynolds number was shown by means of the JPDF of DE parameters normalized by the flamelet scales. This suggests that the increased thickening for an increasing integral scale and Reynolds number at approximately constant turbulent intensity and Karlovitz number is linked to the increased presence of turbulence-induced extremal points near and inside the inner reactive layer of the flame.

As expected, species such as formal dehyde, which are usually present in the preheat layer of laminar flames experience a significantly enhanced transport. However, even species such as OH and O, which are usually negligible in the preheat layer are present in a significant amount several flame thicknesses ahead of the turbulent flame surface when the DE parameter ΔT is small.

The analysis of the integrated fuel consumption rate along the gradient trajectories revealed that for regions with small ΔT , which correspond to thickened flame sections, the local fuel consumption rate decreases with respect to the flamelet solution. However, due to the thickening of the reaction layer, the integral over the thickened flame is larger than that in the unthickened flamelet, explaining an overall increase of the turbulent flame speed.

This work is concluded with the application of the insight gained through the DE analysis of the turbulent combustion to model both the scale interaction

between the turbulence and combustion as well as the scalar structure itself.

The previously introduced concept of a regime diagram for turbulent non-premixed combustion based on DE parameters was used to apply the insight gained from DNS to the computational fluid simulation of a real-world passenger car direct injection diesel engine. The universality of the statistics of the normalized DE parameters obtained from passive scalar fields in combination with the characteristic scaling of the mean DE parameters was exploited in a modelling framework. This framework relies on quantities readily available in CFD simulations utilizing mixture fraction-based combustion models. With the insight gained from the combustion regime boundaries from DNS, the probability of encountering the individual regimes in a diesel engine could be predicted. The modelling framework was applied to CFD simulations of a passenger car diesel engine in various operation points. The results yielded were highly plausible with a classification of the combustion processes as largely flamelet-like. However, in the early combustion phases, as well as in low load operation points, small scale combustion might dominate.

Futhermore, a DE statistic-based extension of the composite PDF model for the mixture fraction Z from Effelsberg & Peters [46] was proposed. The zonal decomposition of free shear flows and the reconstruction of the mixture fraction PDF by means of gradient trajetories was demonstrated with three inert and reacting DNS datasets. The DE statistics-based model was derived and model assumptions in the model equations were justified by the DE analysis of the three DNS cases. Finally, the results of the novel model procedure were compared to the DNS and a conventional beta PDF model. The DE statistic based model showed satisfactory results when compared to the DNS and is vastly superior in all flow regions compared to the beta PDF approach due to the consideration of the different flow regimes.

In conclusion, this thesis demonstrated the importance of transcending the conventionally used one-point statistics to comprehend the complex interaction of turbulence and combustion chemistry featured in the investigated configurations. As structures of finite sizes interact at the presented combustion conditions, it appears only logical that the conventionally considered flame structure as well as a robustly defined turbulent structure must be reflected in the method of analysis. In this regard, the DE analysis proved invaluable in providing said turbulent structures in a non-arbitrary and well parametrized way, which allowed for an intuitive and straight forward physical interpretation of the results.

Another important aspect of the present thesis was shifting the perspective of the investigation from a purely statistical approach using global, quantities to a more local analysis. By retaining the information of the topological features of the instantaneous scalar fields in the analysis, new physical mechanisms were considered which would have otherwise been lost due to the averaging procedure.

Lastly, the demonstrated universality of the DE parameter statistics are a reason for optimism with regards to the certainty of directly applying the knowledge of turbulence gained through the investigation of non-reacting flows (and of course, theoretical considerations) onto reacting flows. The presented DE parameter statistic based models exploiting these universalities will hopefully only be the start and inspire others to further pursue modeling approaches in this spirit.

Bibliography

- [1] R. A. Antonia and P. Burattini. "Approach to the 4/5 law in homogeneous isotropic turbulence". In: *J. Fluid Mech.* 550 (2006), pp. 175–184.
- [2] R. A. Antonia and K. R. Sreenivasan. "Log-normality of Temperature Dissipation in a Turbulent Boundary Layer". In: *Phys. Fluids* 20 (1977), pp. 1800–1804.
- [3] A. Antonio, S. Luca, D. Denker, F. Bisetti, and H. Pitsch. "Turbulent flame speed and reaction layer thickening in premixed jet flames at constant Karlovitz and increasing Reynolds numbers". In: *Proc. Comb. Inst.* (2020).
- [4] A.J. Aspden, M.S. Day, and J.B. Bell. "Lewis number effects in distributed flames". In: *Proceedings of the Combustion Institute* 33.1 (2011), pp. 1473 –1480.
- [5] A. Attili and F. Bisetti. "Fluctuations of a passive scalar in a turbulent mixing layer". In: *Phys. Rev. E* 3 (2013), p. 03301.
- [6] A. Attili and F. Bisetti. "Statistics of Scalar Dissipation and Strain / Vorticity / Scalar Gradient Alignment in Turbulent Nonpremixed Jet Flames". In: Flow, Turbulence and Combustion 103.3 (2019), pp. 625–642.
- [7] A. Attili, J. C. Cristancho, and F. Bisetti. "Statistics of the turbulent/non-turbulent interface in a spatially developing mixing layer". In: *Journal of Turbulence* 15.9 (Sept. 2014), pp. 555–568.
- [8] A. Attili, F. Bisetti, M. E. Mueller, and H. Pitsch. "Damköhler number effects on soot formation and growth in turbulent nonpremixed flames". In: Proceedings of the Combustion Institute 35 (2015), pp. 1215–1223.
- [9] A. Attili, F. Bisetti, M. Mueller, and H. Pitsch. "Effects of non-unity Lewis number of gas-phase species in turbulent nonpremixed sooting flames". In: *Comb. and Flame* 166 (2016), pp. 192–202.
- [10] A. Attili, F. Bisetti, M. E. Mueller, and H. Pitsch. "Effects of non-unity Lewis number of gas-phase species in turbulent nonpremixed sooting flames". In: *Combustion and Flame* 166 (2016), pp. 192–202.

- [11] A. Attili, F. Bisetti, M. E. Mueller, and H. Pitsch. "Formation, growth, and transport of soot in a three-dimensional turbulent non-premixed jet flame". In: *Combust. Flame* 161 (2014), pp. 1849–1865.
- [12] A. Attili, S. Luca, D. Denker, F. Bisetti, and H. Pitsch. "Turbulent flame speed and reaction layer thickening in premixed jet flames at constant Karlovitz and increasing Reynolds numbers". In: *Proc. Comb. Institute* (2020).
- [13] B. Ayoolan, R. Balachandran, E. Mastorakos J.Frank and, and C. Kaminski. "Spatially resolved heat release rate measurements in turbulent premixed flames". In: *Comb and Flame* 144 (2006), pp. 1–16.
- [14] B. Bédat, F. N E., and T. Poinsot. "Direct numerical simulation of heat release and NOx formation in turbulent nonpremixed flames". In: Combustion and Flame 119.1 (1999), pp. 69 –83.
- [15] R. W. Bilger. "The structure of diffusion flames". In: Combust. Sci. and Tech. 13 (1976), pp. 155–170.
- [16] R.W. Bilger, S. B. Pope, K. N. C. Bray, and J. F. Driscoll. "Paradigms in turbulent combustion research". In: *Proc. Combust. Inst.* 30 (2005), pp. 21–42.
- [17] D. K. Bisset, J. C. R. Hunt, and M. M. Rogers. "The turbulent/non-turbulent interface bounding a far wake". In: *J. Fluid Mech.* 451 (2002), pp. 383–410.
- [18] M. Bode, M. Gauding, Z. Lian, D. Denker, M. Davidovic, K. Kleinheinz, J. Jitsev, and H. Pitsch. "Using Physics-Informed Super-Resolution Generative Adversarial Networks for Subgrid Modeling in Turbulent Reactive Flows". In: Proc. Comb. Inst. (2020).
- [19] R. W. Borghi. "On the structure and morphology of turbulent premixed flames". In: *Recent Advances in the Aoerospace Science* (1985), pp. 117–138.
- [20] J. Boschung, F. Hennig, D. Denker, H. Pitsch, and R. J. Hill. "Analysis of structure function equations up to the seventh order". In: *J. Turbul.* (2017), pp. 1–32.
- [21] J. Boschung, M. Guading, F. Hennig, D. Denker, H. Pitsch, and R. J. Hill. "Finite Reynolds number corrections to the 4/5-law for decaying turbulence". In: *Phys. Rev. Fluids* 1.064403 (2016).

- [22] J. Boschung, F. Hennig, M. Gauding, H. Pitsch, and N. Peters. "Generalized higher-order Kolmogorov scales". In: J. Fluid Mech. 794 (2016), pp. 233–251.
- [23] K. N. C. Bray and J. B. Moss. "A unified statistical model of the premixed turbulent flame". In: *Acta Astronautica* 4 (1977), pp. 291–319.
- [24] K. N. C. Bray and N. Peters. "Laminar flamelets in turbulent flames". In: *Turbulent Reacting Flows*. Ed. by P. A. Libby and F. A. Williams. Academic Press, 1994, p. 1994.
- [25] J. E. Broadwell and R. E. Breidenthal. "A simple model for mixing and chemical reaction in a turbulent shear layer". In: *J. Fluid Mech.* 125 (1982), pp. 397–410.
- [26] L. G. Brown and A. Roshko. "On density effects and large structure in turbulent mixing layers". In: *J. Fluid Mech.* 64 (1974), pp. 775–816.
- [27] P. N. Brown, G. D. Bryne, A. C. Hindmarsh, and Vode. "A Variable Coefficient ODE Solver". In: SIAM J. Sci. Stat. Comput. 10 (1989), pp. 1038–1051.
- [28] S. P. Burke and T. E. W. Schumann. "Diffusion Flames". In: First Symposium (International) on Combustion (1928), pp. 2–11.
- [29] A. Celani, M. Cencini, M. Vergassola, E. Villermaux, and D. Vincenzi. "Shear effects on passive scalar spectra". In: *J. Fluid Mech.* 523 (2005), pp. 99–108.
- [30] N. Chakraborty, M. Klein, and N. Swaminathan. "Effects of Lewis number on the reactive scalar gradient alignment with local strain rate in turbulent premixed flames". In: *Proceedings of the Combustion Institute* 32.1 (2009), pp. 1409–1417.
- [31] N. Chakraborty and N. Swaminathan. "Influence of the Damköhler number on turbulence-scalar interaction in premixed flames. I. Physical insight". In: *Physics of Fluids* 19.4 (2007), p. 045103.
- [32] Nilanjan Chakraborty and Stewart Cant. "Unsteady effects of strain rate and curvature on turbulent premixed flames in an inflow-outflow configuration". In: *Combustion and flame* 137.1-2 (2004), pp. 129–147.
- [33] M. S. Chong, A. E. Perry, and B. Cantwell. "The General classification of three dimensional flow fields". In: *Phys. Fluids A* 2 (1990), pp. 408–420.

- [34] A Cook, W. Cabot, and P. Miller. "The mixing transition in Rayleigh—Taylor instability". In: *J. Fluid Mech.* 511 (2004), pp. 333–362.
- [35] S. Corrsin. "Random geometric problems suggested by turbulence". In: Statistical Models and Turbulence. Ed. by M. Rosenblatt and C. van Atta. Vol. 12. Lecture Notes in Physics. Springer Verlag, 1971, pp. 300–316.
- [36] J. Crank and P. Nicolson. "A practical method for numerical evaluation of solutions of partial differential equations of the heat-conduction type". In: Advances in Computational Mathematics. Vol. 6. 1. Springer, 1996. Chap. 207-226.
- [37] D. D'acunto and K. Kurdyka. "Bounds for gradient trajectories and geodesic diameter of real algebraic sets". In: *Bull. London math. Soc.* 38 (2006), pp. 951–968.
- [38] D. Denker, A. Attili, and H. Pitsch. "Dissipation Element Analysis of Inert and Reacting Turbulent Flows". In: *Data Analysis for Direct Numerical Simulations of Turbulent Combustion*. Ed. by H. Pitsch and A. Attili. Springer International Publishing, 2020. Chap. 2, pp. 19–41.
- [39] D. Denker, A. Attili, M. Bode, M. Gauding, and H. Pitsch. "A New Modeling Approach for Mixture Fraction Statistics Based on Dissipation Elements". In: *Proc. Comb. Inst* (2020).
- [40] D. Denker, A. Attili, J. Boschung, F. Hennig, M. Gauding, M. Bode, and H. Pitsch. "Dissipation Element Analysis of Non-premixed Jet Flames". In: J. Fluid Mech. 905 (2020), A4.
- [41] D. Denker, A. Attili, S. Luca, M. Gauding, F. Bisetti, and H. Pitsch. "Dissipation element analysis of premixed jet flames". In: Comb. Sci. Tech. 191.9 (2019), pp. 1677–1683.
- [42] D. Denker, A. Attili, K. Kleinheinz, and H. Pitsch. "Gradient Trajectory Analysis of the Burning Rate in Turbulent Premixed Jet Flames". In: Comb. Sc. and Tech. 192.11 (2020), pp. 2189–2207.
- [43] O. Desjardins, G. Blanquart, G. Balarac, and H. Pitsch. "High Order Conservative Finite Difference Scheme for Variable Density Low Mach Number Turbulent Flows". In: J. Comp. Phys. 227 (2008), pp. 7125–7159.
- [44] J. F. Driscoll, J. H. Chen, A. W. Skiba, C. D. Carter, E. R. Hawkes, and H. Wang. "Premixed flames subjected to extreme turbulence: Some questions and recent answers". In: *Prog. Energ. Combust. Sci.* 76 (2020), p. 100802.

- [45] M. J. Dunn, A. R. Masri, and R. W. Bilger. "A new piloted premixed jet burner to study strong finite-rate chemistry effects". In: *Combustion and Flame* 151.1 (2007), pp. 46–60.
- [46] E. Effelsberg and N. Peters. "A composite model for the conserved scalar pdf". In: *Combust. Flame* 50 (1983), pp. 351–360.
- [47] R. D. Falgout, J. E. Jones, and U. M. Yang. "Pursuing Scalability for hypre's Conceptual Interfaces". In: ACM Transactions on Mathematical Software 31 (2005).
- [48] V. Favier and L. Vervisch. "Edge flames and partially premixed combustion in diffusion flame quenching". In: *Combust. Flame* 125 (2001), pp. 788–803.
- [49] Y. Feng and M. R. Krumholz. "Early turbulent mixing as the origin of chemical homogeneity in open star clusters". In: *Nature* 513.7519 (2014), pp. 523–525.
- [50] L. De Floriani and M. Spangnuolo, eds. Shape Analysis and Structuring. Springer, 2007.
- [51] R. O. Fox. Computational Models for Turbulent Reacing Flows. Cambridge University Press, 2003.
- [52] M. Gampert, P. Schaefer, and N. Peters. "Experimental investigation of dissipation-element statistics in scalar fields in a jet flow". In: *J. Fluid Mech.* 724 (2013), pp. 337–366.
- [53] M. Gampert, P. Schaefer, J.H. Goebbert, and N. Peters. "Decomposition of the field of the turbulent kinetic energy into regions of compressive and extensive strain". In: *Physica Scripta* 155.014002 (2013).
- [54] M. Gampert, K. Kleinheinz, N. Peters, and H. Pitsch. "Experimental and Numerical Study of the Scalar Turbulent/Non-Turbulent Interface in a Jet Flow". In: Flow Turbulence Combust. 92 (2014), pp. 429–449.
- [55] M. Gampert, J. H. Goebbert, P. Schaefer, M. Gauding, N. Peters, F. Aldudak, and M. Oberlack. "Extensive strain along gradient trajectories in the turbulent kinetic energy field". In: New J. of Phys. 13 (2011), p. 043012.
- [56] M. Gampert, P. Schäfer, V. Narayanaswamy, and N. Peters. "Gradient trajectory analysis in a jet flow for turbulent combustion modeling". In: J. Turbul. 14 (2013), pp. 147–164.

- [57] M. Gauding. "Statistics and Scaling Laws of Turbulent Scalar Mixing at High Reynolds Numbers". PhD thesis. RWTH Aachen University, 2014.
- [58] M. Gauding, F. Dietzsch, J.H. Goebbert, D. Thévenin, A. Abdelsamie, and C Hasse. "Dissipation element analysis of a turbulent non-premixed jet flame". In: *Phys. Fluids* 29.085103 (2017).
- [59] M. Gauding, D. Denker, Y. Brahami, M. Bode, L. Danaila, and E. Varea. "On the combined effect of internal and external intermittency in turbulent non-premixed jet flames". In: Proc. Comb. Inst. (2020).
- [60] J. H. Göbbert, H. Iliev, C. Ansorge, and H. Pitsch. "Overlapping of Communication and Computation in nb3dfft for 3D Fast Fourier Transformations". In: *High-Performance Scientific Computing*. Ed. by Edoardo Di Napoli, Marc-André Hermanns, Hristo Iliev, Andreas Lintermann, and Alexander Peyser. Cham: Springer International Publishing, 2017, pp. 151–159. ISBN: 978-3-319-53862-4.
- [61] E. R. Hawkes and R. S. Cant. "A flame surface density approach to large-eddy simulation of premixed turbulent combustion". In: Proceedings of the Combustion Institute 28.1 (2000), pp. 51–58.
- [62] E. R. Hawkes, R. Sankaran, J. C. Sutherland, and J. H. Chen. "Scalar mixing in direct numerical simulations of temporally evolving plane jet flames with skeletal CO/H2 kinetics". In: *Proc. Combust. Inst.* 31 (2007), pp. 1633–1640.
- [63] F. Higuera and R. D. Moser. "Effect of chemical heat release in a temporally evolving mixing layer". In: *In Studying Turbulence Using Numerical Databases* V (1994), pp. 19–40.
- [64] J. O. Hirschfelder and C. F. Curtis. "Flame prpagation in explosive gas mixtures". In: *Third Symposium (International) om Combustion*. Reinhold, New York, 1949, pp. 121–127.
- [65] M. Holzer and E. D. Siggia. "Turbulent mixing of a passive scalar". In: Phys. Fluids 6 (1994), pp. 1820–1837.
- [66] F. Hunger, M. Gauding, and C. Hasse. "On the impact of the turbulent/non-turbulent interface on differential diffusion in a turbulent jet flow". In: J. Fluid Mech. 802 (2016).
- [67] International Energy Outlook 2019. U.S. Energy Information Administration, 2019.

- [68] G. S. Jiang and C. W Shu. "Efficient implementation of weighted ENO schemes". In: *J. Comput. Phys.* 126 (1996), pp. 202–228.
- [69] B. Jochim, M. Korkmaz, and H. Pitsch. "Scalar dissipation rate based multi-zone model for early-injected and conventional diesel engine combustion". In: Comb. and Flame 000 (2016), pp. 1–17.
- [70] J. Kim and P. Moin. "Application of a fractional-step method to incompressible Navier-Stokes equations". In: *Journal of Computational Physics* 59.2 (1985), pp. 308 –323.
- [71] W. Kollman and J. Janicka. "The probability density function of a passive scalar in turbulent shear flows". In: *Phys. Fluids* 25 (1982), pp. 1755–1769.
- [72] A. N. Kolmogorov. "Dissipation of energy under locally isotropic turbulence". In: *Dokl. Akad. Nauk SSSR* 32 (1941), pp. 16–18.
- [73] A. N. Kolmogorov. "The local structure of turbulence in an incompressible viscous fluid for very large Reynolds numbers". In: *Dokl. Akad. Nauk SSSR* 30 (1941), pp. 301–305.
- [74] R. H. Kraichnan. "Convection of passive scalar by quasi-uniform random straining field". In: *J. Fluid Mech.* 64.737-762 (1974).
- [75] P. A. Krogstad and P. Davidson. "Freely-decaying, homogenous turbulence generated by multy-scale grids". In: J. Fluid Mech 680 (2011), pp. 417–434.
- [76] A. Kronenburg and R. W. Bilger. "Modelling Differential Diffusion in Nonpremixed Reacting Turbulent Flow: Model Development". In: Combustion Science and Technology 166.1 (2001), pp. 195–227.
- [77] S. Kullback and R. A. Leibler. "On information and sufficiency". In: *Annals of Mathematical Statistics* 1 (1951), pp. 79–86.
- [78] G. A. Lavoie, J. B. Heywood, and J. C. . Keck. "Experimental and Theoretical Study of Nitric Oxide Formation in Internal Combustion Engines". In: *Combust. Sci. Tech* 1 (1970).
- [79] S.K. Lele. "Compact finite difference schemes with spectral-like resolution". In: *Phys. Fluids* 103 (1992), pp. 16–42.
- [80] D. O. Lignell, J. H. Chen, and H. A. Schmutz. "Effects of Damköhler number on flame extinction and reignition in turbulent non-premixed flames using DNS". In: Combustion and Flame 158.5 (2011), pp. 949 –963.

- [81] Z. Lu and S. Ghosal. "Flame holes and flame disks on the surface of a diffusion flame". In: *J. Fluid Mech* 513 (2004).
- [82] S. Luca, A. N. Al-Khateeb, A. Attili, and F. Bisetti. "Comprehensive Validation of Skeletal Mechanism for Turbulent Premixed Methane—Air Flame Simulations". In: J. Propulsion Power 34.1 (2018), pp. 153–160.
- [83] S. Luca, A. Attili, E. L. Schiavo, F. Creta, and F. Bisetti. "On the statistics of flame stretch in turbulent premixed jet flames in the thin reaction zone regime at varying Reynolds number". In: *Comb. and Flame* 37.2 (2019), pp. 2451–2459.
- [84] J. P. Mellado, L. Wang, and N. Peters. "Gradient trajectory analysis of a scalar field with external intermittency". In: J. Fluid Mech 626 (2009), pp. 333–365.
- [85] M. Oberlack and A. Rosteck. "New statistical symetries of the multipoint equations and its importance for turbulent scaling laws". In: *Discret. Cont. Dyn. Syst. S.* 3 (3) (2010), pp. 451–471.
- [86] M. A. Ol'shanskii and V. M. Staroverov. "On simulation of outflow boundary conditions in finite difference calculations for incompressible fluid". In: *International Journal for Numerical Methods in Fluids* 33 (2000).
- [87] Steven A. Orszag and G. S. Patterson. "Numerical Simulation of Three-Dimensional Homogeneous Isotropic Turbulence". In: *Phys. Rev. Lett.* 28 (2 1972), pp. 76–79.
- [88] M. R. Overholt and S. B. Pope. "Direct numerical simulation of a passive scalar with imposed mean gradient in isotropic turbulence". In: *Phys. Fluids* 8 (1996), p. 3128.
- [89] C. Pantano. "Direct simulation of non-premixed flame extinction in a methane—air jet with reduced chemistry". In: *Journal of Fluid Mechanics* 514 (2004), pp. 231–270.
- [90] C. Pantano and D.I. Pullin. "A statistical description of turbulent diffusion flame holes". In: *Comb. and Flame* 137 (2004).
- [91] N. Peters. "Combustion Theory". In: CEFRC Summer School Princeton (2010).
- [92] N. Peters. "Laminar diffusion flamelet models in non-premixed turbulent combustion". In: *Progr. Energy Combust. Sci.* 10 (1984), pp. 319– 339.

- [93] N. Peters. "Local quenching of diffusion flamelets and non-premixed turbulent combustion". In: Western States Section of the Combusiton Institute, paper WSS80-4 (1980).
- [94] N. Peters. "Multiscale Combustion and Turbulence". In: 32nd Symposium on Combustion, Montreal 2008, Proc. Combust. Inst. 32 (2009), pp. 1–25.
- [95] N. Peters. Turbulent Combustion. Cambridge University Press, 2000.
- [96] N. Peters, B. Kerschgens, and G. Paczko. "Super-Knock prediction using a refined theory of turbulence". In: *SAE* 2013-01-1109 (2013).
- [97] N. Peters and P. Trouillet. "On the role of quasi-one-dimensional dissipation layers in turbulent scalar mixing". In: Center for Turbulence Research Annual Research Briefs (2002), pp. 27–40.
- [98] N. Peters and L. Wang. "Dissipation element analysis of scalar fields in turbulence". In: C. R. Mechanique 334 (2006), pp. 493–506.
- [99] N. Peters, G. Paczko, R. Seiser, and K. Seshadri. "Temperature cross-over and non-thermal runaway at two-slage ignition at n-heplane". In: *Combust. Flame* 128 (2002), pp. 38–59.
- [100] H. Pitsch, C. M. Cha, and S. Fedotov. "Flamelet modelling of non-premixed turbulent combustion with local extinction and re-ignition".
 In: Combustion Theory and Modelling 7.2 (2003), pp. 317–332.
- [101] H. Pitsch and N. Peters. "A consistent flamelet formulation for non-premixed combustion considering differential diffusion effects". In: *Combust. Flame* 114 (1998), pp. 26–40.
- [102] A.Y. Poludnenko and E.S. Oran. "The interaction of high-speed turbulence with flames: Turbulent flame speed". In: *Combustion and Flame* 158.2 (2011), pp. 301 –326.
- [103] S. B. Pope. "Small scales, many species and the manifold challenges of turbulent combustion". In: *Proc. Combust. Inst.* 34 (2013), pp. 1–31.
- [104] S. B. Pope. Turbulent Flows. Cambridge University Press, 2000.
- [105] R. Prasad and K. R. Sreenivasan. "Scalar interfaces in digital images in turbulent flows". In: *Exp. Fluids* 7 (1983), pp. 259–264.
- [106] L.F. Richardson. Weather Prediction by Numerical Process. Cambridge University Press, 1922.
- [107] J. C. Rotta. "Turbulente Strömungen". In: *Teubner Verlag, Stuttgart* (1972).

- [108] L. Schaefer, U. Dierksheide, M. Klaas, and W. Schroeder. "Investigation of Dissipation Elements in a Fully Developed Turbulent Channel Flow by Tomographic-Particle Image Velocimetry". In: *Phys. Fluids* 23 (2011), doi:10.1063/1.3556742.
- [109] A. Schnorr, D. Helmrich, D. Denker, T. Kuhlen, and B.Hentschel. "Feature Tracking by Two-Step Optimization". In: *IEEE Transactions on Visualization and Computer Graphics* (2018).
- [110] Z. S. She and E. Orzag. "Intermittent vortex structures in homogenous isotropic turbulence". In: *Nature* 344.226-228 (1990).
- [111] A. W. Skiba, T. M. Wabel, C. D. Carter, S. D. Hammack, J. E. Temme, and J. F. Driscoll. "Premixed flames subjected to extreme levels of turbulence part I: Flame structure and a new measured regime diagram". In: *Comb. and Flame* 189 (2018), pp. 407–432.
- [112] P. Sripakagorn, G. Kosaly, and J. Riley. "Investigation of the influence of the Reynolds number on extinction and reignition". In: 136.3 (2004), pp. 351–363.
- [113] S. Stanley, S. Sarkar, and J. P Mellardo. "A study of the flowfield evolution and mixing in a planar turbulent jet using direct numerical simulation". In: *J. Fluid Mech.* 450.377-407 (2002).
- [114] G. Strang. "On the construction and comparison of difference schemes". In: SIAM J. Numer. Anal. 5 (1968), pp. 506–517.
- [115] R. R. Taveira and C. B. da Silva. "Kinetic energy budgets near the turbulent/nonturbulent interface in jets". In: *Phys. Fluids* 25 (2013).
- [116] G. I. Taylor. "Statistical Theory of Turbulence". In: Proceedings of the Royal Society of London. Mathematical and Physical Sciences 151 (1935), pp. 421–444.
- [117] A. G. Tomboulides, J. Lee, and S. A. Orszag. "Numerical simulation of low Mach number reactive flows". In: *J. Sci. Comput.* 12.2 (1997), pp. 139–167.
- [118] A. A. Townsend. "Local isotropy in the turbulent wake of a cylinder". In: Austral. J. Sci. Res. 1 (1948), pp. 161–174.
- [119] P. Trisjono and H. Pitsch. "A direct numerical simulation study on NO formation in lean premixed flames". In: *Proceedings of the Combustion Institute* 36.2 (2017), pp. 2033 –2043.
- [120] A. Tsinober. An Informal Conceptual Introduction to Turbulence. Springer Science & Business Media, 2009.

- [121] T. von Kármán and L. Howarth. "On the statistical theory of isotropic turbulence". In: *Proc. Roy. Soc. London.* A A 164 (1938), pp. 192–215.
- [122] H. Wang, E. R. Hawkes, B. Zhou, J. H. Chen, Z. Li, and M. Aldén. "A comparison between direct numerical simulation and experiment of the turbulent burning velocity-related statistics in a turbulent methane-air premixed jet flame at high Karlovitz number". In: Proceedings of the Combustion Institute 36.2 (2017), pp. 2045 –2053.
- [123] L. Wang. "Geometrical Description of Homogeneous Shear Turbulence Using Dissipation Element Analysis". PhD thesis. RWTH University, 2008.
- [124] L. Wang. "Scaling of the two-point velocity difference along scalar gradient trajectories in fluid turbulence". In: *Phys. Rev.* E 79, 046325 (2009), p. 046325.
- [125] L. Wang. "Structure function of two-point velocity difference along scalar gradient trajectories in fluid turbulence". In: *Phys. Rev. E* 79.046325 (2009).
- [126] L. Wang and N. Peters. "A new view of flow topology and conditional statistics in turbulence". In: *Phil. Trans. of Roy. Soc.* 371.20120169 (2013).
- [127] L. Wang and N. Peters. "The length scale distribution function of the distance between extremal points in passive scalar turbulence". In: *J. Fluid Mech.* 554 (2006), pp. 457–475.
- [128] L. Wang and N. Peters. "The Length scale distribution functions and conditional means for various fields in turbulence". In: J. Fluid Mech. 608 (2008), pp. 113–138.
- [129] World Energy Outlook 2019. IEA, Paris, 2019.
- [130] A. A. Wray and J. C. R. Hunt. "Algorithms for classification of turbulent structures". In: *Topological Fluid Mechanics*. Ed. by H. K. Moffat and A. Tsinober. Cambridge University Press, 1990, pp. 95–104.
- [131] Y. B. Zeldovich and F. Frank-Kamenetski. "Zhurnal Fis." In: *Khimii* 12 (1938), p. 100.